

# Bifurcation Analysis of Nonlinear Ground Handling of Aircraft

**James Rankin**

Department of Engineering Mathematics

University of Bristol



A dissertation submitted to the University of Bristol in  
accordance with the requirements of the degree of  
Doctor of Philosophy in the Faculty of Engineering.

March 2010



## Abstract

Nonlinearities inherent in the landing gear geometry, the complex interactions at the tyre-ground interface and the aerodynamics play an important role in the behaviour of aircraft on the ground. The use of computer models that incorporate nonlinear effects is becoming more widespread in industry. Numerical continuation and bifurcation analysis have successfully been applied in the study of road vehicle dynamics and flight dynamics. However, the study of aircraft ground handling has not yet been approached in this way. Here, we work with computer and mathematical models that capture the important nonlinear effects in the relevant components to show that bifurcation and continuation methods provide an efficient and effective way of investigating the highly nonlinear dynamics of an aircraft moving on the ground.

In order to investigate turning manoeuvres we utilise an established, industry-tested, multi-body systems model representing an Airbus A320 passenger aircraft. The model is linked directly to the numerical continuation package AUTO without the need to derive the equations of motion explicitly. Steady-state solutions of the system are fixed-radius turning circles. We present a bifurcation study showing how these solutions change with respect to variation of two control inputs: the steering angle and the thrust level. Identified are regions of stable turning and regions of laterally unstable behaviour; the transition between these types of behaviour is associated with a Hopf bifurcation. A detailed study of the undesirable behaviour associated with a loss of lateral stability focuses on the saturation of tyre forces at different wheel sets. The presented bifurcation diagrams identify parameter regions for which undesirable behaviour is avoidable and, thus, they form a foundation for defining the safe operating limits during turning manoeuvres.

Next we present the derivation and validation of a fully mathematical model that facilitates more elaborate bifurcation studies in terms of additional operational parameters. Two-parameter bifurcation diagrams are represented in compact form as surfaces of solutions that provide complete descriptions of the overall dynamics. Under the variation of additional parameters, qualitative changes to the solution structure are identified and the physical relevance of these changes is explained. Our results give a full description of the possible turning dynamics of the aircraft in dependence on four parameters of operational relevance. With a combination of numerical continuation and simulation we gain further insight into the mechanism by which lateral stability of the aircraft is lost. The system is shown to have a separation of time scales and to exhibit so-called canard-type oscillations; these phenomena are directly related to physical effects in the system.

To complement the bifurcation analysis of steady-state solutions, a transient analysis is presented that takes into account the taxiway geometry and fully captures the aircraft's behaviour during the initialisation and execution of a turn. We introduce a general approach to assess an aircraft's performance during taxiway manoeuvres across the range of its operation. The limits of operating regions are determined from published data on the usage of in-service aircraft. The maximal lateral loads experienced at individual landing gears are found, and this information allows us to assess the suitability of existing regulations for the certification of aircraft. A comparison between the steady-state and transient analysis shows that regions of safe operation as defined in the bifurcation analysis are physically relevant and of practical importance.



## **Acknowledgements**

The project was funded by an Engineering and Physical Sciences Research Council (EPSRC) Case award grant in collaboration with Airbus in the United Kingdom.

I would like to thank my supervisors Prof. Bernd Krauskopf, Dr. Mark Lowenberg and Sanjiv Sharma for their continued support and encouragement. Without their guidance and expertise this Ph.D. would not have been possible. I am truly grateful to Etienne Coetzee who led the way and acted as a patient and insightful adviser throughout.

Thanks also to Mathieu Desroches, Clare Lee and Dave Rodrigues who taught me how to do everything in the beginning, and Phani Thota has always found the time to offer his help. During my time with the Engineering Mathematics Department I have made too many friends to mention, safe to say, if we shared a few ales in the Hope and Anchor, I couldn't have done it without you.

I am indebted to Paul Street and everyone that made my time in Bristol so unique. The last few summers will never escape my fondest memories. A special thank you to 'Team Buzz' who kept me on the straight and narrow in that all-important final summer and taught me humility, patience, tolerance, commitment and poypes as we wended our way through Italy.

My family have been right behind me every step of the way: a massive thank you.



*“No good fish goes anywhere without a porpoise.”*

**Lewis Carroll**



### **Author's Declaration**

I declare that the work in this dissertation was carried out in accordance with the regulations of the University of Bristol. The work is original except where indicated by special reference in the text and no part of the dissertation has been submitted for any other degree.

Any views expressed in the dissertation are those of the author and in no way represent those of the University of Bristol.

The dissertation has not been presented to any other University for examination either in the United Kingdom or overseas.

Signed:

Dated:



# Contents

<b>1</b>	<b>Introduction</b>	<b>1</b>
1.1	Research motivation and objectives . . . . .	1
1.2	Review of existing work . . . . .	2
1.3	Thesis overview . . . . .	3
<b>2</b>	<b>Bifurcation analysis of turning solutions</b>	<b>5</b>
2.1	Introduction . . . . .	5
2.2	SIMMECHANICS model . . . . .	7
2.2.1	Tyre modelling . . . . .	8
2.2.2	Modelling the oleos . . . . .	11
2.2.3	Modelling the aerodynamics . . . . .	12
2.3	Bifurcation analysis of aircraft turning . . . . .	13
2.3.1	Low-thrust case . . . . .	14
2.3.2	High-thrust case . . . . .	16
2.3.3	Two-parameter bifurcation diagrams . . . . .	18
2.4	Different types of periodic solution . . . . .	19
2.4.1	Diagrammatic representation . . . . .	23
2.4.2	Detailed discussion of cases A–D . . . . .	23
2.5	Discussion . . . . .	30
<b>3</b>	<b>Operational parameter study</b>	<b>33</b>
3.1	Introduction . . . . .	33
3.2	Mathematical model . . . . .	34
3.2.1	Tyre modelling . . . . .	38
3.2.2	Modelling the aerodynamics . . . . .	41
3.3	Validation of mathematical model . . . . .	42
3.4	Two-parameter bifurcation study and sensitivity analysis . . . . .	44
3.4.1	Heavy aircraft case . . . . .	45
3.4.2	Light aircraft case . . . . .	48
3.4.3	Qualitative changes of the surfaces of solutions with thrust . . . . .	50
3.5	The effect of reducing tyre friction coefficient . . . . .	52
3.6	Periodic orbits as canard cycles . . . . .	53
3.7	Discussion . . . . .	56
<b>4</b>	<b>Lateral loads during typical taxiway turns</b>	<b>59</b>
4.1	Introduction . . . . .	59
4.1.1	Specific loading cases . . . . .	62

---

4.2	Generic parameterized turn . . . . .	63
4.2.1	Trajectory geometry . . . . .	64
4.3	Operating region for typical taxiway turns . . . . .	65
4.3.1	Relating parameterized turn trajectories to specific manoeuvres . . . . .	66
4.3.2	Maximal lateral loading conditions and operating regions . . . . .	68
4.4	Maximal lateral gear loads in operating regions . . . . .	70
4.5	Operating region for efficient turns . . . . .	72
4.6	Comparison of transient analysis and continuation analysis . . . . .	74
4.7	Discussion . . . . .	76
<b>5</b>	<b>Conclusion and outlook</b>	<b>79</b>
5.1	Summary . . . . .	79
5.2	Future work . . . . .	80

# Chapter 1

## Introduction

### 1.1 Research motivation and objectives

The dynamics of an aircraft manoeuvring on the ground are governed by many different aspects of its design, loading and operational practice. The handling qualities, which play a crucial part in safety and ride comfort, are also determined by factors such as the runway surface, weather conditions and tyre wear. From a commercial point of view, the speed at which taxiing manoeuvres are performed is important: a reduction of time spent taxiing improves efficiency of operations at airports. Computer modelling has been an invaluable tool in studying the ground dynamics of aircraft due to the high cost of real ground tests. Modelling and simulation have been used extensively in the design phases of new aircraft and for the analysis of existing aircraft, for example, to perform taxiway clearance tests. Control of aircraft on the ground is one of the few areas in which automation has not been employed. The design of controllers to automate ground operations is heavily reliant on computer modelling and a greater understanding of ground manoeuvres in general. The overall motivation for this work is to gain a deeper understanding of the dynamics of aircraft moving on the ground in order to inform operational practice, the design of future aircraft and the design of ground automation systems.

Nonlinear effects are known to play a significant role in the dynamics of aircraft on the ground [5, 21]; numerical continuation [12, 28] and bifurcation analysis [19, 50] are powerful tools in the study of nonlinear systems and have been successfully applied in many fields of science. The use of these methods in the fields of aeronautical engineering and vehicle dynamics is slowly becoming more widespread. The first goal of the thesis is to demonstrate the benefits of applying continuation and bifurcation techniques in the study of aircraft ground dynamics. In particular, by investigating the steady-state dynamics of the system under variation of parameters, we aim to find the limits of safe operation for the aircraft; we anticipate that the limit of safe operation will be related to a bifurcation. The effectiveness of these methods is dependent on a modelling approach that captures the dominant physics of the system at a manageable level of complexity. An appropriate model will allow findings from the bifurcation analysis to be related back to the physical behaviour. In order to relate manoeuvres to taxiway geometry and operational practice it will be necessary to include a transient analysis. The results should take into account, and be compared with, available usage data. Overall, we aim to better understand what it means to operate the aircraft close to and outside the limits of stable turning, and develop new methods for the prediction of safe operating regions.

## 1.2 Review of existing work

Firstly, we discuss the available usage data recorded from in-service aircraft. As part of an extensive testing campaign the Federal Aviation Administration (FAA) recorded data from in-service aircraft to be used in order to identify factors that affect the service life of commercial aircraft and to assess existing certification criteria [45, 46, 47]. Such statistical studies are important in identifying any disparity between expected usage during the design phase and the actual day-to-day operation of commercial aircraft. A further study by the FAA [55] compares the usage data from a range of different sized aircraft. Another study [22] employs this information to investigate specific criteria for the lateral loads experienced during ground manoeuvres. To address explicit concerns, the statistical studies are complemented by specific ground tests; Finn et al. [16] perform ground tests to find the actual maximal lateral loads experienced at individual landing gears. In a series of studies by Klyde et al. specific ground tests are used to evaluate handling characteristics [25], the effect of tyre pressure on ground handling [26], and assess the effectiveness of an augmented steering system [27]. In another study [24] these ground tests are complemented by an investigation of understeer/oversteer characteristics with a low-order linear model.

Mathematical and computer modelling are used extensively in industry due to relatively low cost and risk compared with real-world tests. Alongside the traditional, theoretical approach [18, 57], the application of computer modelling — in particular, multibody systems methods — is well established in the analysis of road vehicles [6, 48]. Furthermore, multibody systems software packages are widely used during the design phases of new aircraft and to study existing aircraft. The advantage of working with multibody systems packages, such as ADAMS [6] and SIMMECHANICS [34], is that the software provides a complete framework within which models can be defined, validated and simulated. Reference [23] is an example from the literature in which a multibody system model is used to study an aircraft's ground dynamics, specifically, asymmetric gear loading during landing and landing roll. The motion of bicycles has been studied extensively using both mathematical modelling and multibody systems approaches; Reference [35] is a good entry point to the literature.

An important aspect of modelling any vehicle is nonlinearities introduced via geometry and specific properties of components, such as the tyres, steering systems and aerodynamic surfaces. In traditional road vehicles the most significant nonlinear effects are introduced at the tyre-ground interface [40]. To study the dynamics of aircraft in flight nonlinear models are used extensively; Reference [52] provides an overview. Since nonlinearities are known to play an important role in the dynamics of a given system, it is important to fully incorporate them as part of the model and the analysis. Bifurcation and continuation methods, effective tools for the study of nonlinear models, have been applied in the field of aircraft dynamics, for example, to flight dynamics [9, 33], to autogyro stability [32] and to a model of a rotorcraft with an underslung load [3]. Bicycle dynamics have been investigated with nonlinear models in which bifurcations occur [17]; in Reference [2] families of turning solutions are computed with numerical continuation. Numerical continuation has been coupled with a symbolically defined multibody system model of a motorcycle [36]. Bifurcation analysis has been used successfully to study low-order road vehicle models; steady-state behaviour, periodic motion and chaotic dynamics have been found in models of longitudinal motion with periodic forcing [58] and driver feedback control [31, 30]. In References [38, 39, 56] the lateral dynamics are investigated with the fixed longitudinal velocity treated as a parameter and it is shown that a loss

of stability, resulting in the car entering a spin, is associated with a bifurcation. Bifurcation and continuation techniques have been used to study wheel shimmy [49]. Nose landing gear shimmy during straight-line aircraft motion has been investigated using low-order mathematical models [53, 54]. Though continuation and bifurcation methods have been used extensively in related fields, their application to the study of an aircraft turning on the ground is new. The starting point of the research presented here is Etienne Coetzee's Master's thesis [10], which is the first demonstration of the usefulness of bifurcations methods for the study of aircraft ground manoeuvres.

### 1.3 Thesis overview

In Chapter 2 we introduce a tricycle model of a commercial aircraft in the multibody systems package SIMMECHANICS. The individual component models include important nonlinear effects: the lateral tyre forces depend nonlinearly on vertical load and tyre slip angle, and the aerodynamic forces depend nonlinearly on the aircraft velocity and its angle with respect to the oncoming airflow. The fully validated model is coupled to the continuation package AUTO [12] in MATLAB which allows turning circle solutions (steady-state solutions in the aircraft's body axis) to be tracked under the variation of parameters. The continuation output is presented in bifurcation diagrams where system states are plotted against varying parameters. Specifically, we present a bifurcation analysis of the underlying solution structure that governs the dynamics of turning manoeuvres in dependence on the steering angle and thrust level. Furthermore, a detailed study of the behaviour when lateral stability is lost focuses on how the tyre saturation at different wheel sets leads to qualitatively different types of overall behaviour. The presented bifurcation diagrams identify parameter regions for which undesirable behaviour is avoidable and, thus, they form a foundation for defining the safe operating limits during turning manoeuvres.

In Chapter 3 we give the full equations of motion for an aircraft turning on the ground. The equations of motion are derived from first principles in terms of forces and moments acting on a rigid airframe; details are given of the necessary steps to incorporate component models described in Chapter 2. The resulting fully parameterized mathematical model is used to produce the results in the remainder of the thesis. The key advantage of the mathematical model is that it removes the black-box nature of working with a multibody systems package and allows full access to all component states. In general, it allows for extended integration with AUTO and is computationally much more efficient than the SIMMECHANICS model. We present a validation of the mathematical model in terms of both steady-state solutions and laterally unstable periodic motion. The results from an extended bifurcation analysis, computed in terms of the steering angle and the aircraft's centre of gravity position, are represented in a compact form as surfaces of solutions; we identify regions of stable turning and regions of laterally unstable motion. The boundaries between these regions are computed directly and they allow us to determine ranges of parameter values for safe operation. The robustness of the results under the variation of additional parameters, specifically, the engine thrust and aircraft mass, are investigated. Qualitative changes in the structure of the solutions are identified and explained in detail. Overall, our results give a complete description of the possible turning dynamics of the aircraft in dependence on four parameters of operational relevance. Also presented is an investigation into the effect of reducing the tyre friction coefficient; we find that there is a

direct equivalence between reducing the friction coefficient and increasing engine thrust. Finally, we provide a theoretical explanation for apparently discontinuous jumps in the amplitude of periodic motions studied in Chapter 2.

In Chapter 4 we study the lateral loads experienced during typical taxiway turns. The main motivation for this work is to evaluate the suitability of the existing Federal Aviation Regulation for lateral loads experienced during turning manoeuvres. The analysis differs from previous chapters in that we take into account the transient behaviour whilst the aircraft converges to a stable turning circle; initial investigations showed that the maximal lateral loads occur in the transients. We present a general approach to assess an aircraft's performance during taxiway manoeuvres across the range of its operation. Operating regions are defined in terms of parameters specifying the approach velocity and the steering input for a generic turn that is representative of pilot practice. The limits of the operating regions represent the extremes of the aircraft's operation during turning as determined by the maximal lateral loading conditions identified in a published FAA study [22]. The performance of the turn can be assessed over the entire operational range in terms of the actual loads experienced at individual landing gears. Recent studies by the FAA of instrumented aircraft have been limited to investigating the lateral loads experienced at the aircraft's CG position [22, 47, 55]. Our results show that this information is insufficient to predict the actual loads experienced by individual landing gears, especially for the nose gear which is found to experience considerably higher lateral loads than predicted by the corresponding loads at CG. The results are shown to be consistent for different aircraft mass cases and a different criterion for the limits of the operating regions. Finally, we relate the results from the transient analysis to the continuation analysis in order to determine the suitability of the defined regions of safe operation.

In Chapter 5 we present a summary of our findings, how the project objectives have been addressed and outline directions for future work.

# Chapter 2

## Bifurcation analysis of turning solutions

The model and results presented in this chapter have been published in [42].

### 2.1 Introduction

When creating a dynamical systems model it is important to identify, in as simple a manner as possible, the significant components and appropriate levels of complexity in order to capture all relevant behaviour. The model used here, designed with these considerations in mind, is a SIM-MECHANICS [34] model that was developed in parallel with a well-established ADAMS [6] model of an Airbus A320 (a typical mid-sized, single-aisle, passenger aircraft). The model was used for a previous study of nonlinear ground dynamics [10]. The software packages ADAMS and SIMMECHANICS utilise a multibody systems approach to study the dynamical behaviour of connected rigid bodies that undergo translational and rotational displacements [6, 48]. We consider a tricycle model where the landing gears are connected to the airframe by translational joints (allowing displacement in vertical axis only) for the main gears and a cylindrical joint (allowing displacement in, and rotation around, the vertical axis only) for the nose gear that steers the aircraft. The models for individual components, the forces acting on them and generated by them are constructed from test data, including nonlinear effects where appropriate. The main contributors to nonlinearity are forces on the tyres, the oleo (shock absorber) characteristics and the aerodynamic forces generated by the airframe. The model was developed using data in normal operating regions of the aircraft with the aim that simulations be carried out within these regions. In order to study behaviour outside of the normal operating regions, in particular when lateral stability is lost, it was necessary to extend the range of definition for some of the component models.

We consider turning manoeuvres that an aircraft may make when exiting the runway at high speed or taxiing to and from the airport terminal. Turns are made by adjusting the steering angle of the nose gear whilst the aircraft is in motion. During ground operations the thrust may be changed occasionally to adjust speed, however the thrust is kept constant during individual turns. We assume that no drive or braking forces are applied through the tyres. In particular, we are concerned with turning manoeuvres in which a fixed steering angle is applied for the duration of a turn; as an aircraft turns it follows a partial turning circle, and when the turn is complete the steering is straightened up. The performance of turning circle manoeuvres

is a traditional test case for aircraft. Following a turning circle corresponds in the model to a steady-state solution for the aircraft because it does not undergo any accelerations in the body frame. In our analysis we focus on fixed steering angle turning circle solutions and their stability, because they dictate whether a particular turning manoeuvre is possible without a loss of lateral stability of the aircraft. We do not consider here any direct pilot or controller input, as are required for transient cases such as a lane change manoeuvre. However, in the bifurcation analysis approach it would be possible to include pilot and/or controller action by considering an extended model.

Continuation is a numerical method used to compute and track or follow steady-state solutions of a dynamical system under the variation of parameters [1]. In our case, we treat the steering angle of the aircraft as a continuation parameter and, hence, compute how the turning circle solutions change as the steering angle is varied. Although the thrust of the aircraft is kept constant for individual continuation runs, it is used as a second parameter, with continuation runs performed across a range of discrete thrust levels. Stability is monitored whilst solutions are being followed; changes in stability correspond to bifurcations, which are qualitative changes in the behaviour of the system. Physically, changing the steering angle beyond a bifurcation point to a value where the turning circle solution is unstable can lead to a loss of lateral stability of the aircraft and, therefore, it can enter a skid or even a spin. One of the main strengths of the continuation methods used to produce this bifurcation analysis is the ability to identify safe parameter regions where it is known that the aircraft will follow a stable turning circle. Additionally, it is possible to follow solutions when they are unstable, leading to the identification of physical phenomena which otherwise might not be detected with time history simulations alone. The data produced from continuation can be represented in bifurcation diagrams of a state variable plotted against parameters, which show how the solutions change by indicating stability and identifying bifurcation points. The bifurcation diagrams describe the underlying dynamical structure of a system from which we can explain the reasons for specific behaviour (instead of just describing or observing it). This provides a more global picture of the dynamics of the nonlinear system, the aircraft during turning in our case.

We present a bifurcation analysis of a particular aircraft configuration during turning manoeuvres. Results were obtained by coupling the SIMMECHANICS [34] model with the continuation software AUTO [12] in MATLAB. The use of continuation software facilitates the determination of the stability of turning operations as described below. We identify regions in the steering angle versus thrust parameter plane for which the aircraft follows a stable turning circle or, if the turning circle solution is unstable, a periodic motion. Note that, although turning circle solutions are spatially periodic, we do not consider them as periodic solutions here because the aircraft states remain constant in the body axis. The bifurcation diagrams at two fixed thrust levels for which the steering angle is varied are explained in detail, identifying the different kinds of solution and what it means to switch between these solutions. In the bifurcation diagrams, the solutions are shown in terms of the modulus of the velocity of the aircraft. In order to explain the dynamics represented by the diagrams, aircraft trajectory and time histories are used. The results for two parameters, the steering angle and the thrust level, are obtained by combining bifurcation diagrams over a range of discrete thrust levels. To summarise the behaviour over the complete range of relevant values, a surface plot is rendered. The surface plot reveals robustness of the solution structure over the range of thrust levels. Therefore, by identifying regions of uniformly stable turning solutions in combination with information from the two fixed thrust cases, the surface plot explains all relevant dynamics in a very compact

way.

When lateral stability is lost, the aircraft performs a periodic motion relative to the now unstable turning circle. During the periodic motion lateral stability of the aircraft is lost and it enters a skid or, in some cases, a spin before coming to a near or full stop. Due to the fixed thrust, the aircraft speeds up again before losing lateral stability once more and, therefore, the motion is repeated periodically. Due to the the way the model is implemented in SIMMECHANICS it is not possible to use continuation to study these periodic solutions. Therefore, in this chapter we use time history simulations to compute periodic solutions instead. Regions of qualitatively different behaviour are identified along a branch of solutions. In order to explain the different types of periodic behaviour a new diagrammatic representation is introduced. For four qualitatively different cases an ordered series of diagrams show how the state of the aircraft changes over one period of motion. Each series of diagrams describes the changes in the dynamical state of the aircraft in terms of its translational and rotational motion whilst identifying the saturation of individual tyres. Together with the bifurcation analysis our results give a full and detailed explanation of the stable dynamics of the aircraft over the entire range of relevant steering angle and thrust values.

This chapter is organised as follows. In Section 2.2 full details of the model are given. The results of the continuation analysis in the form of bifurcation diagrams and a global picture of the dynamics are given in Section 2.3. In Section 2.4 periodic solutions are studied in detail. Finally, a discussion of the results in this chapter is presented in Section 2.5.

## 2.2 SIMMECHANICS model

The model of an Airbus A320 passenger aircraft that we study here is based on an ADAMS [6] model. This model has been implemented in SIMMECHANICS [34] so that it can be coupled with the continuation software AUTO [12] in MATLAB. Importantly, the package AUTO has direct control of the dynamical states in the SIMMECHANICS model and therefore is using the system definition in an implicit way. Hence, we are able to study an industrially tested high-order model without the need for explicit equations.

We study a tricycle model in which the nose gear is used for steering. The model has nine degrees of freedom (DOF); six DOF for the fuselage and one DOF for each of the oleos. Table 2.1 lists the dimensions of the aircraft. The lightweight case is considered here in which there are no passengers or cargo and the minimal amount of fuel is on board. The mass is 45420kg and we consider a forward position for the centre of gravity (CG) (14% of the Mean Aerodynamic Chord).

SIMMECHANICS can analyse kinematic, quasi-static and dynamic mechanical systems. The first step of the modelling is to describe the rigid parts and the joints connecting them [6], where a part is described by its mass, inertia and orientation. The airframe is modelled as a rigid body to which the individual landing gears are connected. In the tricycle model considered here the nose gear is constrained by a cylindrical joint and the main gears are constrained by translational joints. The next step is the addition of internal force elements, known as line-of-sight forces, to represent the shock absorbers and tyre forces. External forces such as thrust and aerodynamic forces are then added, they are known as action-only forces. All geometric

**Table 2.1.** Aircraft dimensions.

Length	37.6m
Wingspan	34.1m
Height	11.8m
Fuselage width	4.0m
Wheelbase	12.8m
Track width	7.6m

aspects were parameterized, from the axle widths, wheel dimensions, gear positions, to the rake angles on the gears. This means that all joint definitions and forces are automatically updated when the design variables are changed. A schematic of the SIMMECHANICS model is shown in Figure 2.1.

Direct control of the steering angle is assumed, in that it is varied as a continuation parameter during the continuation runs. In all of the computations discussed below the thrust is kept constant, where a PI (proportional-integral) controller is used to find the desired thrust levels. Further details of the continuation process are explained in the Section 2.3.

Several nonlinear components are included in the model. The modelling of the tyres, the oleos and the aerodynamics is based on real test data. In each case there are nonlinear relations depending on dynamic states of the system. The data on which the models are based comes from tests performed within the normal operating regions for the aircraft. Previously the model has been used by the Landing Gear Group at Airbus to generate results within these regions. In order to model the dynamics when the lateral stability of the aircraft is lost, it is necessary to study the behaviour outside the normal operating regions. Therefore, it is required that the range of definition is extended in the models of certain components. The details of how this was done in the case of the tyre model and aerodynamic forces is discussed now.

### 2.2.1 Tyre modelling

Apart from the aerodynamic, propulsive and gravitational forces, all other loads on the aircraft are applied at the tyre-ground interface. Tubeless radial tyres are generally used for aircraft due to better failure characteristics when compared with bias-ply tyres [57]. The force elements acting on the tyres are calculated with a tyre model developed by a GARTEUR action group investigating ground dynamics [20]. The fundamental work behind this model can be found in [40]. In our model there are two tyres per gear, although due to the small separation distance they can be assumed to act in unison. At lower velocities the forces generated by the tyres have a dominant effect over aerodynamic forces on the motion of the aircraft.

The vertical force component on the tyre can be approximated by a linear spring and damper system [6]. The total force is:

$$\begin{aligned}
 F_z &= -k_z \delta_z - c_z V_z \\
 &= -k_z \delta_z - 2\zeta \sqrt{m_t k_z} V_z,
 \end{aligned}
 \tag{2.1}$$

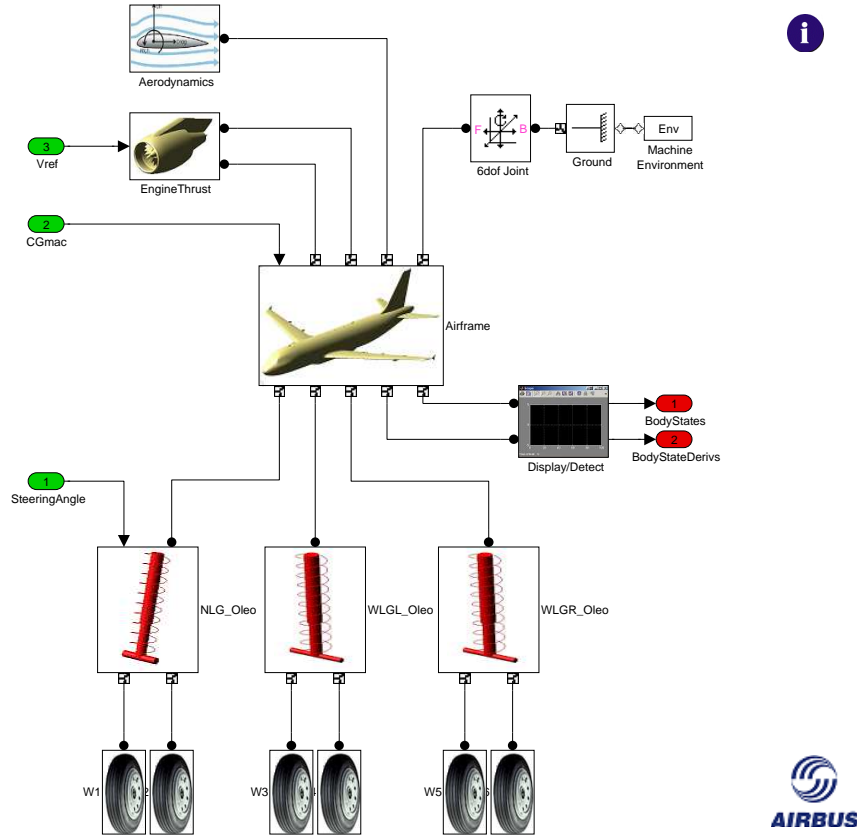


**Figure 2.1.** SIMMECHANICS representation of A320.

**Table 2.2.** Parameters values used to calculate the vertical tyre force in Equation (2.1).

Parameter	Description	Units	Nose	Main
$m_t$	mass of tyre	kg	21	75.5
$k_z$	stiffness coeff.	kN/m	1190	2777
$\zeta$	damping ratio		0.1	0.1
$c_z$	damping coeff.	Ns/m	1000	2886

where  $V_z$  is the vertical velocity of the tyre, and  $\delta_z$  is the tyre deflection representing the change in tyre diameter between the loaded and unloaded condition. The coefficients are specified in Table 2.2.

Rolling resistance on hard surfaces is caused by hysteresis in the rubber of the tyre. The pressure in the leading half of the contact patch is higher than in the trailing half, and consequently the resultant vertical force does not act through the middle of the wheel. A horizontal force in the opposite direction to the wheel movement is needed to maintain an equilibrium. This horizontal force is known as the rolling resistance [57]. The ratio of the rolling resistance  $F_x$ , to vertical load  $F_z$ , on the tyre is known as the coefficient of rolling resistance  $\mu_R$ , where a value of 0.02 is typically used for aircraft tyres [37]. We use an adapted Coulomb friction

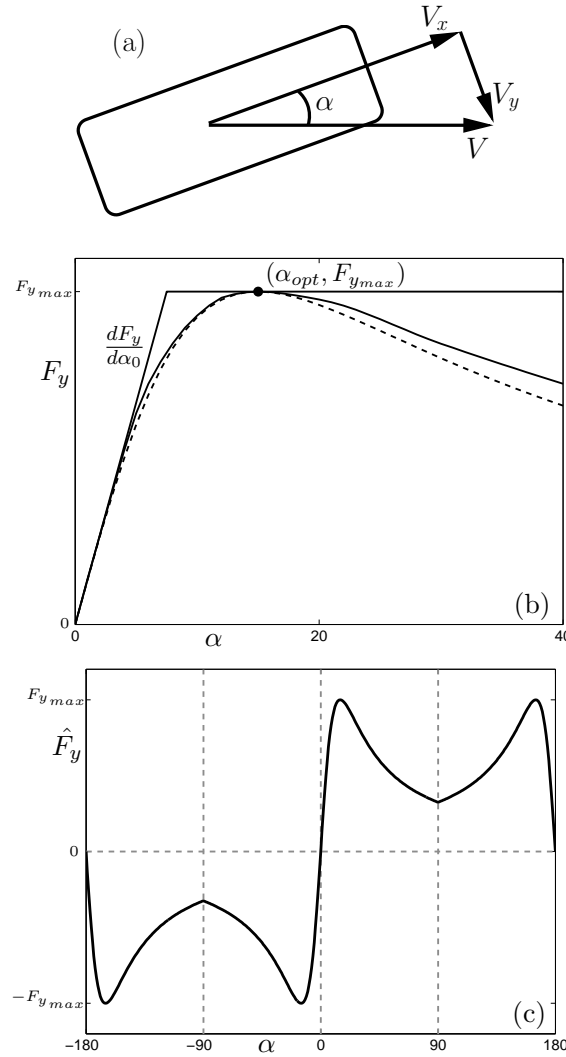


**Figure 2.2.** Panel (a) shows how the slip angle  $\alpha$  is calculated. Panel (b) shows how the normalised lateral tyre force function, Equation (2.3) (dashed curve), approximates test data for  $\alpha \in (0^\circ, 40^\circ)$  (solid curve) for a given  $F_z$ . The function depends on the parameters  $(\alpha_{opt}, F_{y_{max}})$  marked at the apex of the graph. The lateral tyre stiffness is the gradient  $\frac{dF_y}{d\alpha_0}$  of the curve at  $\alpha = 0$ . Panel (c) shows how the lateral force function is extended over the range  $\alpha \in (-180^\circ, 180^\circ)$ .

model:

$$F_x = -\mu_R F_z \tanh(V_x/\varepsilon), \quad (2.2)$$

which incorporates a hyperbolic tangent function to approximate the switch in sign of the force when the direction of motion of the tyre changes; the parameter  $\varepsilon$  governs the level of smoothing and is fixed to a value of  $\varepsilon = 0.01$ .

When no lateral force is applied to a tyre, the wheel moves in the same direction as the wheel plane. When a side force is applied to the wheel it makes an angle with its direction of motion. This angle is known as the slip angle  $\alpha$ , as depicted in Figure 2.2(a). For small slip angles, typically less than  $\alpha = 5^\circ$ , the tyre force increases linearly after which there is a

nonlinear relationship [57]. The lateral force on the tyre  $F_y$  is a function of  $\alpha$ . It depends on the maximum lateral force  $F_{y_{max}}$  attainable by the tyre at the optimal slip angle  $\alpha_{opt}$  as given by:

$$F_y(\alpha) = 2 \frac{F_{y_{max}} \alpha_{opt} \alpha}{\alpha_{opt}^2 + \alpha^2}. \quad (2.3)$$

The parameters  $F_{y_{max}}$  and  $\alpha_{opt}$  depend quadratically on the vertical tyre force  $F_z$  and, hence, change dynamically in the model; the expressions for  $F_{y_{max}}$  and  $\alpha_{opt}$  in terms of  $F_z$  are given in Section 3.2.1. A function fitted to test data over the interval  $\alpha \in (0^\circ, 40^\circ)$  is plotted in Figure 2.2(b) as a solid curve. The lateral tyre force  $F_y$  from Equation (2.3) for the same  $F_z$  is plotted against tyre slip angle  $\alpha$  as a dashed curve. The tyre stiffness  $\frac{dF_y}{d\alpha_0}$  is the gradient of the function at  $\alpha = 0$ . In the results section we refer to a tyre as saturated if  $|\alpha|$  exceeds  $\alpha_{opt}$ .

The lateral tyre force function  $F_y(\alpha)$  is fitted to test data for a nominal load  $F_z$  obtained in the normal region of operation of the aircraft;  $\alpha \in (0^\circ, 40^\circ)$ . In the original model impulses on the force function are observed (at discontinuities at  $\alpha = \pm 180^\circ$ ) when operating outside this region. In order to study behaviour outside of the normal operating region it is necessary to extend the definition of the force function. Firstly with a change in sign of  $\alpha$  there is a corresponding change in the sign of  $F_y$ . To extend the range outside of  $\alpha = \pm 40^\circ$  we assume here that, as the slip angle increases beyond  $|\alpha| = 40^\circ$ , the force will continue to drop off as the size of the contact patch of the tyre will continue to decrease when the slip angle increases. Furthermore, due to symmetry of the forces on the tyre when it is rolling backwards, it is possible to extend the definition of the function over the range  $\alpha \in (-180^\circ, 180^\circ)$  with continuity at the points  $\alpha = \pm 90^\circ$ . The extended function  $\hat{F}_y(\alpha)$  is plotted in Figure 2.2(c).

### 2.2.2 Modelling the oleos

Oleo-pneumatic shock absorbers, which use a combination of oil and gas, are used in aircraft because they have the highest energy dissipation capability for a specific mass [11]. Single stage oleos are used for the nose and main landing gears in the model.

We now discuss the design of the spring curve for the oleos. A level attitude is desired when the aircraft is stationary. The static load for the nose and main landing gears is calculated using the maximum aircraft weight at the fore and aft CG positions, respectively. The extended/compressed stroke lengths and the stroke required for static loading are set based on the aircraft geometry. The compression ratio between two states of the oleo is the ratio of the respective forces in that state. The following compression ratios are used in the model:

- static to extended ratio of 5:1
- compressed to static ratio of 2:1.

The spring curve is fitted to the three points, the static load  $F_s$ , the extended load  $F_e$  and the compressed load  $F_c$ . Figure 2.3(a) shows the spring curve, load  $F_o$  (kN) against stroke  $l_s$  (mm) for the main landing gears.

Figure 2.3(b) shows the profile of the damping coefficient  $C$  ( $\text{kg}^2/\text{s}^2$ ) against stroke  $l_s$  for the main landing gears. The dashed curve shows  $C$  under extension and the solid curve under

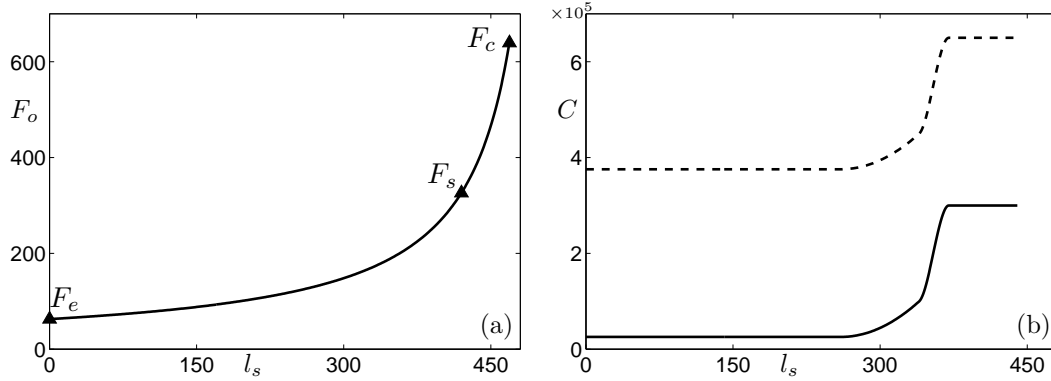


**Figure 2.3.** Oleo characteristics. Panel (a) shows the spring curve, load  $F_o$  (kN) against stroke  $l_s$  (mm), for the oleos, fitted to three points: the load  $F_s$  when the aircraft is statically loaded, the load  $F_e$  when the oleo is fully extended and the load  $F_c$  when the oleo is fully compressed. Panel (b) shows a plot of the damping coefficient  $C$  ( $\text{kg}^2/\text{s}^2$ ) against stroke  $l_s$  (mm) for compression of the oleo (solid curve) and extension of the oleo (dashed curve).

compression. The transition between the profile for extension ( $V_{oleo} > 0$ ) and compression ( $V_{oleo} < 0$ ) is continuous because the damping force is proportional to the vertical velocity of the oleo. In the results presented below the oleos operate with stroke approximately in the range  $l_s \in (300\text{mm}, 400\text{mm})$ . The force the oleo exerts on the airframe is given by:

$$F_{oleo}(l_s) = F_o(l_s) - C(l_s)V_{oleo}. \quad (2.4)$$

### 2.2.3 Modelling the aerodynamics

Aerodynamic effects are nonlinear because the forces are proportional to the square of the velocity of the aircraft. The forces also depend nonlinearly on the sideslip angle  $\beta$  and angle of attack  $\sigma$  due to the geometry of the aircraft. We consider ground manoeuvres with no incident wind. Hence, the sideslip angle  $\beta$  is equal to and interchangeable with the slip angle of the aircraft  $\alpha$ . Because we are studying ground manoeuvres the angle of attack  $\sigma$  remains relatively steady. There are six components to the aerodynamics forces; three translational forces and three moment forces. The forces and moments on the aircraft are defined in terms of its geometric properties and dimensionless coefficients based on wind-tunnel data and results from computational fluid dynamics. The coefficients used here were obtained from a (GARTEUR) action group [20] Simulink model in which they are defined using neural networks. Here, the calculation of the longitudinal drag force  $F_{xA}$  is explained in detail as an example; each of the other components is determined in a similar fashion. The force  $F_{xA}$  is described by the equation

$$F_{xA} = \frac{1}{2}\rho|V|^2S_wC_x, \quad (2.5)$$

where  $\rho$  is the density of air,  $S_w$  is the wing surface area,  $|V|$  is the modulus of the velocity of the aircraft and  $C_x$  is a dimensionless axial force coefficient that depends nonlinearly on the slip angle  $\alpha$  and angle of attack  $\sigma$ . The other force and moment equations are given in

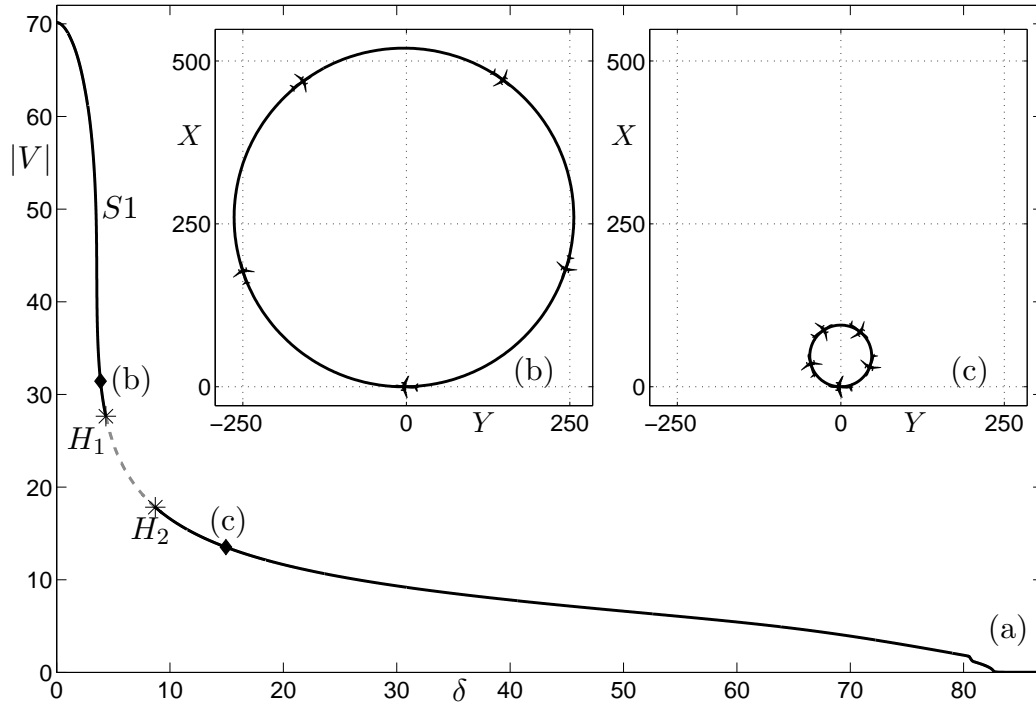


**Figure 2.4.** Panel (a) is a bifurcation diagram for 13% of maximum thrust with single branch  $S1$ . Stable parts are solid black lines and the unstable part a dashed grey line. Transitions from stable to unstable branches occur at the Hopf bifurcations  $H_1$  and  $H_2$ . Insets (b) and (c) show the aircraft CG curves in the  $(X, Y)$ -plane at the respective points on  $S1$  for  $\delta = 3.9^\circ$  and  $\delta = 14.9^\circ$ .

Section 3.2.2 and the values of the constant coefficients are given in Table 3.1. Here,  $C_x$  is defined over the range  $\alpha \in (-10^\circ, 10^\circ)$ ,  $\sigma \in (-2^\circ, 5^\circ)$ .

Whilst on the ground the angle of attack  $\sigma$  remains within the range of definition of the GARTEUR data. However, as we wish to consider behaviour of the aircraft for slip angles  $\alpha$  outside the range of the data it is necessary to define the functions for all values of  $\alpha \in (-180^\circ, 180^\circ)$ . When looking at behaviour for slip angles outside of the range  $\alpha \in (-10^\circ, 10^\circ)$ , the velocity of the aircraft is sufficiently small ( $|V| < 30\text{m/s}$ ) such that aerodynamic forces are small relative to those generated by the tyres. It is sufficient to ensure the forces are continuous over the full range of  $\alpha$  values. The extension of the definition of the axial force coefficients is done in a similar fashion to that of the lateral force functions in Section 2.2.1, where we use symmetries of the aircraft geometry and force saturation values outside of the specified ranges for  $\alpha$  and  $\sigma$ .

## 2.3 Bifurcation analysis of aircraft turning

In this section we use continuation software to perform a bifurcation analysis of the aircraft model introduced above. We focus on the stability of turning circle solutions over a range of

discrete fixed thrust levels where, for each thrust case, the steering angle is varied as a parameter. Each continuation run is executed at a fixed thrust level that corresponds to a constant straight-line velocity. The aircraft travelling at a constant velocity is a steady-state solution of the system and these solutions are used as initial points to start individual continuation runs. A PI (proportional-integral) thrust controller is used with the steering angle set to  $0^\circ$  to obtain the required fixed straight-line velocity. Starting from such an initial solution the steering angle is varied as a parameter whilst the stability is monitored. The results from the continuation runs are represented as bifurcation diagrams where the modulus  $|V|$  of the velocity of the aircraft is shown. Aircraft trajectory plots are shown with corresponding time histories where appropriate. In the trajectory plots a trace of the path of the aircraft's CG (centre of gravity) is drawn over the  $(X, Y)$ -plane (orthogonal ground position coordinates). Along the CG curve aircraft markers are drawn at regular time intervals to indicate the attitude of the aircraft relative to the CG curve. Note that the attitude of the aircraft on the CG curves is equivalent to its slip angle  $\alpha$  at that point in the simulation. The markers are not drawn to scale except when explicitly stated.

### 2.3.1 Low-thrust case

Figure 2.4(a) shows the continuation curve initiated from an equilibrium state for which the aircraft maintains a constant forward velocity of 70m/s at 13% of maximum thrust. The resulting solution branch  $S1$  of stable (solid) and unstable (dashed) solutions is plotted in the plane of the steering angle  $\delta$  and the modulus  $|V|$  of the aircraft velocity. The stability changes at the points  $H_1$  and  $H_2$ , which are indicated by stars. On the stable parts of  $S1$  the aircraft follows a turning circle and on the unstable part more complex stable solutions exist which are discussed below. Once a steering angle is applied ( $\delta > 0$ ), the tyres generate a side force that holds the aircraft in a turning circle. As  $\delta$  is increased the velocity of the aircraft rapidly decreases along with a decrease of the radius of the stable turning circle. The branch becomes unstable at the point  $H_1$ , where a Hopf bifurcation takes place [50]. Here a stable periodic solution is born, as is typical with a Hopf bifurcation. As the steering angle is increased further the velocity drops less rapidly along the unstable part of the branch, which regains stability at a second Hopf bifurcation  $H_2$ . As the steering angle is increased beyond  $H_2$  the aircraft velocity gradually decreases. Along the section of  $S1$  between the initial point and  $H_1$  the aircraft follows a large turning circle and all tyres forces remain safely below their saturation levels. Along the section between  $H_2$  and the final point the aircraft follows a small radius turning circle. As  $\delta$  increases beyond  $H_2$  the turning circles become tighter and at  $\delta \approx 40^\circ$  the outer main gear saturates; for large  $\delta$  the main gear tyres are effectively dragged around the turn. At  $\delta \approx 83^\circ$  the force generated by the nose gear tyre is almost perpendicular to the thrust force and is sufficiently large to hold the aircraft stationary. The aircraft CG curve plots in Figures 2.4(b) and (c) correspond to the respective points on  $S1$  for  $\delta = 3.9^\circ$  and  $\delta = 14.9^\circ$ , where the aircraft follows a turning circles of radius  $r \approx 260\text{m}$  and  $r \approx 50\text{m}$ , respectively. Both insets are shown on the same scale and the aircraft markers also drawn to scale.

We now discuss the behaviour of the aircraft for steering angles where the turning circle solution is unstable. Figure 2.5(a) shows an enlargement of the unstable part of the branch  $S1$  from Figure 2.4(a). To find the stable behaviour in this region, model simulations are run at discrete values of the steering angle for  $\delta \in (4.37^\circ, 8.65^\circ)$ . After transients have decayed, stable

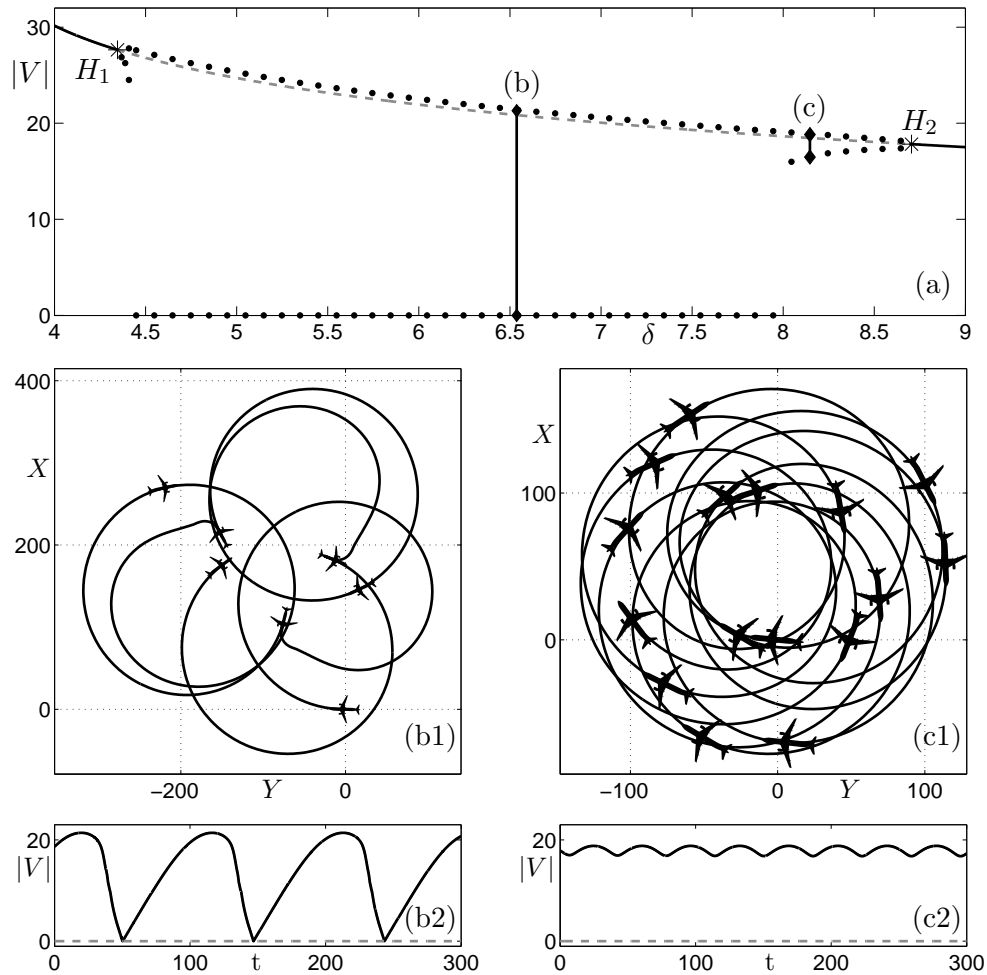


**Figure 2.5.** Panel (a) shows detail from Figure 2.4(a) with the maximum and minimum aircraft velocity  $|V|$  of periodic solutions, shown as black dots, determined by simulations at regularly spaced points between  $H_1$  and  $H_2$ . Note the sharp change in the minimum velocity curves at  $\delta \approx 4.4^\circ$  and  $\delta \approx 8.0^\circ$ . Panels (b1) and (c1) show aircraft CG curves in the  $(X, Y)$ -plane and panels (b2) and (c2) show time plots of aircraft velocity  $|V|$  at points  $\delta = 6.54^\circ$  (b) and  $\delta = 8.14^\circ$  (c), respectively.

behaviour is identified as a branch of periodic solutions. They are represented in Figure 2.5(a) by lines of black dots indicating the minimum and maximum velocities. For a steering angle just below  $H_2$  small oscillations are observed as is expected just after a Hopf Bifurcation. An aircraft CG curve and a time plot of aircraft velocity at point (c) are shown in the panels (c1) and (c2). The trajectory oscillates between turning circles of radius  $r_{max} \approx 90\text{m}$  and  $r_{min} \approx 75\text{m}$ . Physically, the aircraft approaches its maximum velocity and starts to oversteer. The oversteer increases and the velocity drops whilst the main inner tyres saturate and start to skid (the slip angle changes rapidly). The force on the main outer tyres increases to compensate and after a short amount of time the skid is recovered and the aircraft accelerates again towards its maximum velocity. In Figure 2.5(a) at  $\delta \approx 8^\circ$  there is a sharp increase in the amplitude of these oscillations that coincides with the outer main gear tyres also saturating and starting to skid; the result is that the aircraft enters a spin. In the region of larger oscillations the aircraft oscillates between following an approximate turning circle of  $r \approx 130\text{m}$  and making a  $180^\circ$  skid that brings the aircraft to a complete halt. An example CG curve and a time plot of aircraft velocity at point (b) are shown in the Figures 2.5(b1) and (b2). The sharp increase in the size of the oscillations for steering angles just beyond  $H_1$  happens in a similar fashion. Further details of the periodic oscillations are discussed below; their analysis in terms of tyre saturation is the focus of Section 2.4. The sharp transition between small amplitude oscillations and large amplitude oscillations is discussed further in Section 3.6.

### 2.3.2 High-thrust case

The bifurcation diagram is more complex for a higher thrust case. Figure 2.6(a) shows the curve of steady-state solutions initiated from an equilibrium position at which the aircraft maintains a constant forward velocity of  $90\text{m/s}$  at  $19\%$  of max thrust. Although the initial velocity is outside the normal operational range for ground manoeuvres, the solutions that exist at lower velocities are well within the aircraft's operational range. Studying solutions outside the normal operational range ensures that all the possible dynamics of the system are identified. In Figure 2.6(a) the equilibrium branch  $S1$  corresponds to that of the lower thrust case shown in Figure 2.4(a). The Hopf bifurcation  $H_2$  on the branch  $S1$  persists. There are two limit point (or saddle-node) bifurcations  $L_1$  and  $L_2$  that are characterised by a fold in the equilibrium curve and the coexistence of another solution at parameter values before the bifurcation [50]. Locally, in the case of  $L_1$ , a stable and an unstable solution coexist, and in the case of  $L_2$ , two unstable solutions coexist. Due to the changes in direction at  $L_1$  and  $L_2$ , a hysteresis loop exists for values of  $\delta$  around these bifurcations. The branch  $S1$  is unstable between  $L_1$  and  $L_2$  and between  $L_2$  and  $H_2$ . Along the unstable branch of  $S1$  between  $L_2$  and  $H_2$  there is a branch of periodic solutions that is discussed below. The maximum and minimum velocities of these solutions are shown as black dots. Furthermore, there is a new branch  $S2$  (disjoint from  $S1$ ) with stable and an unstable part separated by the limit point bifurcation  $L_3$ .

As is consistent with the lower thrust case, the aircraft follows a large radius turning circle solution on the part of  $S1$  between the initial point and  $L_1$ . Furthermore, on the stable part of  $S1$  beyond  $H_2$  the aircraft follows a tight turning circle solution with the outer main gear tyres saturated. Recall that, in this case for  $\delta > 85^\circ$ , there is a stable solution represented on  $S1$  for which the force generated by the nose gear is sufficient to hold the aircraft stationary. In this higher thrust case there is the coexisting solution branch  $S2$  because the thrust force is

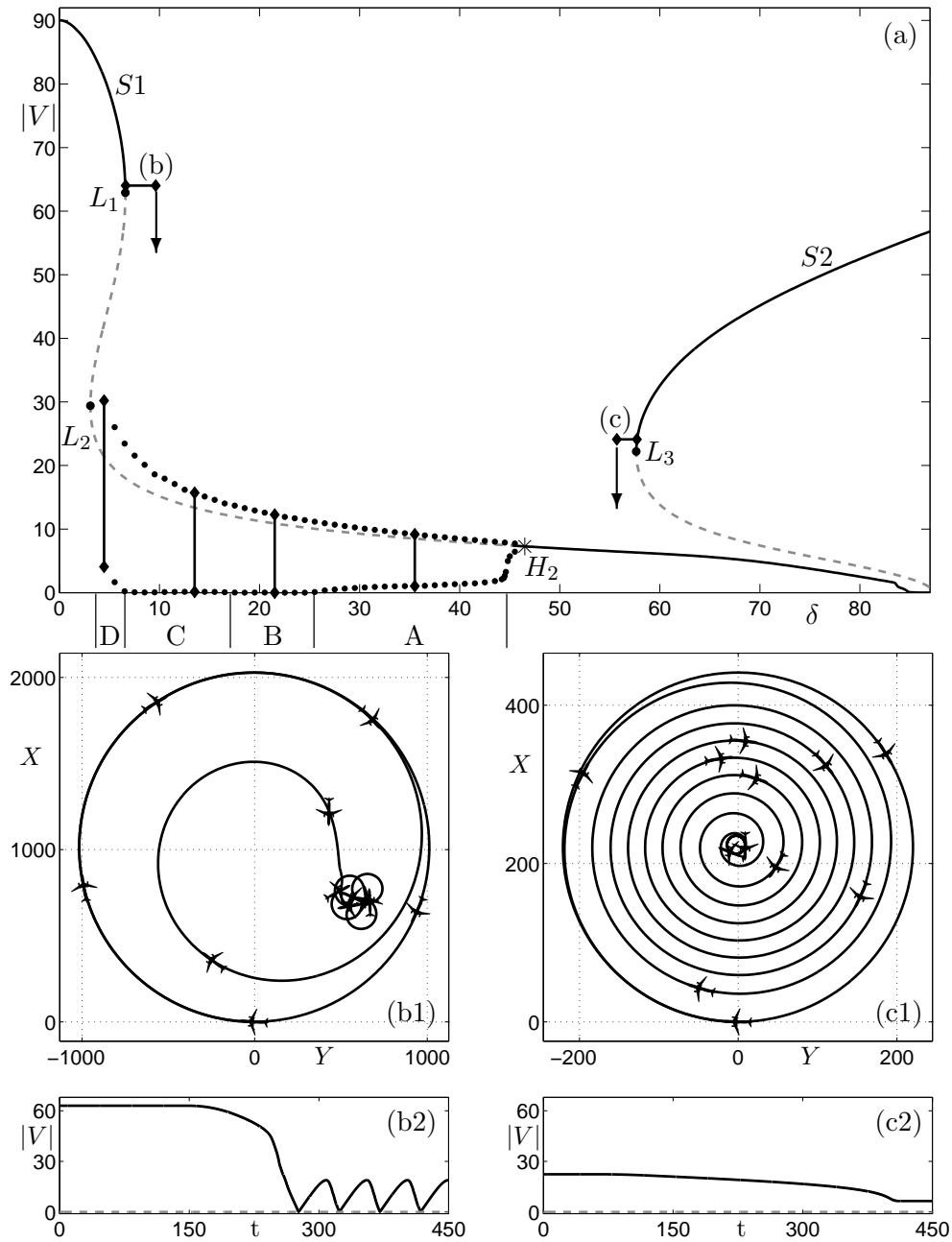


**Figure 2.6.** Panel (a) shows the bifurcation diagram for 19% of maximum thrust with two disjoint branches  $S1$  and  $S2$ . On  $S1$  there are two limit point bifurcations  $L1$  and  $L2$  and a Hopf bifurcation  $H2$ . On  $S2$  there is a limit point bifurcation  $L3$ . Periodic solutions exist along the unstable part of the branch  $S1$ , for which the maximum and minimum velocities are shown by black dots. Four regions A–D each with a different qualitative behaviour are indicated along the branch. Panels (b1) and (b2) show an aircraft CG curve and velocity plot at point (b) on  $S1$  followed by an increase in steering angle beyond  $L1$  ( $\delta = 6.6^\circ$  to  $\delta = 9.6^\circ$ ). Similarly (c1) and (c2) show the transition from the point (c) branch  $S2$  to branch  $S1$  where the steering angle is decreased past  $L3$  ( $\delta = 57.6^\circ$  to  $\delta = 55.6^\circ$ ).

sufficient to overcome the holding force generated by the nose gear if the aircraft is in motion. On the stable part of the new branch  $S2$  the aircraft follows a large turning circle solution with the nose gear tyres saturated.

We now consider the role of the limit point bifurcations  $L_1$  and  $L_3$ . Starting at a solution on the stable part of the branch  $S1$  and increasing the steering angle just beyond  $L_1$  causes the aircraft to move towards a different attractor. At point (b) with the steering angle  $\delta = 6.6^\circ$  the aircraft follows a turning circle with radius  $r \approx 1\text{km}$ . When the steering angle is ramped up to  $\delta = 9.6^\circ$  the aircraft moves towards to a different attractor. A CG curve plot and velocity  $|V|$  time plot are shown in Figures 2.6(b1) and (b2). In the simulation the aircraft follows a turning circle until the steering angle is ramped up after  $150\text{s}$  to a value beyond  $L_1$ , then the aircraft spirals inwards towards a periodic solution similar to that shown in Figures 2.5(b1) and (b2). There would be no immediate indication to a pilot that the limit point bifurcation is approached or passed; the aircraft tends to the periodic solution over a transient period. Decreasing the steering angle from  $\delta = 9.6^\circ$  (to a value below that at  $L_2$ ) causes the aircraft to deviate from this periodic solution and return to following a large turning circle on the stable part of branch  $S1$ . These two transitions between the stable part of  $S1$  and the periodic solution existing for values of  $\delta$  along the unstable part of  $S1$  form a hysteresis loop. In the example just described the aircraft jumps from a stable part of  $S1$  to a periodic solution about an unstable part of  $S1$ . A similar jump, this time between different branches, occurs when starting at a solution on the stable part of the branch  $S2$  and decreasing the steering angle below  $L_3$ . In this case the aircraft moves from a stable solution on branch  $S2$  to a stable solution on the branch  $S1$ . At point (c) the steering angle is initially  $\delta = 57.6^\circ$  and ramped down after  $70\text{s}$  to  $\delta = 55.7^\circ$ . Plots of the simulations are shown in Figures 2.6(c1) and (c2). The aircraft follows a turning circle of radius  $r \approx 220\text{m}$  and then spirals in towards a turning circle of radius  $r \approx 12\text{m}$ .

In Figure 2.6(a) the maximum and minimum velocities of the periodic solutions are shown by dotted black curves. The behaviour for a steering angle just below the bifurcation  $H_2$  was shown in Figure 2.5(c1). The same behaviour persists near  $H_2$  for the higher thrust case presented in Figure 2.6(a). As the steering angle is decreased below the bifurcation  $H_2$  the size of oscillations gradually increases. The increase in size of the oscillations corresponds to a greater loss of velocity when the aircraft deviates from the unstable turning circle solution. Figure 2.6(a) shows a steep but apparently smooth increase in the size of oscillations. The steepest part of this increase is at  $\delta \approx 45^\circ$ . For  $\delta < 45^\circ$  there are much larger oscillations. The transition between the small and large oscillations becomes sharper as lower thrust cases are considered as in Figure 2.5(a). This can be attributed to the fact that the transition from the existence of a stable turning circle for  $\delta > H_2$  to the unstable behaviour between  $H_1$  and  $H_2$  happens for smaller  $\delta$  and, therefore, at a higher velocity in the lower thrust case. The large oscillations are the subject of Section 2.4.

### 2.3.3 Two-parameter bifurcation diagrams

Having studied the steady-state solutions for two different thrust cases it is desirable to see whether the behaviour persists at different thrust levels. We consider the solutions for constant thrust levels that correspond to discrete initial forward velocities  $|V_{init}| \in (10\text{m/s}, 115\text{m/s})$ . Figure 2.7(a) shows a surface plot of steady-state solutions in  $(\delta, |V|, T)$ -space where  $T$  is the percentage of the maximum thrust of the engines. Figure 2.7(b) shows a corresponding contour

plot, effectively a top-down view of the surface in the  $(\delta, |V|)$ -plane. In both plots the loci of limit point bifurcations are labelled  $L$  and  $L^*$  and the locus of Hopf bifurcations is labelled  $H$ . The blue part of the surface that lies below the curves  $L$  and  $H$  represents stable turning solutions, and the red part above these curves represents unstable turning solutions. Individual solution branches used to create the surface are shown at regular intervals on the surface by thin black curves. For orientation, the solution branches shown in Figures 2.4(a) and 2.6(a) are highlighted by thick black lines on the surface and labelled  $C_{70}$  and  $C_{90}$ , respectively. In the contour plot the stability of the contours  $C_{70}$  and  $C_{90}$  is indicated as in Figures 2.4(a) and 2.6(a).

Bifurcations on the individual solution branches correspond to a crossing of a bifurcation locus curve. The example  $C_{70}$  consists of one piece, corresponding to the branch  $S1$ , which intersects the Hopf bifurcation locus curve  $H$  in two places corresponding to the bifurcations  $H_1$  and  $H_2$  in Figure 2.4(a). The transition between  $C_{70}$  and  $C_{90}$  is as follows. With increasing thrust levels two limit point bifurcations appear at a cusp point on  $L$ . The curve  $H$  terminates at an intersection with  $L$  (a Bogdanov-Takens bifurcation [29], not discussed here) and thus the Hopf bifurcation  $H_1$  no longer appears for thrust levels above this intersection. The second branch  $S2$  on  $C_{90}$  can be seen in the background of the surface plot; it is clearly seen in the contour plot in Figure 2.7(b).

The surface plot reveals that for thrust levels greater than at  $C_{90}$  the structure remains qualitatively the same except that branches  $S1$  and  $S2$  meet on  $L^*$ . For thrust levels below the minimal point on  $H$  the behaviour is trivial: for all values of  $\delta$  the solution branches represent stable turning circles. Furthermore, for thrust levels above the saddle point on  $L$ , at which point the bifurcations  $L_1$  and  $L_3$  meet and vanish, the behaviour is also uniformly stable. Due to the robustness of the structure, the surface in Figure 2.7(a) explains the equilibria dynamics fully. Therefore, by studying the two cases  $C_{70}$  and  $C_{90}$  in detail and using the surface and contour plots, we have described the underlying dynamics dictating the aircraft's behaviour across the entire range of relevant values in the  $(\delta, T)$ -plane comprehensively and in a compact manner.

## 2.4 Different types of periodic solution

We now study the branch of periodic solutions in Figure 2.6(a) for  $\delta \in (4.5^\circ, 46.5^\circ)$  in more detail. An attempt was made to follow the periodic solutions using AUTO, but it was only possible to find very short branches near the Hopf bifurcations. Due to the black-box nature of the SIMMECHANICS model it is difficult to assess the reason for this computational difficulty, but it may be related to the rapid growth of the solution profile. As an alternative we found the periodic solutions by simulation runs for discrete values of the steering angle. The stable periodic behaviour was found by running the model from an initial state of the system on the stable part of the branch  $S1$  near the bifurcation  $H_2$  and ramping down the steering angle. Once any transient behaviour has passed the persistent behaviour is studied. Here, we focus on the region the region of large amplitude oscillations (for  $\delta < 44.5^\circ$ ) which can be divided into four subintervals that correspond to qualitatively different types of periodic solution. Specifically we distinguish

case A:  $\delta \in (25.5^\circ, 44.5^\circ)$ ;

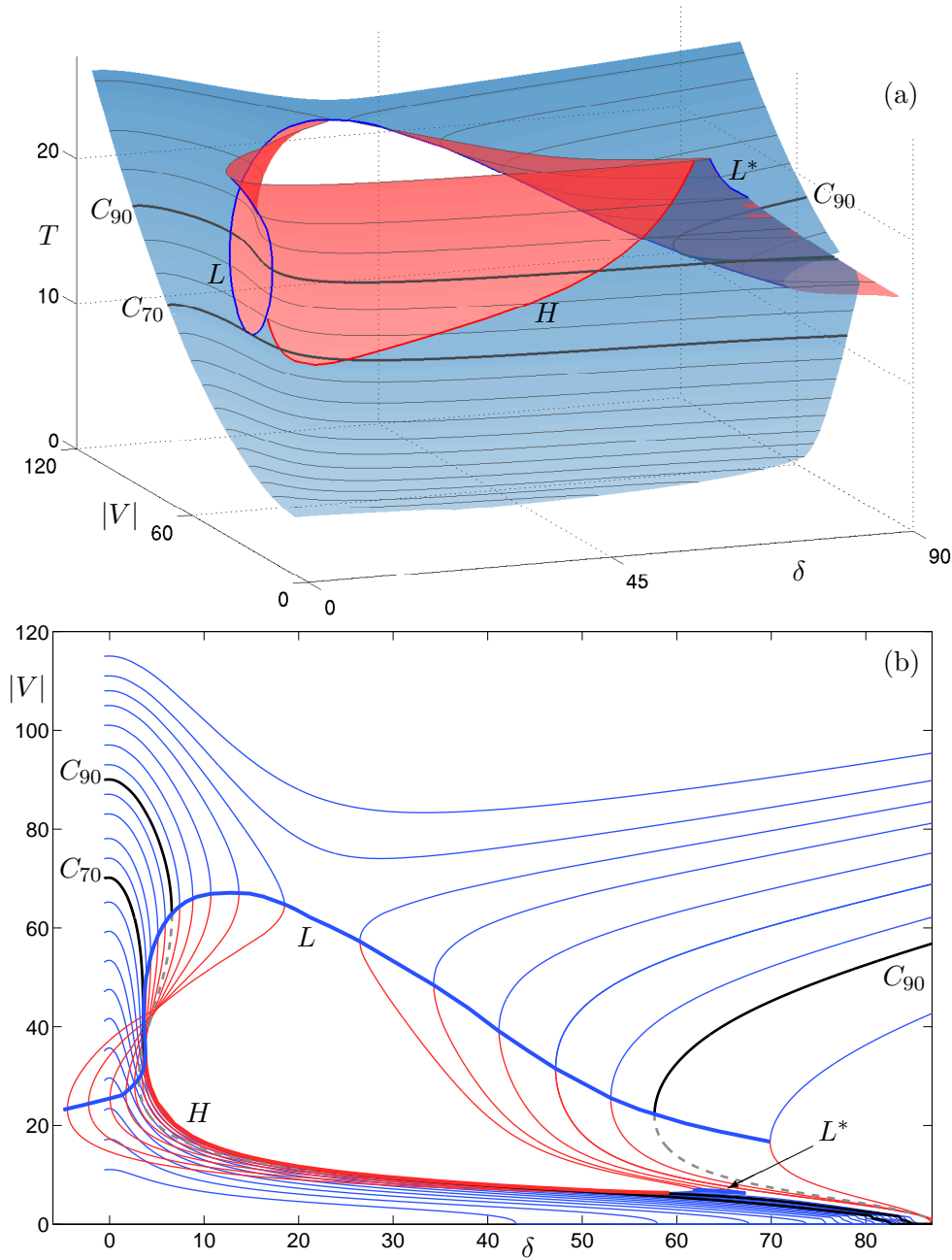


**Figure 2.7.** Panel (a) shows the surface of turning solutions in  $(|V|, \delta, T)$ -space. The loci of limit point bifurcations  $L$  and  $L^*$  and the locus of Hopf bifurcations  $H$  are indicated by a thick lines; the blue part of the surface below  $H$  and  $L$  consists of stable solutions, and the red part above of unstable solutions. Individual solution branches used to create the surface are shown at regular intervals as thin black curves. The solution branches shown in Figures 2.4(a) and 2.6(a) are highlighted by thick black lines and labelled  $C_{70}$  and  $C_{90}$ , respectively. Panel (b) shows a corresponding contour plot of individual contours in the  $(|V|, \delta)$ -plane. In the contour plot, the stability of the curves  $C_{70}$  and  $C_{90}$  has been indicated as in Figures 2.4(a) and 2.6(a).

case B:  $\delta \in (17.5^\circ, 25^\circ)$ ;

case C:  $\delta \in (7^\circ, 17^\circ)$ ;

case D:  $\delta \in (4.5^\circ, 6.5^\circ)$ .

The boundary between the regions A and B is the point where the minimum velocity of the periodic solution first reaches  $|V| = 0$ . Similarly the transition from C to D is associated with the minimum velocity becoming non-zero again.

Figure 2.8 shows CG curves plotted in the  $(X, Y)$ -plane over one period of motion with corresponding time history plots of the aircraft velocity  $|V|$  and the slip angle  $\alpha$ . Plotted is the stable behaviour at  $\delta$ -values that are representative for the four intervals A–D shown in Figure 2.6. Across each region the behaviour is qualitatively the same. The aircraft slip angle gives the aircraft's orientation relative to its direction of motion. Recall that the slip angle is used to calculate the orientation of the markers on the CG curves. For each of the cases A–D there are common features that can be identified. The data is plotted over one period taken between points of maximum velocity. Therefore, the initial points represent the aircraft approximately following the unstable turning circle but at a slightly higher velocity. The turning circle solution is unstable so the aircraft deviates from it, loses velocity and comes to a near or full stop. The point of minimum velocity corresponds to the point of maximum curvature on the aircraft CG curve. Due to the constant thrust, the aircraft then speeds up once more, approaching the turning circle before again reaching the maximum velocity at the final point. From the plots in the left column a longer trajectory is obtained by repeatedly copying and translating each trajectory so that the start and final points connect. Figure 2.5(c1) is an example of what such a trajectory looks like.

The time plots in the right column of Figure 2.8 are divided into numbered time intervals each representing a qualitative state of the aircraft. Transitions between the intervals indicate a qualitative change. For example, for case A the transition between A3 and A4 corresponds to the modulus of the aircraft slip angle  $|\alpha|$  exceeding  $90^\circ$ . This means that the aircraft has rotated beyond slipping sideways relative to its direction of motion and has a backwards component to its motion. Clearly it is necessary to look at other features of the aircraft behaviour to fully explain all these transitions. Therefore we now introduce a diagrammatic representation that takes into account many aspects of the aircraft's behaviour, to give a very detailed account in each case.

The overall behaviour in regions A–D is as follows. In case A when the aircraft deviates from the unstable turning circle solution it enters a skid and loses velocity until the skid is recovered and the aircraft starts to approach the unstable turning circle solution again as it speeds up. In case B the aircraft enters a skid in a similar fashion to case A but skids round almost  $180^\circ$  and rolls backwards before coming to a complete stop. Case C is similar to B, but now the aircraft skids through  $180^\circ$  and briefly follows a backwards turning circle before stopping. In cases B and C the skid is only recovered when the aircraft comes to a halt. After stopping it speeds up again and approaches the unstable turning circle solution. In case D the aircraft enters a skid and makes a full rotation relative to its CG curve without coming to a stop. The skid is only recovered when the aircraft is travelling forwards again.

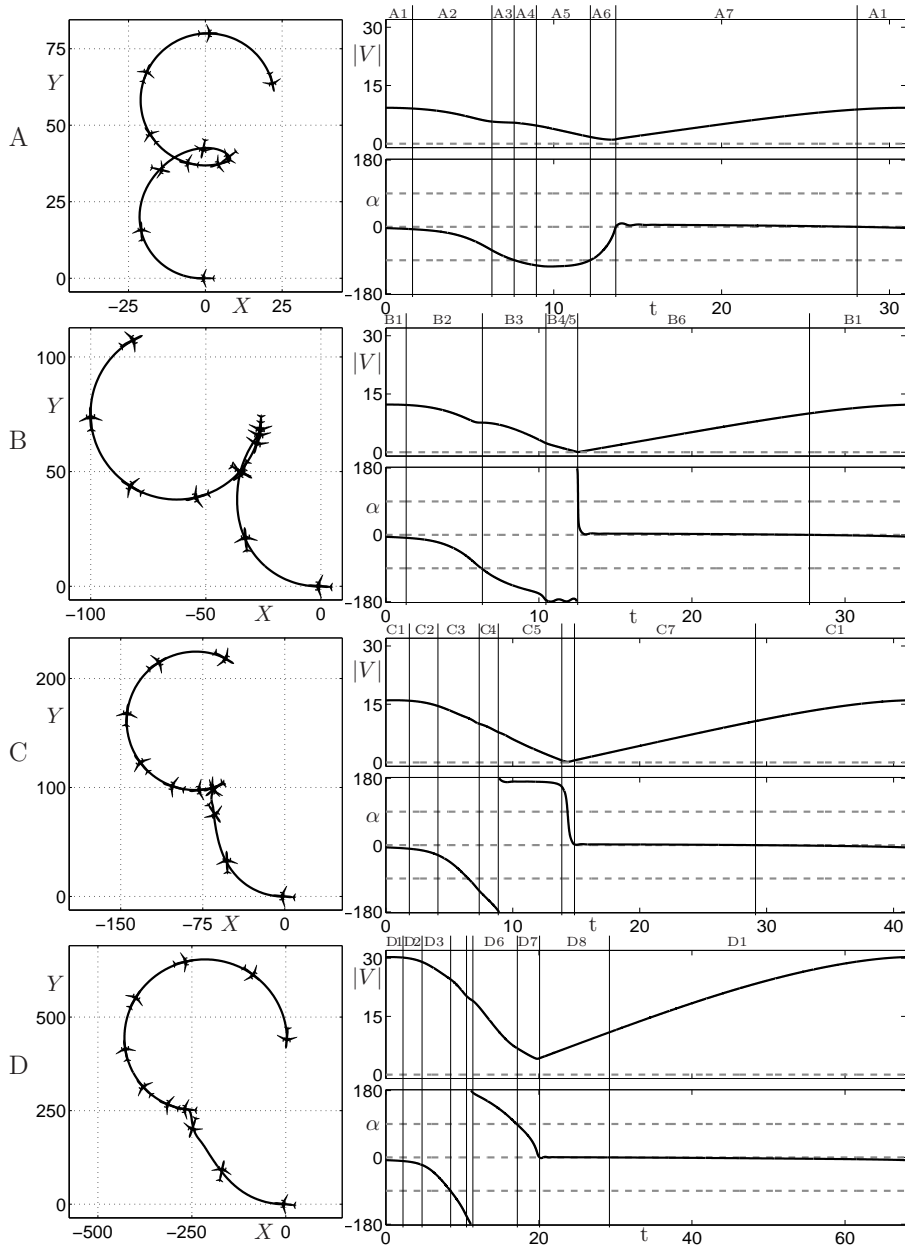


**Figure 2.8.** Panels on the left show aircraft trajectories exhibiting the qualitatively different periodic behaviour in the regions A-D shown in Figure 2.6(a). Panels on the right are the corresponding plots of the aircraft velocity  $|V|$  and aircraft slip angle  $\alpha$  against time  $t$  for each case. In the time plots the lines  $|V| = 0$ ,  $\alpha = 0$  and  $\alpha = \pm 90$  are represented by dashed grey lines. These time history plots are divided into time intervals which correspond with the changing aircraft states described in Figures 2.9, 2.10, 2.11 and 2.12.

### 2.4.1 Diagrammatic representation

Figures 2.9–2.12 each show time plots of the nose tyre slip angle  $\alpha_N$  and main outer tyre slip angle  $\alpha_M$  for the cases A–D. We do not distinguish between the behaviour of the inner and outer main gears as both gears act practically simultaneously in the cases studied. The tyre forces are larger on the outer gear due to a greater load. Therefore, the slip angle of the outer gear  $\alpha_M$  is used to represent the behaviour of both the main gears. In the time history plots of Figures 2.9–2.12 there is a dashed black line indicating the optimal slip angle at which the tyre will generate the greatest holding force. These plots show concurrent information with the plots in Figure 2.8. The plots are divided into numbered regions for which a given aircraft state can be identified.

For each of the numbered regions in the time plots of Figures 2.9–2.12 there is a corresponding diagram at the top of the figure. Each diagram shows several pieces of information about the state of the aircraft. Recall that the aircraft markers in the CG curve plots of Figure 2.8 indicate the slip angle of the aircraft, that is, the angle it makes with its direction of motion. The direction of motion is indicated in the diagrams in Figures 2.9–2.12 by an arrow originating from the CG position that is pointing to the left. The slip angle of the aircraft in the diagrams is indicated schematically as one of the values  $\alpha = \pm 10^\circ, \pm 45^\circ, \pm 135^\circ, \pm 170^\circ$ . The direction of rotation of the aircraft, taken from the sign of the rotational velocity of the aircraft, relative to the CG curve is shown about a representative centre of rotation; it may be in front of the nose gear, between the nose and main gears, or behind the main gears. The (approximate) location of the three landing gears is represented by two black tyres, the nose and outer main gear, and a grey tyre, the inner main gear. Recall that we consider the main gears to act simultaneously and therefore only represent the behaviour at the outer gear. The directions of tyre forces are shown on the nose gear and main outer gear. From each of the nose and main outer gears originates a double arrow indicating the direction of the tyre force as determined by the sign of the tyre slip angles  $\alpha_{N,M}$ . Passing through the lines  $\alpha_{N,M} = 0^\circ$  or  $\alpha_{N,M} = \pm 180^\circ$  indicates that the direction of the tyre force changes. The size of these arrows is uniform, and does not indicate the magnitude of the forces. Finally, a single arrow is shown opposing the tyre force direction if that particular tyre is skidding. In general, when the tyres are rolling and generating a holding force sufficient to control the aircraft the slip angles will change gradually. A tyre is identified as skidding if the slip angle crosses through the optimal holding force line and the slip angle starts to change rapidly. A tyre is identified as having recovered from skidding when the time derivative of its slip angle returns towards 0 (the slip angle curve plateaus out).

### 2.4.2 Detailed discussion of cases A–D

We now discuss the aircraft dynamics for the cases A–D. After a brief summary each periodic state of the aircraft is explained in detail. The reader will find it useful to refer back to Figure 2.8.

**Case A:**  $\delta \in (25.5^\circ, 44.5^\circ)$ ; as shown in Figure 2.9. Initially the aircraft is at the maximum velocity and has started to deviate from the unstable turning circle solution; the velocity then drops as the main tyres start skidding. The aircraft continues to slow down. The skid is recovered when the aircraft reaches its minimum velocity. The aircraft approximately follows a turning circle as it speeds up from the minimum velocity. In more detail:

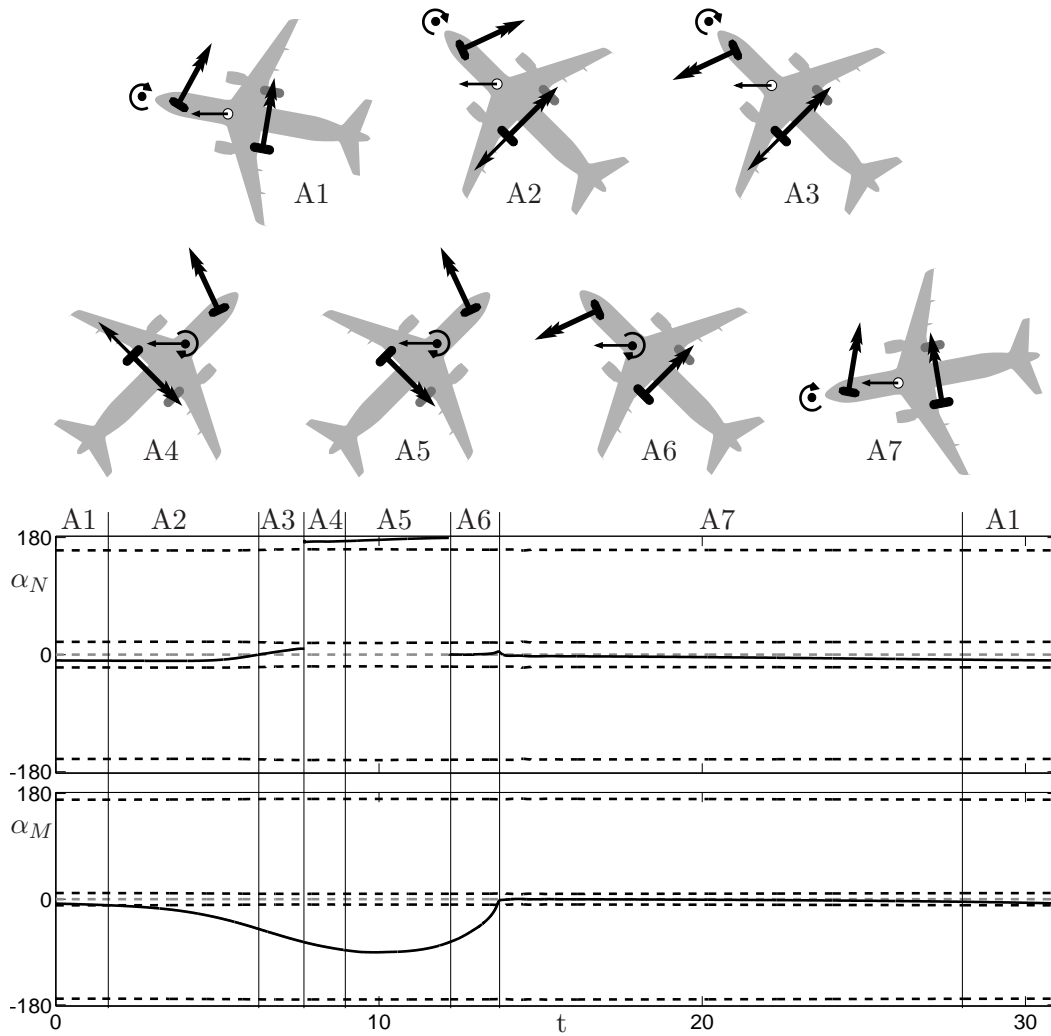


**Figure 2.9.** Diagrammatic representation of the periodic behaviour of the aircraft for region A in Figure 2.6. The two panels show the nose tyre slip angle  $\alpha_N$  and main tyre slip angle  $\alpha_M$  over one period (black curves). The optimal slip angle values are shown by dashed black lines. The line  $\alpha_{N,M} = 0$  is shown as a dashed grey line. Each aircraft diagram represents the aircraft's state over the numbered time intervals on the time history panels.

- A1 The aircraft approximately follows the unstable turning circle solution, held by tyre forces; i.e. it rotates clockwise about a point in front of the nose gear and the aircraft slip angle  $\alpha$  is small. The aircraft slip angle  $\alpha$  increases as the aircraft gains velocity and gradually starts to oversteer.
- A2 The main tyres saturate (in quick succession, inner followed by outer) and start to skid. The main tyre slip angle  $\alpha_M$  passes through the optimal slip angle line after which its slope increases rapidly. The aircraft begins to oversteer excessively and the aircraft slip angle  $\alpha$  changes rapidly, the rotational velocity of the aircraft increases.
- A3 The main gears continue to skid. The force on the nose gear switches ( $\alpha_N$  changes sign) to oppose the rotation of the aircraft causing the rotational velocity to fall.
- A4 As A3 but the slip angle exceeds  $|\alpha| > 90^\circ$  (see Figure 2.8) — the aircraft moves beyond sliding sideways with a slight backward component to the motion. The centre of rotation of the aircraft moves through the nose gear causing a sudden jump in its slip angle  $\alpha_N$ .
- A5 Main tyres regain traction, evidenced by the main tyre slip angle  $\alpha_M$  plateauing out, so both the nose tyres and main tyres oppose the spin — effectively bringing the spin under control. The slip angle of the aircraft  $\alpha$  plateaus out as it regains control.
- A6 The aircraft has stopped skidding and starts to travel forwards again; the slip angle has fallen below  $|\alpha| = 90^\circ$  and therefore, there is no backward component to its motion. It continues to slow down towards its minimum velocity. Although the main tyre slip angle  $\alpha_M$  changes rapidly, it is moving towards the optimal slip angle line and the tyre force is increasing.
- A7 When the aircraft reaches its minimum velocity the sign of  $\alpha_N$  changes so that the direction of the nose tyre force matches the main gears. The aircraft speeds up and starts to follow an approximate turning circle. Initially, whilst travelling at low velocity the aircraft understeers slightly before starting to oversteer at the transition back into A1.

Note: For  $\delta \in (40.5^\circ, 44.5^\circ)$  in case A the aircraft slip angle does not exceed  $|\alpha| > 90^\circ$  and in this case the steps A4 and A5 do not occur in Figure 2.9.

**Case B:**  $\delta \in (17.5^\circ, 25^\circ)$ ; as shown in Figure 2.10. The aircraft enters a skid in a similar way to case A but does not recover from the skid. The aircraft skids round almost  $180^\circ$  and only stops skidding when the tyres are rolling backwards. The aircraft rolls backwards, oscillating from side to side with a slip angle just greater than  $\alpha = -180^\circ$ . The constant forward thrust brings the aircraft to a halt, the slip angle  $\alpha$  passes through  $\alpha = -180^\circ$  to become positive and returns rapidly towards  $\alpha \approx 0^\circ$  as the aircraft starts moving forwards again. The significant difference with case A is that the aircraft makes a full rotation relative to the CG curve and also that the aircraft comes to a complete halt ( $|V| = 0$ ). After coming to a halt it starts to move off again following an approximate turning circle. In more detail:

B1 As A1.

B2 As A2.

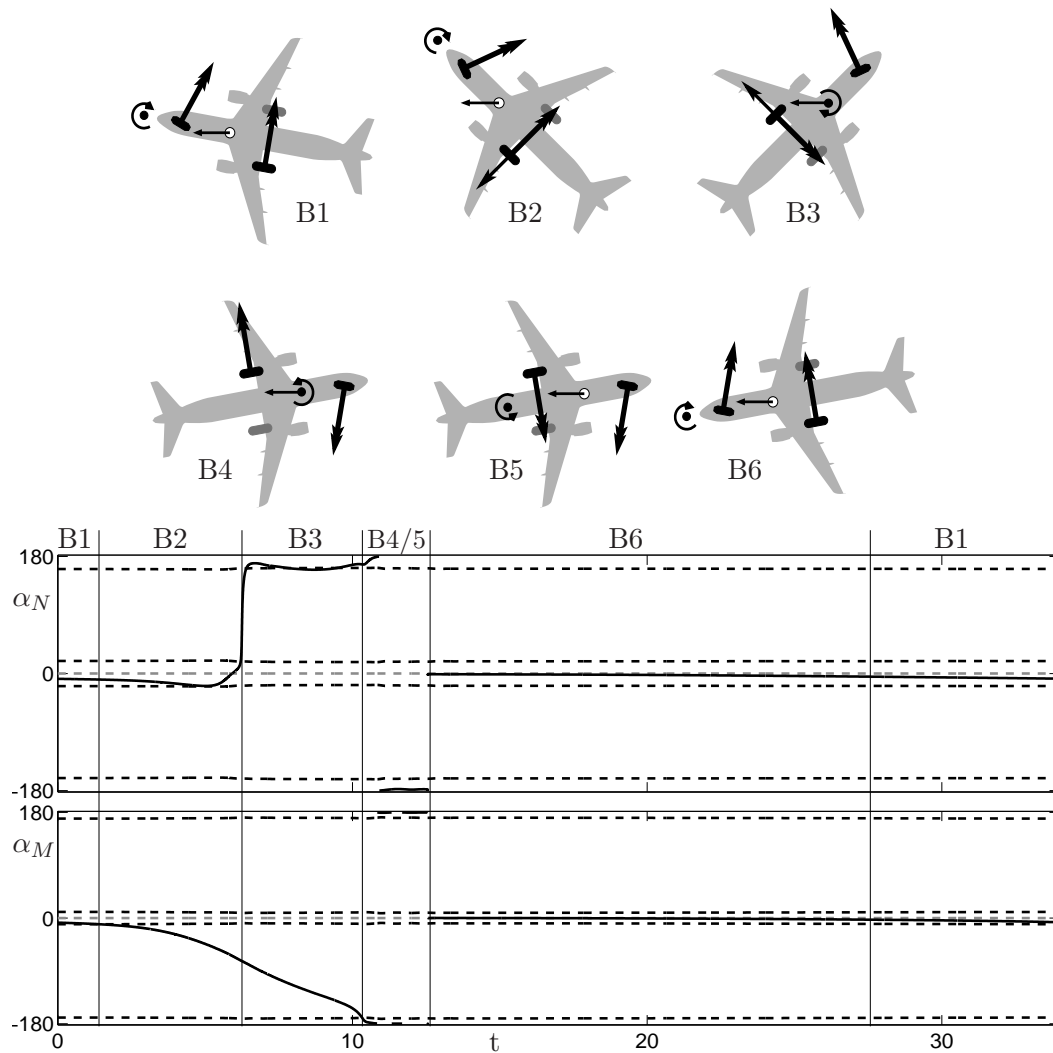


**Figure 2.10.** Diagrammatic representation of the periodic behaviour of the aircraft for region B as shown in Figure 2.6. The two panels show the nose tyre slip angle  $\alpha_N$  and main tyre slip angle  $\alpha_M$  over one period (black curves). The optimal slip angle values are shown by dashed black lines. The line  $\alpha_{N,M} = 0$  is shown as a dashed grey line. Each aircraft diagram represents the plane's state over the numbered time intervals on the time history panels.

- B3 The direction of the force on the nose gear changes as the aircraft starts to rotate about a point between the nose and main gears. Simultaneously the slip angle exceeds  $|\alpha| > 90^\circ$ . Qualitatively the same as A4, effectively missing out A3 because the aircraft rotates faster in the skid.
- B4/5 The aircraft skids round far enough such that the tyres regain traction whilst rolling backwards. The aircraft slip angle  $\alpha$  plateaus out into a region of small oscillations just above  $\alpha = -180^\circ$ . As the aircraft travels backwards the momentum from the skid causes it to roll from side to side (the wings pitch up and down). The forces on the main tyres switch from side to side and the direction of rotation alternates, switching between B4 and B5. As the aircraft is travelling backwards the constant thrust rapidly slows it down, bringing it to a complete halt. The slip angle passes through  $\alpha = -180^\circ$ , becoming positive and rapidly returning towards  $\alpha = 0^\circ$ .
- B6 The aircraft moves off from stationary following an approximate turning circle; as A7.

**Case C:**  $\delta \in (7^\circ, 17^\circ)$ ; as shown in Figure 2.11. The aircraft enters a skid in a similar fashion to cases A and B, but it skids over  $180^\circ$  before the tyres stop skidding. The aircraft briefly follows a backwards turning circle whilst the forward thrust slows it down. Although the translational velocity reaches  $|V| = 0$ , it still has rotational velocity at that point. The significant difference from case B is that the aircraft tyres regain traction after it has spun over  $180^\circ$ , i.e. the slip angle has passed through  $\alpha = -180^\circ$ . The momentum from the skid maintains a rotational velocity when the aircraft travels backwards. After stopping (translationally, not rotationally) the aircraft then moves off following a turning circle in the forward direction. In more detail:

- C1 As A1 and B1.
- C2 As A2 and B2.
- C3 The aircraft has more momentum as, in this case, the velocity is higher when the aircraft enters a skid. Traction on the main and nose tyres is lost before the aircraft slides past  $\alpha = 90^\circ$ . In contrast to the previous cases, all tyres are skidding. The slope of the aircraft slip angle  $\alpha$  increases.
- C4 The direction of the force on the nose tyre switches and the centre of rotation moves to a position between the main and nose gears. All the tyres oppose the direction of rotation but are skidding. The aircraft slip angle  $\alpha$  continues to change rapidly.
- C5 The aircraft slip angle moves through  $\alpha = -180^\circ$  after which the main tyres and the nose tyres regain traction. The aircraft follows a backwards turning circle with a small, almost constant aircraft slip angle  $\alpha$ . The main tyre slip angle  $\alpha_M$  remains very small and does not change sign once (although this is not indicated in the diagram).
- C6 The aircraft (translational) velocity reaches  $|V| = 0$  instantaneously but as it passes through this point it still has rotational velocity. The momentum of the aircraft causes it to carry on rotating in the same direction as it travels backwards. The aircraft starts to accelerate again, moving in a forward direction, due to the constant thrust.
- C7 As A7 and B6.

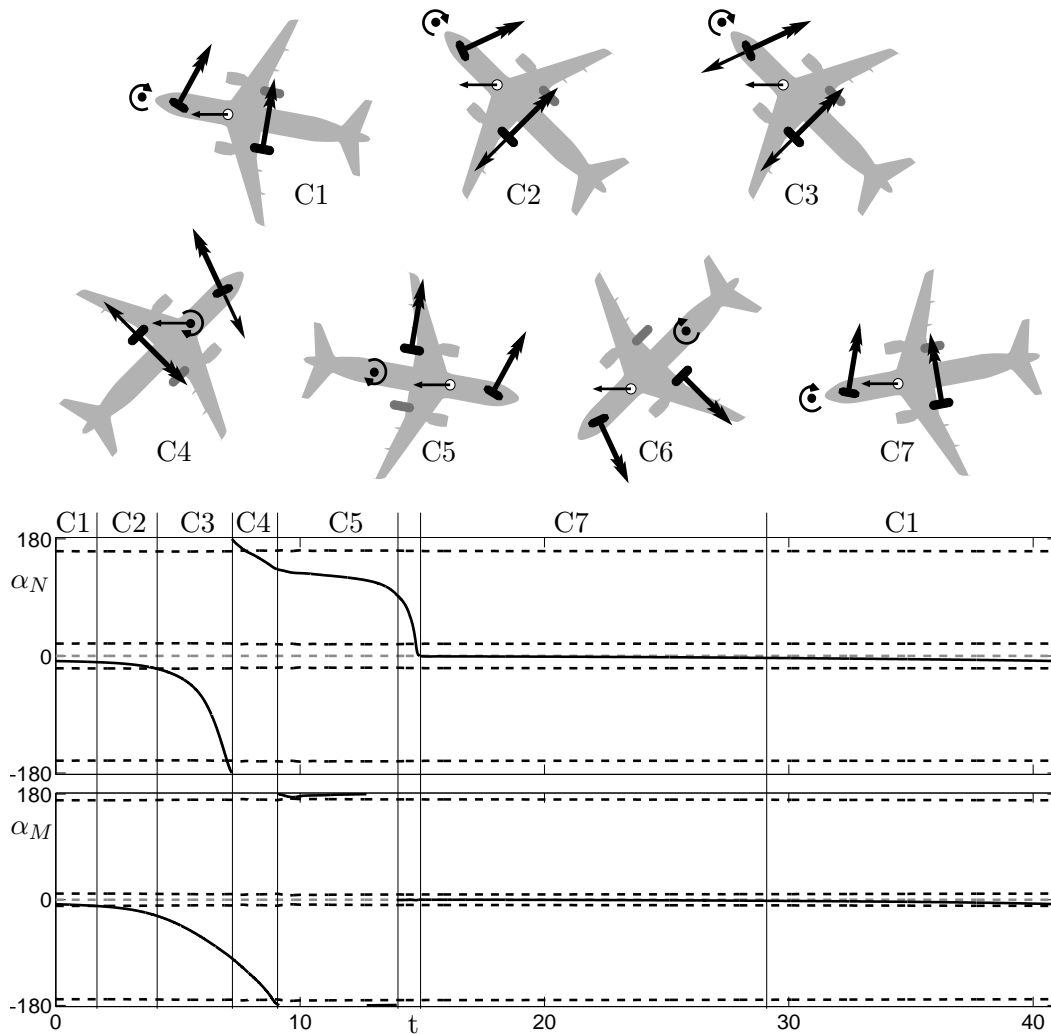


**Figure 2.11.** Diagrammatic representation of the periodic behaviour of the aircraft for region C as shown in Figure 2.6. The two panels show nose tyre slip angle  $\alpha_N$  and main tyre slip angle  $\alpha_M$  over one period (black curves). The optimal slip angle values are shown by dashed black lines. The line  $\alpha_{N,M} = 0$  is shown as a dashed grey line. Each aircraft diagram represents the plane's state over the numbered time intervals on the time history panels.

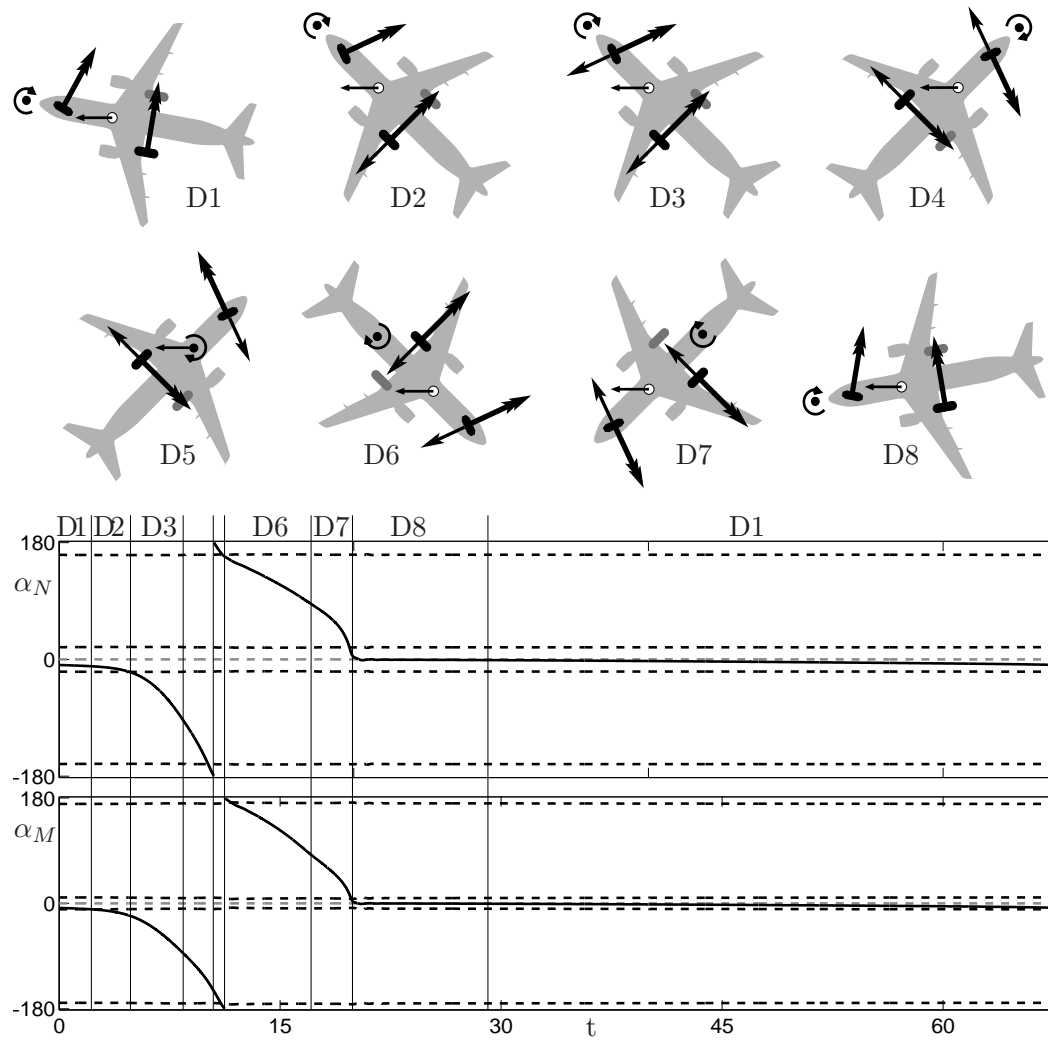


**Figure 2.12.** Diagrammatic representation of the periodic behaviour of the aircraft for region D as shown in Figure 2.6. The two panels show the nose tyre slip angle  $\alpha_N$  and main tyre slip angle  $\alpha_M$  over one period (black curves). The optimal slip angle values are shown by dashed black lines. The line  $\alpha_{N,M} = 0$  is shown as a dashed grey line. Each aircraft diagram represents the plane’s state over the numbered time intervals on the time history panels.

**Case D:**  $\delta \in (4.5^\circ, 6.5^\circ)$ ; as shown in Figure 2.12. The aircraft enters a skid at a higher velocity than the previous cases. The aircraft has more momentum, so that it makes a full  $360^\circ$  spin relative to the CG curve before traction on the tyres is regained. In contrast to the previous two cases, when the aircraft travels backwards the tyres continue skidding. Once the aircraft is facing forwards after the spin it has lost sufficient momentum for the tyres to stop skidding and the aircraft returns to following an approximate turning circle. In more detail:

D1 As A1, B1 and C1.

D2 As A2, B2 and C2.

D3 As C3.

D4 The aircraft continues to skid, the slip angle exceeding  $\alpha = 90^\circ$  before direction of the force on the nose gear changes. The centre of rotation stays at a point in front of the nose gear.

D5 As C4.

D6 The aircraft spins through  $\alpha = 180^\circ$ , the tyres not regaining traction. The force on the main tyres changes direction and the aircraft now spins about a point behind the main gears.

D7 The aircraft continues to rotate and return towards facing forwards whilst slowing to a low velocity.

D8 As the aircraft returns to travelling in a forward direction ( $\alpha \approx 0$ ) the tyres regain traction and the aircraft speeds up following a turning circle; as A7, B6 and C7.

Cases A–D above provide a complete explanation of the behaviour when lateral stability of the aircraft is lost. From case to case the velocity at which lateral stability is lost increases. Therefore, more momentum is available so that aircraft undergoes a larger rotation before the tyres regain traction. The level of detail shown in our new diagrammatic representation is necessary in order to fully explain the different types of periodic behaviour and the transitions between them.

## 2.5 Discussion

A bifurcation analysis of the turning manoeuvres of an Airbus A320 on the ground was presented. Focusing on a particular aircraft configuration, the stability of turning circle solutions was computed over the entire range of relevant values of steering angle and thrust. It is the stability of these turning circle solutions that dictates whether a particular turning manoeuvre at specific parameter values is laterally stable. The results were rendered as a surface plot, which was constructed from continuation runs with varying steering angle  $\delta$  at discrete fixed thrust levels. The modulus of the velocity of the aircraft  $|V|$  was used in this representation, meaning that the surface is represented in  $(\delta, |V|, T)$ -space. We found that the single parameter continuation curves corresponding to fixed thrust levels are qualitatively the same over

large ranges of thrust. Due to this robustness in the structure of the surface it was possible to fully explain the dynamics represented on the surface by studying two individual thrust cases in detail. These two cases were explained in terms of the solutions represented by the bifurcation diagrams. Examples were given of branch switching near limit point bifurcations and of the periodic solutions that arise from Hopf bifurcations. In this way two significant types of behaviour were identified: stable turning circle solutions and periodic solutions for which the aircraft loses lateral stability, entering a skid or even a spin.

As an example of how bifurcation analysis can uncover even quite subtle effects of practical interest, we consider the dynamics near the limit point  $L_1$  in Figure 2.6(a). On the stable branch close to  $L_1$ , a small increase in the steering angle beyond the bifurcation leads to a transition to the low-velocity part of the solution branch. In this case the aircraft moves to a laterally unstable behaviour over a transient period. It is not immediately obvious how to relate this observation to inherent properties of the aircraft system that could be monitored. At high velocity the aerodynamic forces generated by the aircraft's vertical tail attempt to keep the aircraft travelling in a straight line. As the steering angle is increased and the limit point is approached two things happen. The turning moment generated by the nose gear tyres is increasing and the aerodynamic holding force decreases (with the aircraft velocity). The limit point corresponds to the aerodynamic holding force being overcome by the turning moment generated at the nose gear. This observation shows that bifurcation analysis can reveal features of the dynamics that otherwise would not be immediately evident.

In conjunction with the bifurcation analysis, model simulations were used to study periodic orbits in the region of unstable turning solutions. A detailed explanation of the dynamics was given by means of a diagrammatic representation of changing states of the aircraft. The focus was on attributing qualitative changes in the behaviour under parameter variation to the saturation of the forces generated by individual tyres. Four regions of qualitatively different behaviour were identified, and the differences and transitions between them explained. The diagrammatic explanation gave details of the undesirable behaviour when the aircraft loses lateral stability. The safe operating limits that avoid this behaviour, have been identified over the relevant ranges of steering angle and thrust by the bifurcation analysis. Specifically, our results identify that for high-velocity turns, such as when exiting the runway, maintaining a steering angle below  $\delta = 3.5^\circ$  ensures lateral stability. This value agrees with empirical data, and it is used in the A320's steering system as a limit for high-velocity turns. Furthermore, a curve of Hopf bifurcations in the steering angle versus thrust parameter space is identified as the boundary for lateral stability (safe operation) when performing manoeuvres at lower velocities.



# Chapter 3

## Operational parameter study

The model and results presented in Sections 3.2, 3.3 and 3.4 have been published in [44]; the results in Section 3.5 appeared in [43].

### 3.1 Introduction

In this chapter we develop a fully parameterized, mathematical model of an aircraft turning on the ground; effectively, the full equations of motion for the model outlined in Chapter 2 are given. We demonstrate that the new model allows us to extend previous work with a bifurcation study in terms of several operational parameters. The new mathematical model takes the form of a system of coupled ordinary differential equations (ODEs). The airframe is considered as a rigid body with six DOF and the equations of motion are derived by balancing the respective forces and moments. Specific sub-components are modelled in accordance with industry experience and test data, and nonlinear effects are included in the models of the tyres and the aerodynamics. In this way, the overall mathematical model incorporates an appropriate level of complexity. This new mathematical model provides several advantages over the existing SIMMECHANICS model used in Chapter 2, especially when used with continuation software. Its general functionality and computational efficiency with the software package AUTO is dramatically improved. Furthermore, the model does not suffer from a black-box nature, which means that all variables and parameters — both design parameters (such as dimensions of the aircraft) and operational parameters (such as total mass and CG position) — are fully accessible.

The development of the mathematical model was guided by the SIMMECHANICS model described in Section 2.2. Following the implementation of the mathematical model, the first goal was its validation via a direct comparison with existing results from Chapter 2. The validation is demonstrated with a one-parameter bifurcation analysis that focuses on the agreement between different types of solutions in each model. In particular, stable turns and periodic solutions for which the aircraft loses lateral stability are studied. The solutions are presented across the full range of the steering angle for a particular aircraft setup, allowing for a comprehensive comparison between the models.

We then present an extensive bifurcation analysis of turning solutions of the aircraft under variation of several operational parameters. One-parameter continuation runs are computed in

the steering angle at many discrete values of the CG position (over a suitable range). Two-parameter continuation is used to follow curves of bifurcation points directly to determine regions where turning is unstable. As in Chapter 2, the results are represented as surfaces of solutions that describe the possible dynamics over the full range of the two parameters, the steering angle and the centre of gravity position. Moreover, we find that a curve of limit point bifurcations forms a fold in the surface of solutions; crossing this curve in parameter space results in a significant change in the radius of the turning circle that the aircraft attempts to follow. In contrast with Chapter 2 we find closed curves of Hopf bifurcations; however, these curves still bound regions of unstable turning solutions for which the aircraft follows a laterally unstable motion relative to the unstable turning solution. The robustness of these results is further investigated under the variation of the aircraft mass and the thrust level. We find that quite small changes in thrust result in a sequence of qualitative changes of the solution surface. This occurs for two different mass cases (heavy and light aircraft) but at different thrust levels. Overall, a heavier aircraft will make stable turns over a larger range of centre of gravity positions and at higher thrust levels. We also find that the region of laterally unstable behaviour grows more rapidly with increased thrust for a lighter aircraft.

An investigation into differences in taxiway surface conditions reveals an interesting relation to the results in Chapter 2. We find that reducing the coefficient of friction of the tyres has the same qualitative effect as increasing the thrust level. This is shown by the qualitative agreement between surfaces of solutions computed in terms of the two parameters. We are further able to elaborate on results presented in Chapter 2 with a detailed investigation of the apparent jump in the amplitude of oscillations that was found to occur close to a Hopf bifurcation. An advantage of the mathematical model is that we are able to compute branches of periodic solutions directly (instead of with time history simulation). With a combination of different continuation computations and time history simulations we are able to provide a theoretical explanation for the sharp increase in oscillation amplitude and gain further insight into the mechanism through which the lateral stability of the aircraft is lost.

The chapter is organised as follows: In Section 3.2 full details of the new model are given. Its validation against the existing SIMMECHANICS model is demonstrated in Section 3.3. An extensive bifurcation analysis in several parameters is the subject of Section 3.4. The effect of reducing tyre friction is investigated in Section 3.5. In Section 3.6 a sharp increase in the amplitude of periodic oscillations close to a Hopf bifurcation is discussed. Finally, conclusions and directions of future work are presented in Section 3.7.

## 3.2 Mathematical model

In this section we give details of the derivation and implementation of a fully parameterized mathematical model that describes an aircraft moving on the ground. As in Chapter 2 the chosen parameter values and component models represent an A320, however, the model parameters could easily be adapted to represent almost any passenger aircraft. We give a full description of the mathematical model in this chapter; it is effectively a fully parameterized mathematical version of the SIMMECHANICS model. Therefore, to keep this chapter self-contained, there is some repetition from Section 2.2. Motivations for its development are: to overcome the black-box nature of a model written in SIMMECHANICS (especially concerning full access to relevant system parameters), to improve functionality with the continuation

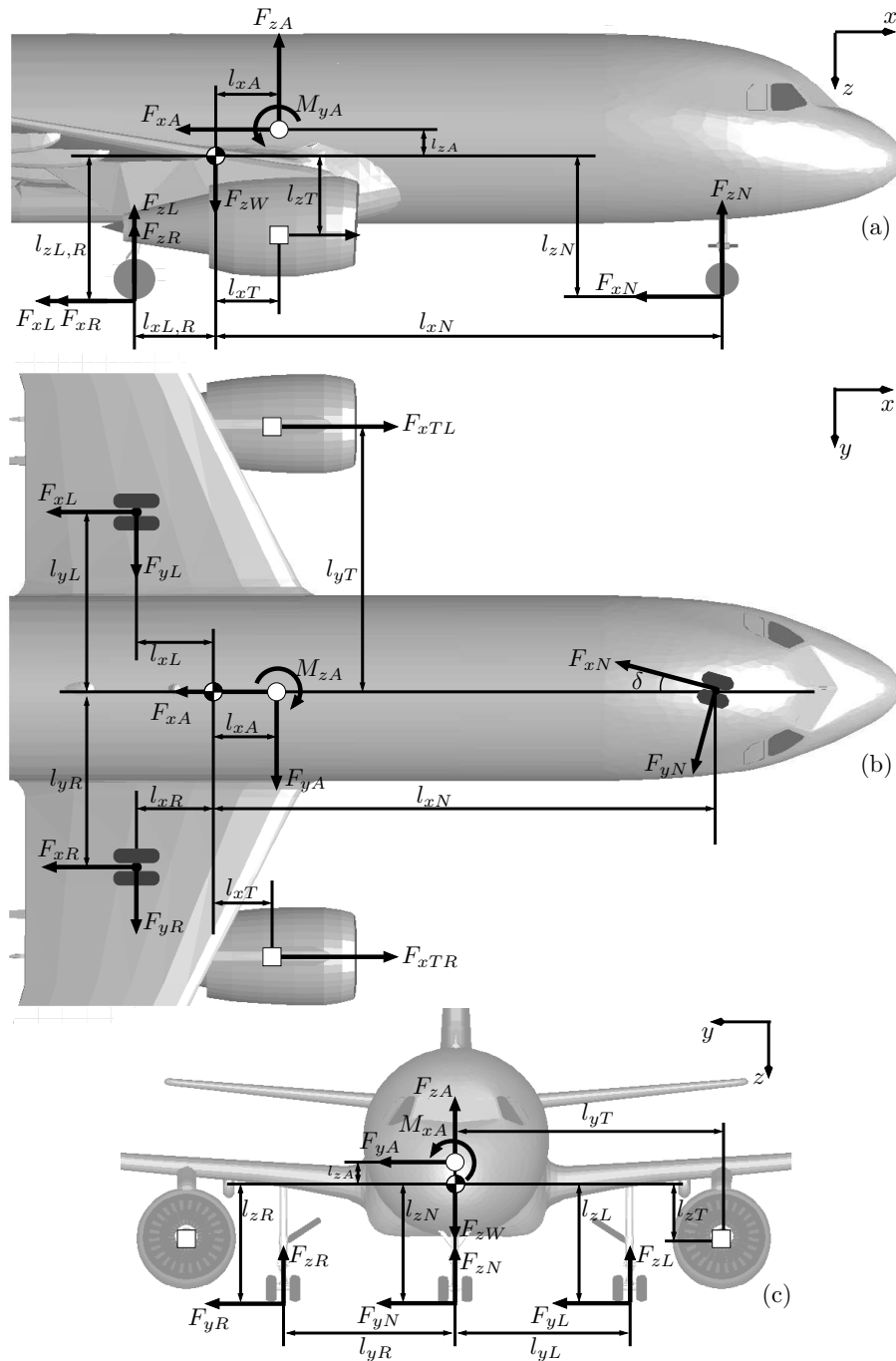


**Figure 3.1.** Schematic diagram showing relative positions of force elements  $F_*$  acting on the airframe with dimensions defined by  $l_*$  in Table 3.1. Three projections are shown in the aircraft's body coordinate system: the  $(x, z)$ -plane in panel (a), the  $(x, y)$ -plane in panel (b), and the  $(y, z)$ -plane in panel (c). The centre of gravity position is represented by a checked circle, the aerodynamic centre by a white circle and the thrust centre of each engine by a white square.

package AUTO [12], and to increase the computational efficiency so that more elaborate bifurcation studies become feasible. The mathematical model has been derived via force and moment equations, coupled to relevant subsystem descriptions. It has been fully validated against the existing SIMMECHANICS model; see Section 3.3.

The aircraft modelled here has a tricycle configuration in which the nose gear is used for steering. We model the aircraft as a single rigid body with DOF; three translational DOF and three rotational DOF. On the aircraft there are two tyres per gear. Due to the small separation distance they can be assumed to act in unison and, hence, are described as a single tyre in the model. We do not include oleos in the model presented here, that is, we assume the landing gears to be rigid. The reason for this simplifying assumption is that oleo dynamics are not excited in turning as considered in the bifurcation study in Section 3.4. Oleos could be included into the model, but at the expense of increasing its dimensionality.

Throughout this study we use one of the conventionally accepted coordinate systems for aircraft. Specifically, the positive  $x$ -axis points along the centre-line of the fuselage toward the nose of the aircraft, the  $z$ -axis is toward the ground and the  $y$ -axis completes the right-handed body-fixed coordinate system. This body coordinate system is assumed to coincide with the aircraft's principal axes of inertia, a reasonable assumption due to symmetries of the airframe. The equations of motion were derived from Newton's Second Law by balancing either the forces or moments in each degree of freedom [14].

In Figure 3.1 the relative positions and directions of the force elements that act on the aircraft are shown in the three standard projections. These diagrams illustrate how the equations of motion are derived by the balancing of force elements along each axis and moment elements about each axis. The equations of motion for the velocities in the body coordinate system of the aircraft are given as six ordinary differential equations (ODEs):

$$m(\dot{V}_x + V_z W_y - V_y W_z) = F_{xTL} + F_{xTR} - F_{xR} - F_{xL} - F_{xN} \cos(\delta) - F_{yN} \sin(\delta) - F_{xA} + F_{zW} \sin(\theta), \quad (3.1)$$

$$m(\dot{V}_y + V_x W_z - V_z W_x) = F_{yR} + F_{yL} + F_{yN} \cos(\delta) - F_{xN} \sin(\delta) + F_{yA} + F_{zW} \sin(\phi), \quad (3.2)$$

$$m(\dot{V}_z + V_y W_x - V_x W_y) = F_{zW} \cos(\theta) \cos(\phi) - F_{zR} - F_{zL} - F_{zN} - F_{zA}, \quad (3.3)$$

$$I_{xx} \dot{W}_x - (I_{yy} - I_{zz}) W_y W_z = l_{yL} F_{zL} - l_{yR} F_{zR} - l_{zL} F_{yL} - l_{zR} F_{yR} - l_{zN} F_{yN} \cos(\delta) + l_{zN} F_{xN} \sin(\delta) + l_{zA} F_{yA} + M_{xA}, \quad (3.4)$$

$$I_{yy} \dot{W}_y - (I_{zz} - I_{xx}) W_x W_z = l_{xN} F_{zN} - l_{zN} F_{xN} \cos(\delta) - l_{zN} F_{yN} \sin(\delta) - l_{xR} F_{zR} - l_{zR} F_{xR} - l_{xL} F_{zL} - l_{zL} F_{xL} + l_{zT} F_{xTL} + l_{zT} F_{xTR} + l_{zA} F_{xA} + l_{xA} F_{zA} + M_{yA}, \quad (3.5)$$

$$I_{zz} \dot{W}_z - (I_{xx} - I_{yy}) W_x W_y = l_{yR} F_{xR} - l_{yL} F_{xL} - l_{xR} F_{yR} - l_{xL} F_{yL} + l_{xN} F_{yN} \cos(\delta) - l_{xN} F_{xN} \sin(\delta) + l_{xA} F_{yA} + l_{yT} F_{xTL} - l_{yT} F_{xTR} + M_{zA}. \quad (3.6)$$

Here a dot notation is used to show the first derivative with respect to time of these states. The dimensions  $l_*$ , given in Table 3.1, are defined in terms of the centre of gravity position which is parameterized as  $CG$ . The parameter  $CG$  is defined as a percentage measured along the

mean aerodynamic chord  $l_{mac}$ , taken from the leading edge. The aircraft mass  $m$  as defined for two cases presented in the bifurcation analysis is given in Table 3.1; corresponding values of the principal moments of inertia  $I_{xx}$ ,  $I_{yy}$  and  $I_{zz}$  are used in the model. The velocities along each of the aircraft's axes are given by  $(V_x, V_y, V_z)$  and the rotational velocities about the axes by  $(W_x, W_y, W_z)$ . The weight of the aircraft acting at the centre of gravity (CG) position is denoted  $F_{zW} = mg$ ; it is assumed to act along the  $z$ -axis in the aircraft body coordinate system because the pitch and roll angles remain relatively small throughout this analysis. The steering angle applied to the nose gear, defined in degrees, is denoted  $\delta$ . It is used as a parameter in the bifurcation analysis. The modelling of tyre forces is discussed in Section 3.2.1 and the orthogonal force elements on each of the tyres are denoted  $F_{x*}$ ,  $F_{y*}$  and  $F_{z*}$ , where  $*$  indicates the nose ( $N$ ), main right ( $R$ ) or main left ( $L$ ) landing gear. The modelling of the aerodynamics is discussed in Section 3.2.2. The individual aerodynamic force and moment elements are defined with respect to the aerodynamic centre of the aircraft and are denoted  $(F_{xA}, F_{yA}, F_{zA})$  and  $(M_{xA}, M_{yA}, M_{zA})$ , respectively. The thrust forces are assumed to act parallel to the  $x$ -axis of the aircraft and are denoted  $F_{xTL}$  and  $F_{xTR}$ ; the total thrust force from both of the engines is parameterized as  $T$  which is defined as a percentage of the maximum available thrust.

The states that vary most significantly during the aircraft's motion are the velocity  $V_x$  in the  $x$ -direction, the velocity  $V_y$  in the  $y$ -direction, and the angular velocity  $W_z$  about the  $z$ -axis (yaw velocity); they are calculated from equations (3.1), (3.2) and (3.6), respectively. A reasonable approximation of the aircraft's dynamics is given by these three equations alone. However, to calculate the asymmetric loading on the landing gears dynamically and with a high level of accuracy it is necessary to solve the equations in the other degrees of freedom: the vertical velocity  $V_z$ , angular velocity  $W_x$  about the  $x$ -axis (roll velocity) and angular velocity  $W_y$  about the  $y$ -axis (pitch velocity) given by equations (3.3), (3.4) and (3.5), respectively.

To calculate the position of the aircraft as it moves over the ground plane it is necessary to do so with reference to a fixed location and orientation in space. Therefore, we solve a set of equations describing the position of the aircraft in the world coordinate system with position  $(X, Y, Z)$  and angular orientation given by the Euler angles  $(\psi, \theta, \phi)$ , where  $\psi$  is the yaw angle,  $\theta$  the pitch angle and  $\phi$  the roll angle. The plane given by  $Z = 0$  is the (flat) ground plane. Transformations between the body coordinate system and the world coordinate system can be performed by applying the standard sequence of rotations given in Phillips [41]. Defining the velocities in the world axis as  $V_{xW}$ ,  $V_{yW}$  and  $V_{zW}$ , the velocity transformation equations are given by:

$$\begin{pmatrix} V_{xW} \\ V_{yW} \\ V_{zW} \end{pmatrix} = \begin{bmatrix} C_\theta C_\psi & S_\phi S_\theta C_\psi - C_\phi S_\psi & C_\phi S_\theta C_\psi + S_\phi S_\psi \\ C_\theta S_\psi & S_\phi S_\theta S_\psi + C_\phi C_\psi & C_\phi S_\theta S_\psi - S_\phi C_\psi \\ -S_\theta & S_\phi C_\theta & C_\phi C_\theta \end{bmatrix} \begin{pmatrix} V_x \\ V_y \\ V_z \end{pmatrix}, \quad (3.7)$$

where  $C_* = \cos(*)$  and  $S_* = \sin(*)$  for notational convenience. Defining the angular velocities in the world axis as  $W_{xW}$ ,  $W_{yW}$  and  $W_{zW}$ , the angular velocity transformation equations are given by:

$$\begin{pmatrix} W_{xW} \\ W_{yW} \\ W_{zW} \end{pmatrix} = \begin{bmatrix} 1 & S_\phi S_\theta / C_\theta & C_\phi S_\theta / C_\theta \\ 0 & C_\phi & -S_\phi \\ 0 & S_\phi / C_\theta & C_\phi / C_\theta \end{bmatrix} \begin{pmatrix} W_x \\ W_y \\ W_z \end{pmatrix}. \quad (3.8)$$

**Table 3.1.** System parameters and their values as used in the model.

Symbol	Parameter	Value	
	Dimensions relative to CG position		
$l_{xN}$	$x$ -distance to the nose gear	$(10.186 + CG \div 100 \times l_{mac})$ m	
$l_{zN}$	$z$ -distance to the nose gear	2.932 m	
$l_{xR,L}$	$x$ -distance to the main gears	$(2.498 - CG \div 100 \times l_{mac})$ m	
$l_{yR,L}$	$y$ -distance to the main gears	3.795 m	
$l_{zR,L}$	$z$ -distance to the main gears	2.932 m	
$l_{xA}$	$x$ -distance to the aerodynamic centre	$([0.25 - CG \div 100] \times l_{mac})$ m	
$l_{zA}$	$z$ -distance to the aerodynamic centre	0.988 m	
$l_{xT}$	$x$ -distance to the thrust centre	$([0.25 - CG \div 100] \times l_{mac})$ m	
$l_{yTR,TL}$	$y$ -distance to the thrust centre	5.755 m	
$l_{zT}$	$z$ -distance to the thrust centre	1.229 m	
	Mass	Light case	Heavy case
$m$	Mass of the aircraft	45420 kg	75900 kg
	Tyre parameters		
$k_{zN}$	Stiffness coeff. of the nose tyre	1190 kN/m	
$k_{zM}$	Stiffness coeff. of the main tyre	2777 kN/m	
$c_{zN}$	Damping coeff. of the nose tyre	1000 Ns/m	
$c_{zM}$	Damping coeff. of the main tyre	2886 Ns/m	
$\mu_R$	Rolling resistance coeff.	0.02	
	Aerodynamics parameters		
$l_{mac}$	Mean aerodynamic chord	4.194 m	
$S_w$	Wing surface area	122.4 m <sup>2</sup>	
$\rho$	Density of air	1.225 kg/m <sup>3</sup>	

Therefore the equations for the position of the aircraft are given by:

$$\begin{aligned}
 \dot{X} &= V_{xW}, & \dot{\psi} &= W_{zW}, \\
 \dot{Y} &= V_{yW}, & \dot{\theta} &= W_{yW}, \\
 \dot{Z} &= V_{zW}, & \dot{\phi} &= W_{xW}.
 \end{aligned} \tag{3.9}$$

The position  $(X, Y)$  and orientation  $\psi$  are used to plot trajectories of the aircraft motion. The height  $Z$  above the ground plane and the angles  $\theta$  and  $\phi$  that the aircraft makes with the ground plane are used to calculate the load distribution between landing gears.

### 3.2.1 Tyre modelling

The force elements acting on the tyres are calculated with a tyre model developed by a GARTEUR action group investigating ground dynamics [20]. The fundamental work behind this model can be found in [40]. The GARTEUR tyre model was also implemented in the SIMMECHANICS model, see Section 2.2.1. In order to calculate tyre forces for the mathematical model it is necessary to calculate the local displacements and velocities of the tyres; full details

are given in this section. The focus of this work is primarily stable turning solutions where tyre velocities are not small; the tyre model we use is suitable for this application. To ensure that the tyre model response is always continuous we work under the assumption that as the translation velocities of the tyres goes to 0, so do the lateral and longitudinal tyre forces. There are models that give more reliable results at low velocities [49, 51]; these models are more applicable if the emphasis of the work is on low-velocity operations. Throughout this section a second subscript  $N$ ,  $L$  or  $R$  following  $x$ ,  $y$  or  $z$  indicates that the respective velocity or force is aligned with the local tyre coordinate system; in the case of the nose gear the components  $xN$  and  $yN$  are not aligned with the body-fixed coordinate system (except when  $\delta = 0^\circ$ ). The model used here assumes that the roll axis of the tyre is always parallel to the ground because the pitch and roll angles of the aircraft remain relatively small. It is therefore appropriate to use the velocities of the aircraft in the body coordinate system and Euler angles to calculate local displacements and velocities of the tyres. This section focuses on these calculations that are used in obtaining the tyre forces.

To model the vertical force component on the tyre a linear spring and damper system can be used [6]. For example, the total force acting on the nose gear is:

$$F_{zN} = -k_{zN}\delta_{zN} - c_{zN}V_{zN} \quad (3.10)$$

where  $V_{zN}$  is the vertical velocity of the nose gear tyre, and  $\delta_{zN}$  is the nose gear tyre deflection representing the change in tyre diameter between the loaded and unloaded condition. The stiffness coefficients  $k_{z*}$  and damping coefficient  $c_{z*}$  are specified in Table 3.1. Differences in the vertical velocity and deflection of each tyre give the asymmetric load distribution between the gears. The vertical velocity of each tyre can be calculated in terms of the velocities in the body coordinate system as:

$$\begin{aligned} V_{zN} &= V_z - l_{xN}W_y, \\ V_{zR} &= V_z + l_{yR}W_x + l_{xR}W_y, \\ V_{zL} &= V_z - l_{yL}W_x + l_{xL}W_y, \end{aligned} \quad (3.11)$$

where  $V_{z*}$  is the local vertical velocity of the respective tyre. Due to the assumptions that the roll axes of the tyres remain parallel to the ground and that the pitch and roll angles of the aircraft remain small, the deflection of each tyre is given in terms of the aircraft's position states in the world coordinate system as:

$$\begin{aligned} \delta_{zN} &= -l_{zN} - Z + l_{xN}\theta, \\ \delta_{zR} &= -l_{zR} - Z - l_{xR}\theta - l_{yR}\phi, \\ \delta_{zL} &= -l_{zL} - Z - l_{xL}\theta + l_{yL}\phi. \end{aligned} \quad (3.12)$$

The longitudinal and lateral forces at the tyre-ground interface depend on the vertical load acting on the tyre and on its slip angle. The slip angle of a tyre is the angle the tyre makes with its direction of motion. For each respective tyre, the slip angle  $\alpha_*$  is defined in terms of its local longitudinal velocity  $V_{x*}$  and its local lateral velocity  $V_{y*}$  as:

$$\alpha_* = \arctan\left(\frac{V_{y*}}{V_{x*}}\right). \quad (3.13)$$

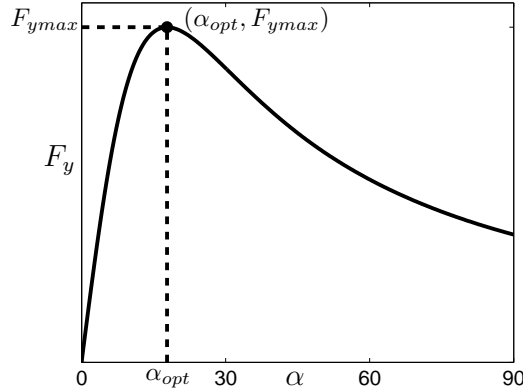


**Figure 3.2.** Lateral force  $F_y$  plotted against slip angle  $\alpha$  as calculated from Equation (3.16). The maximum point  $F_{ymax}$  that can be generated by the tyre occurs at the ‘optimal’ slip angle  $\alpha_{opt}$ .

Therefore, to find the slip angle it is necessary to find the longitudinal and lateral velocity of each tyre. These velocities are calculated in terms of the aircraft’s velocities in the body coordinate system and the steering angle applied to the nose gear  $\delta$  as:

$$\begin{aligned}
 V_{xN} &= V_x \cos(\delta) + (V_y + l_{xN}W_z) \sin(\delta), \\
 V_{yN} &= (V_y + l_{xN}W_z) \cos(\delta) - V_x \sin(\delta), \\
 V_{xR} &= V_x - l_{yR}W_z, \\
 V_{yR} &= V_y - l_{xR}W_z, \\
 V_{xL} &= V_x + l_{yL}W_z, \\
 V_{yL} &= V_y - l_{xL}W_z.
 \end{aligned} \tag{3.14}$$

Note that the rotational velocities  $W_x$  and  $W_y$  are considered to be sufficiently small with respect to  $W_z$  that they can be ignored here.

Longitudinal forces on the tyres are due to the rolling resistance force caused by hysteresis in the rubber of the tyre. The pressure in the leading half of the contact patch is higher than in the trailing half, and consequently the resultant vertical force does not act through the middle of the wheel. A horizontal force in the opposite direction of the wheel movement is needed to maintain an equilibrium. This horizontal force is known as the rolling resistance [57]. The ratio of the rolling resistance  $F_x$ , to vertical load  $F_z$ , on the tyre is known as the coefficient of rolling resistance  $\mu_R$  as given in Table 3.1 [37]. Therefore, the rolling resistance force on the respective tyre  $F_{x*}$  is given by

$$F_{x*} = -\mu_R F_{z*} \cos(\alpha_*), \tag{3.15}$$

which incorporates a cosine function to capture two key features. Firstly, the longitudinal force drops off to zero when the tyre is moving sideways ( $\alpha_* = \pm 90^\circ$ ) and secondly, there is a sign change when the direction of motion changes ( $|\alpha_*| > 90^\circ$ ). This adaptation to the longitudinal tyre force model in Section 2.2.1 ensures that the forces are well defined for slip angles close to  $\alpha_* = \pm 90^\circ$ .

When no lateral force is applied to a tyre, the wheel moves in the same direction as the

wheel plane. When a side force is applied, the tyre generates a slip angle  $\alpha_*$  as defined in Equation (3.13). For small slip angles ( $\alpha_* < 5^\circ$ ) the tyre force increases linearly after which there is a nonlinear relationship [57]. The lateral force on the respective tyre  $F_{y*}$  is a function of  $\alpha_*$  and can be represented as:

$$F_{y*}(\alpha_*) = 2 \frac{F_{y_{max}*} \alpha_{opt*} \alpha_*}{\alpha_{opt*}^2 + \alpha_*^2}, \quad (3.16)$$

where  $F_{y_{max}*}$  is the maximum force that the tyre can generate and  $\alpha_{opt*}$  is the ‘optimal’ slip angle at which this occurs. The parameters  $F_{y_{max}*}$  and  $\alpha_{opt*}$  depend quadratically on the vertical force on the tyre  $F_{z*}$  and, hence, change dynamically in the model. The values for nose gear tyres  $F_{y_{max}N}$  and  $\alpha_{optN}$ , and main gear tyres  $F_{y_{max}R,L}$  and  $\alpha_{optR,L}$  are obtained from the equations:

$$\begin{aligned} F_{y_{max}N} &= -3.53 \times 10^{-6} F_{zN}^2 + 8.83 \times 10^{-1} F_{zN}, \\ \alpha_{optN} &= 3.52 \times 10^{-9} F_{zN}^2 + 2.80 \times 10^{-5} F_{zN} + 13.8, \\ F_{y_{max}R,L} &= -7.39 \times 10^{-7} F_{zR,L}^2 + 5.11 \times 10^{-1} F_{zR,L}, \\ \alpha_{optR,L} &= 1.34 \times 10^{-10} F_{zR,L}^2 + 1.06 \times 10^{-5} F_{zR,L} + 6.72. \end{aligned} \quad (3.17)$$

For values of  $\alpha_*$  outside the quadrant of  $\alpha_* \in (0^\circ, 90^\circ)$ , the curve in Figure 3.2 is reflected appropriately to either represent the tyre rolling backwards or turning in the opposite direction. The extension of Equation (3.16) over the entire range  $\alpha_* \in (-180^\circ, 180^\circ)$  is shown in Figure 2.2(c) of Section 2.2.1.

### 3.2.2 Modelling the aerodynamics

The aerodynamic model presented here is the same as the one described in Section 2.2.3. Aerodynamic effects are nonlinear because the forces are proportional to the square of the velocity of the aircraft. Due to the geometry of the aircraft, the forces also depend nonlinearly on the angle the it makes with the airflow, the sideslip angle  $\beta$  and on the angle of attack  $\sigma$ . We consider ground manoeuvres, with no incident wind. Hence, the sideslip angle  $\beta$  of the entire aircraft is equal to and interchangeable with its slip angle. The slip angle of the aircraft is defined in the same way as that of the tyres, but this time in terms of the velocities of the entire aircraft:  $\alpha_{ac} = \arctan(V_y/V_x)$ . Because we are studying ground manoeuvres, the angle of attack  $\sigma$  remains relatively steady. There are six components to the aerodynamic forces; three translational and three moments. The forces are assumed to act at the aerodynamic centre of the aircraft [14], defined as 25% along the mean aerodynamic chord from its leading edge. The six force elements are given by

$$\begin{aligned} F_{xA} &= \frac{1}{2} \rho |V|^2 S_w C_x(\alpha_{ac}, \sigma), & M_{xA} &= \frac{1}{2} \rho |V|^2 S_w l_{mac} C_l(\alpha_{ac}, \sigma), \\ F_{yA} &= \frac{1}{2} \rho |V|^2 S_w C_y(\alpha_{ac}, \sigma), & M_{yA} &= \frac{1}{2} \rho |V|^2 S_w l_{mac} C_m(\alpha_{ac}, \sigma), \\ F_{zA} &= \frac{1}{2} \rho |V|^2 S_w C_z(\alpha_{ac}, \sigma), & M_{zA} &= \frac{1}{2} \rho |V|^2 S_w l_{mac} C_n(\alpha_{ac}, \sigma), \end{aligned} \quad (3.18)$$

where the parameters  $\rho$ ,  $S_w$  and  $l_{mac}$  are defined in Table 3.1. The dimensionless coefficient functions  $C_*$  depend nonlinearly on  $\alpha_{ac}$  and  $\sigma$  and are based on wind-tunnel data and results from computational fluid dynamics. The coefficients used here were obtained from a model developed by the GARTEUR group [20].

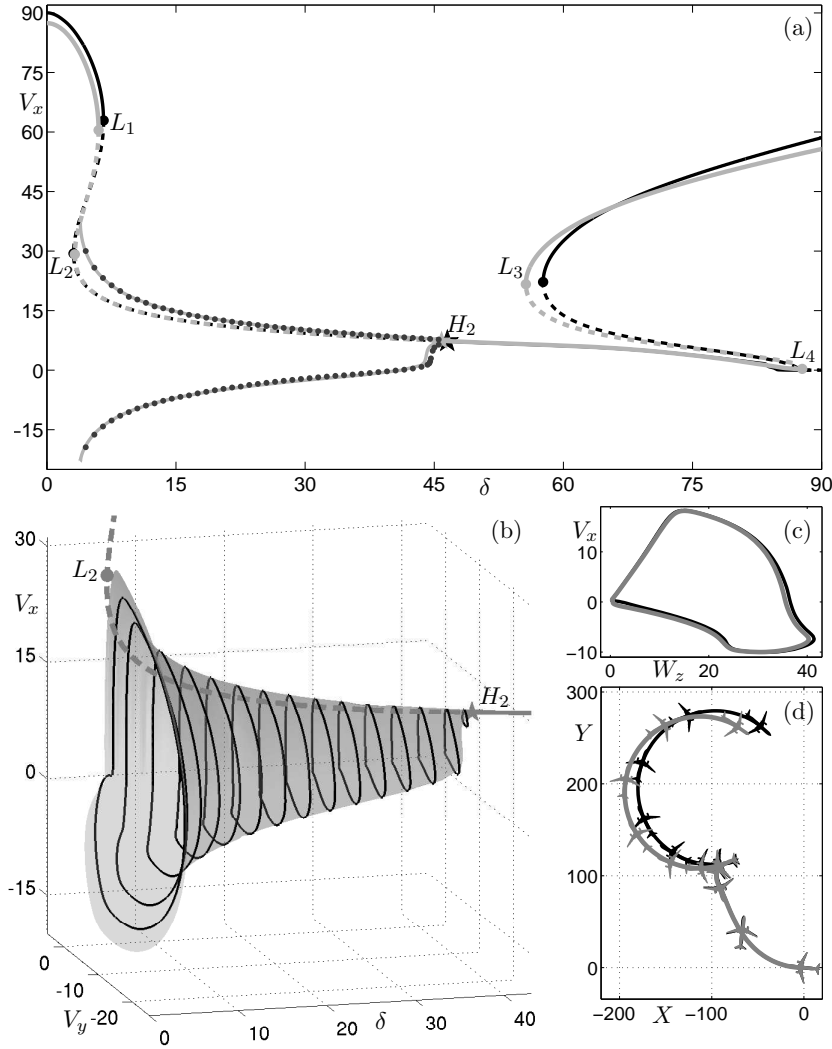


**Figure 3.3.** Comparison between the mathematical model (3.1)–(3.6) (grey curves) and the SIMMECHANICS model (black curves). Panel (a) shows one-parameter bifurcation diagrams for varying steering angle  $\delta$  and fixed  $CG = 14\%$  and  $T = 19\%$ . There is a single branch of turning solutions; stable parts are solid and unstable parts are dashed. Changes in stability occur at the bifurcation points  $L_1$ ,  $L_3$ ,  $L_4$  and  $H_2$ . The maximum and minimum forward velocity of a branch of periodic solutions originating at  $H_2$  are also shown. Panel (b) shows the branch of periodic solutions plotted in the  $(\delta, V_y, V_x)$ -projection; the (grey) surface was computed from the mathematical model and the individual orbits (black closed curves) on the surface were computed with the SIMMECHANICS model. Panel (c) shows a comparison of the individual periodic orbits at  $\delta = 10^\circ$  in the  $(W_z, V_x)$ -projection. The corresponding CG trace of the aircraft in the  $(X, Y)$  ground plane is shown in panel (d) with markers indicating the orientation of the aircraft at regular time intervals. In all figures velocities  $V_x$  and  $V_y$  are measured in m/s, rotational velocity  $W_z$  in deg/s, and distances  $X$  and  $Y$  in m.

### 3.3 Validation of mathematical model

We now present results that were used as part of the validation process for the mathematical model described in Section 3.2 against the established SIMMECHANICS model [42]. Specif-

ically, we show in Figure 3.3 a comparison of a one-parameter bifurcation study of turning solutions as a function of the steering angle  $\delta$ . Throughout Figure 3.3, solutions for the mathematical model (3.1)–(3.6) are in grey and those of the SIMMECHANICS model, as shown previously in Figure 2.6(a), are in black. This comparison shows that there is a high level of agreement between the two models over the entire relevant range of  $\delta$ . Furthermore, a detailed comparison of periodic solutions (corresponding to unstable turning) shows that the two models also agree closely in terms of laterally unstable behaviour.

Figure 3.3(a) shows a direct comparison of a bifurcation diagram in  $\delta$  of turning solutions for  $CG = 14\%$  and  $T = 19\%$ , where the forward velocity of the aircraft  $V_x$  is used as a measure of the solution; the data from the SIMMECHANICS model have been reproduced from Figure 4 in Reference [42]. A single branch of solutions originates in the top left of the diagram and terminates in the top right; stable parts are solid curves and unstable parts are dashed curves. Changes in stability occur at the limit point bifurcations  $L_1, L_3, L_4$  and at the Hopf bifurcation point  $H_2$ . There is a branch of periodic solutions that originates from  $H_2$ ; the maximum and minimum velocities of these solutions are shown as a continuous solid grey curve for the mathematical model (3.1)–(3.6) and as a series of black dots at discrete points for the SIMMECHANICS model. More details of the solutions represented in the bifurcation diagram and the significance of passing the different bifurcations is discussed in greater detail in Chapter 2.

Overall there is close agreement in Figure 3.3(a) between the bifurcation curves of the two models. Any differences are quite small and restricted to certain regions of operation. At the initial point where  $\delta = 0$  the aircraft travels in a straight line. Here the mathematical model has a velocity of  $V_x \approx 87\text{m/s}$ , while the SIMMECHANICS model has a velocity of  $V_x \approx 90\text{m/s}$ . This small difference exists on the branch between the initial point and the bifurcation point  $L_1$  along which the solutions represent large radius turning circles. When the steering angle is increased to a value beyond  $L_1$  the aircraft will attempt to follow a smaller radius turning circle at low velocity. Following the solution branch through  $L_1$ , at which there is a change in stability, we see that the curves computed with the different models agree closely. Along section of the solution branch that is approximately horizontal, which represents small radius turns, the two models remain in almost exact agreement up to the bifurcation  $L_4$ . A branch of periodic solutions originates at the Hopf bifurcation  $H_2$  which is the typical behaviour [50]. The respective maximum and minimum velocities along the branch of periodic solutions show a high level of agreement; these solutions are discussed in further detail below. Due to an update in the way longitudinal tyre forces are handled at high slip angles, the limit point bifurcation  $L_4$  is detected in the mathematical model, but not in the original SIMMECHANICS model. Nevertheless the two models exhibit qualitatively the same behaviour in this region of the bifurcation diagram. For the large radius solutions along the branch between  $L_3$  and the final point in the top right of Figure 3.3(a) the two models show again a slight difference in velocity along the branch. Furthermore, the limit point bifurcation  $L_3$  occurs at a somewhat lower value of  $\delta$  in the mathematical model.

Figure 3.3(b) shows the branch of periodic solutions in the  $(\delta, V_y, V_x)$ -projection, where  $V_y$  is the lateral velocity of the aircraft. In a previous study these solutions were studied in great detail and four types of qualitatively different behaviour were identified [42]. We show this data to demonstrate that the two models agree to a high level of detail even in terms of the laterally unstable motion that the periodic solutions represent. The periodic solutions form

a surface in parameter times phase space. For the mathematical model, it can be computed directly by continuation of the periodic solutions from the Hopf bifurcation point  $H_2$ . For the SIMMECHANICS model, on the other hand, periodic solutions can only be found at discrete values of  $\delta$  by numerical simulation. The two models show excellent agreement: the (black) periodic orbits of the SIMMECHANICS model lie almost exactly on the grey surface of periodic solutions of the mathematical model. Figure 3.3(c) shows a specific periodic orbit in more detail for  $\delta = 10^\circ$  in the  $(V_x, W_z)$ -projection;  $W_z$  is the angular velocity of the aircraft about its vertical axis. The two periodic orbits indeed agree so closely that the (black) periodic orbit of the SIMMECHANICS model is eclipsed by that of the mathematical model. Figure 3.3(d) shows a trace of the aircraft's centre of gravity position over one period of its motion in the  $(X, Y)$  ground plane for each of the two models. Markers drawn to scale on the CG trace show the aircraft's relative direction of motion at equal time intervals along the trajectory. The trajectories computed with the two models agree very closely in the initial section but appear to diverge slightly after a point close to  $(X, Y) = (100, 100)$  where the tangent of the CG trace changes very quickly. In fact, at this point in the trajectory, where the velocity of the aircraft is very low, the plot exaggerates a very small discrepancy in the amount the aircraft rotates. Either side of this point the trajectories agree very precisely.

In summary of the validation process, the models agree very closely both in terms of the turning circle solutions represented in the bifurcation diagram, as well as the lateral unstable periodic solutions. The agreement is well within the accuracy of comparisons with actual test data, so that the mathematical model (3.1)–(3.6) can be used with confidence. In the bifurcation diagram there were only some small observable differences at high velocities. These differences occur because the mathematical model does not include the oleos. As we checked, with the oleos included the aircraft assumes a slightly elevated angle of attack that increases the lift and, therefore, reduces the loads on the tyres. In turn, this reduces the longitudinal and lateral forces on the tyres and, thus, the aircraft travels faster with the oleos included. The slight discrepancy in the amount the aircraft rotates at the point of lowest velocity of the periodic solution is also due to the fact that the oleos are not included in the mathematical model. Namely, with oleos a slight shift of weight from the inner to the outer gears accounts for a greater rotation as exhibited by the SIMMECHANICS model in Figure 3.3(d). In spite of these small discrepancies, the dynamics of the two models are still sufficiently close and qualitatively the same over the entire operating range. Furthermore, the close agreement between the two models justifies that we do not include the oleos as part of Equations (3.1)–(3.6) for the bifurcation study of turning solutions.

### 3.4 Two-parameter bifurcation study and sensitivity analysis

In this section we present two-parameter bifurcation diagrams, where we track turning solutions in dependence on the steering angle  $\delta$  and the centre of gravity position  $CG$ . By choosing to represent turning solutions in terms of their corresponding forward velocity  $V_x$ , we obtain a surface of turning solutions in  $(\delta, V_x, CG)$ -space. From a practical point of view, this surface is assembled from one-parameter continuation runs in  $\delta$ , as presented in Section 3.3, which are computed at discrete values of  $CG$  that cover an appropriate range. Two-parameter continuation with AUTO is used to compute the loci of limit point and Hopf bifurcations directly under the variation of both  $\delta$  and  $CG$ . Combining the results from these two computations into

a single plot is an effective way of representing the turning dynamics and its stability over the complete range of  $\delta$  and  $CG$  in a single figure. What is more, we are able to perform a sensitivity analysis of turning solutions by computing the respective solution surfaces for different fixed values of other parameters. Specifically, we consider different thrust cases for a heavy aircraft in Section 3.4.1, and for a light aircraft in Section 3.4.2. Finally, we show two-dimensional projections of bifurcation curves to highlight certain features that explain qualitative changes in the bifurcation structure when the thrust is changed.

### 3.4.1 Heavy aircraft case

Figure 3.4 shows three surfaces of turning solutions in  $(\delta, V_x, CG)$ -space for the case of a heavy aircraft, each at a different value of the thrust  $T$ . Computed solution branches for fixed discrete values of  $CG$  originate on the left side of the diagram; they are initially stable and may become unstable at bifurcation curves on the surface, namely along the curve  $L$  of limit point bifurcations and the curve  $H$  of Hopf bifurcations. Note that the typical operating range for the centre of gravity position is  $CG \in (10\%, 40\%)$ . Nevertheless, it is convenient to show an extended  $CG$ -range to demonstrate completeness of the overall bifurcation structure. To aid in the visualisation of the key bifurcations at small steering angles one-parameter bifurcation diagrams at fixed  $CG$  are shown in Figure 3.5 for the three different thrust cases. Specifically,  $CG$  is fixed at 30% and  $\delta$  is varied as the continuation parameter over the range  $\delta \in (0^\circ, 10^\circ)$ . The branches are plotted as dashed curves and labelled  $CG_{30}$  in Figure 3.4; their intersections with the bifurcation curves  $L$  and  $H$  correspond to bifurcation points.

In Figure 3.4(a), for a thrust of  $T = 16\%$  of maximal thrust, we can see that for a forward CG position of  $CG < 20\%$  the solutions are uniformly stable. At  $\delta = 0^\circ$  the aircraft travels in a straight line with  $V_x \approx 68\text{m/s}$ ; this initial velocity remains constant under variation of  $CG$ . As  $\delta$  is increased, the velocity of the stable solutions decreases rapidly before starting to plateau out at  $\delta \approx 7.5^\circ$ ; the velocity of solutions continues to decrease gradually down to  $0\text{m/s}$  as  $\delta$  is increased towards  $90^\circ$ . Therefore, for  $CG < 20\%$  and with increasing  $\delta$ , there is a continuous and stable transition from stable large radius solutions via stable small radius solutions all the way to a stationary solution where the nose gear is perpendicular to the direction of motion. For fixed  $CG \in (20\%, 50\%)$  the individual solution branches intersect the curve of limit point bifurcations  $L$  at two bifurcation points. The minimal point on  $L$  at  $CG \approx 20\%$  is a cusp point [29]. When traversing the surface from left to right (fixing  $CG$  but varying  $\delta$ ) there are fold points in the solution branches that occur at intersections with  $L$ . Figure 3.5(a) shows the solution branch  $CG_{30}$  for the case  $T = 16\%$ . In this one-parameter continuation the bifurcation points  $L_1$  and  $L_2$  correspond to intersections on the surface with the curve of limit point bifurcations  $L$ . When the limit point bifurcation curve  $L$  is crossed at the left fold in Figure 3.4(a) (corresponding to  $L_1$  in Figure 3.5(a)) the large-radius turning solution becomes unstable and, the aircraft spirals towards and then follows a stable small-radius solution. Similarly, when  $L$  is crossed at the right fold in Figure 3.4(a) (corresponding to  $L_2$  in Figure 3.5(a)) the small-radius solution becomes unstable and the aircraft spirals out to and settles down onto a stable large-radius solution. Therefore, as is typical in systems with several limit point bifurcations, there is a hysteresis loop [19] between large- and small-radius turns. A similar hysteresis loop exists between large-radius and small-radius solutions under the variation of  $CG$  at fixed values of  $\delta > 5^\circ$ . At large values of  $\delta$  and  $CG$  the solutions that can

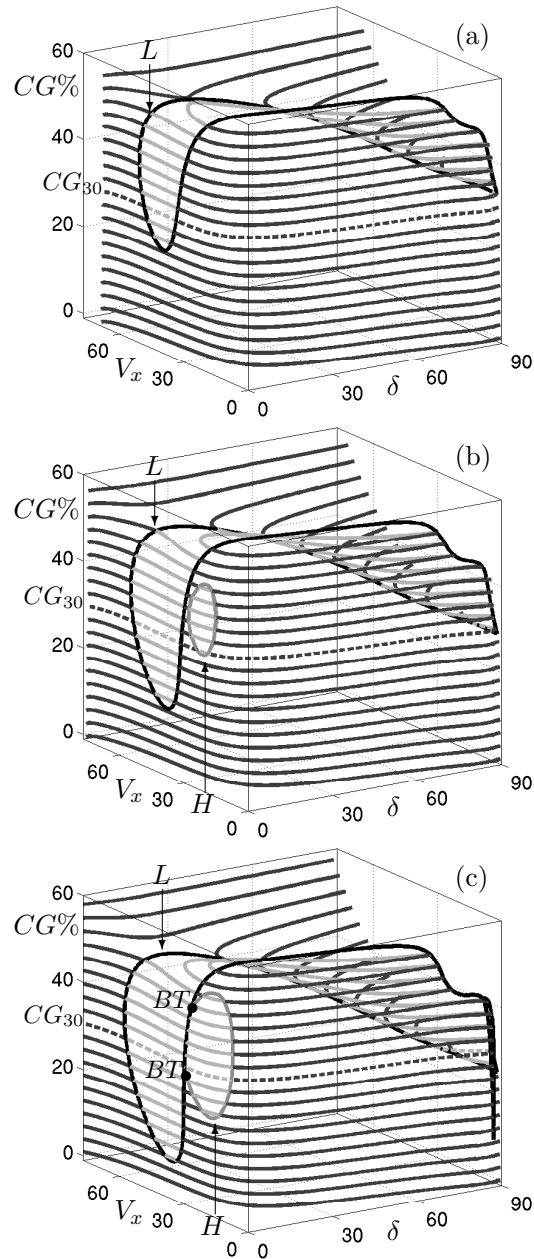


**Figure 3.4.** Surfaces of turning solutions in  $(\delta, V_x, CG)$ -space for a heavy aircraft (as specified in Table 3.1) and for three fixed values of the thrust;  $T = 16\%$  in panel (a),  $T = 18\%$  in panel (b), and  $T = 20\%$  in panel (c). Stable solutions are black and unstable solutions are grey; limit point bifurcations occur along the thick black curve  $L$  and Hopf bifurcations occur along the thick grey curve  $H$ ; the black dots in panel (c) are Bogdanov-Takens bifurcation points labelled  $BT$ . The specific cases plotted in Figure 3.5 are shown as dashed curves and labelled  $CG_{30}$  in each panel.

be seen in the background of the Figure 3.4(a) represent large-radius turns for which the nose gear does not generate enough force to keep the aircraft stationary and is, hence, effectively

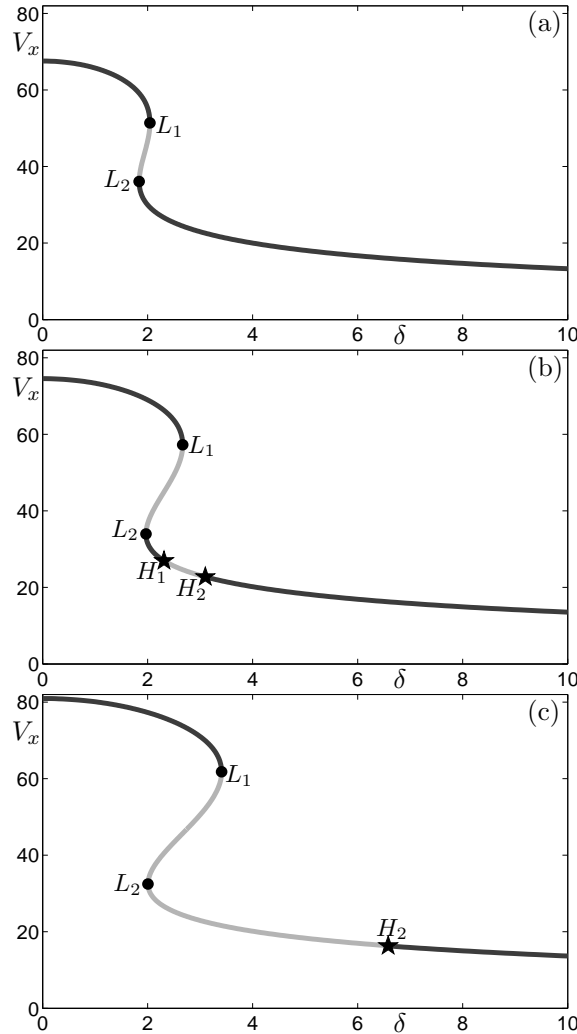


**Figure 3.5.** One-parameter bifurcation curves at fixed  $CG = 30\%$  for varying  $\delta \in (0^\circ, 10^\circ)$  plotted against  $V_x$  for  $T = 16\%$  in panel (a),  $T = 18\%$  in panel (b), and  $T = 20\%$  in panel (c). Stable solutions are black and unstable solutions are grey. Limit point bifurcations  $L_1$  and  $L_2$  are marked with solid dots and Hopf bifurcations  $H_1$  and  $H_2$  with stars.

dragged along the ground. For sufficiently large values of  $CG > 55\%$  the solution branches become uniformly stable, and they represent large-radius turns only.

When the thrust level  $T$  is increased, many of the features of the surface described above persist, but there are some changes. Figure 3.4(b) shows the surface for  $T = 18\%$ . Here the forward velocity when  $\delta = 0^\circ$  has increased to  $V_x \approx 74\text{m/s}$ . Another change is that the  $CG$ -level at which the solution branches first intersect  $L$  has decreased to  $CG \approx 12\%$ . However, the most significant difference is a qualitative change in the dynamics: a closed curve of Hopf bifurcations now bounds a new region of unstable turning solutions on the surface. This new region exists for small  $\delta$  and  $CG \in (29\%, 46\%)$ . Figure 3.5(b) shows the solution branch  $CG_{30}$  for the case  $T = 18\%$ . The two limit point bifurcations  $L_1$  and  $L_2$  persist from the lower thrust case but have moved further apart both in terms of  $\delta$  and  $V_x$ . There are two new bifurcations  $H_1$

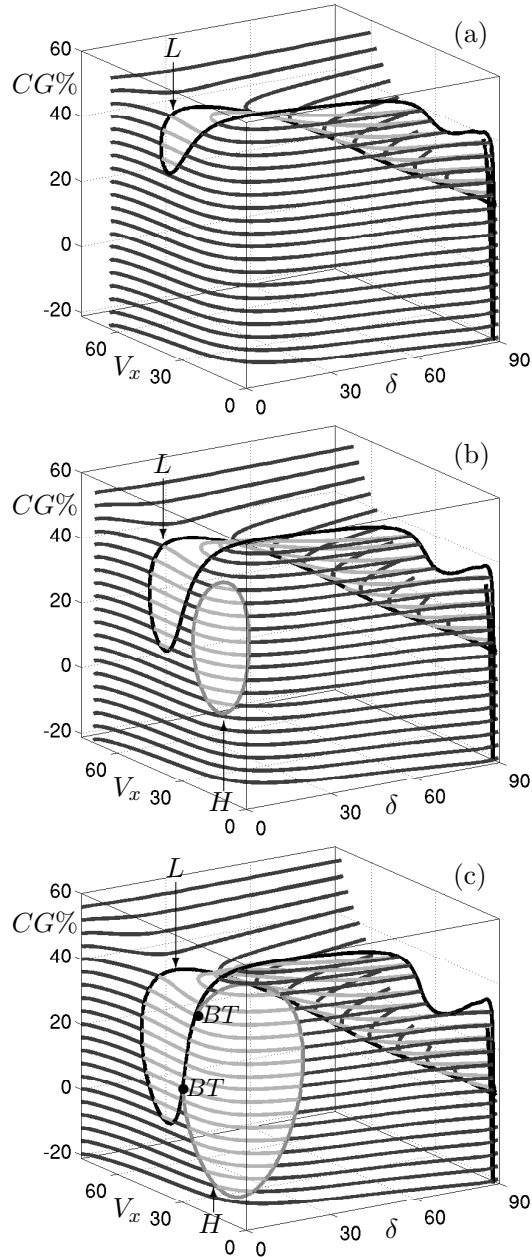
and  $H_2$  that correspond to intersections on the surface with the curve  $H$  of Hopf bifurcations. Crossing  $H$  into this region represents a change where the aircraft will attempt to follow a turning circle solution that is unstable and, therefore, it loses lateral stability. An example of this type of solution was given in Figure 3.3(c) and (d); an extensive account of qualitatively different types of laterally unstable solution can be found in Reference [42]. Note further that crossing  $L$  at the left fold may now lead to the aircraft moving from a stable large-radius turn to laterally unstable behaviour. However, for  $CG < 29\%$  this bifurcation along  $L$  does not lead to a loss of lateral stability.

Figure 3.4(c) shows that there is a further qualitative change when the thrust is increased to  $T = 20\%$ . Namely, the regions bounded by the curves  $L$  and  $H$  have increased in size: the minimum point on  $L$  occurs now at  $CG \approx 5\%$ , and  $H$  exists over the range  $CG \in (20\%, 49\%)$ . As a consequence, the regions bounded by the curves  $L$  and  $H$  have increased in size so much that the curve  $H$  is no longer closed but terminates at two intersection points with the curve  $L$ . Mathematically, these intersection are known as Bogdanov-Takens bifurcation points [29] and labelled  $BT$ . Figure 3.5(c) shows the solution branch  $CG_{30}$  for the case  $T = 20\%$ . In this high-thrust case the limit point bifurcations  $L_1$  and  $L_2$  persist and are further separated. The Hopf bifurcation  $H_1$  is no longer encountered above the lower point  $BT$  in Figure 3.4(c) while  $H_2$  persists and has moved to a larger value of  $\delta$ . Further details of the topological change associated with the emergence of Bogdanov-Takens bifurcation points are given in Section 3.4.3. Another change is that the value of  $CG$  above which the dynamics are uniformly stable is now reduced, from  $CG \approx 55\%$  in Figure 3.4(a) to  $CG \approx 50\%$  in Figure 3.4(c).

The properties of the solution surfaces in Figure 3.4 have physical interpretations in terms of the dynamics of the aircraft. When  $CG$  is increased (the CG position is moved aft) the load on the nose gear is reduced and, thus, the turning force that it can generate is reduced. When making high-velocity turns the aerodynamic forces have a greater effect. In fact, at sufficiently high speeds the holding force generated by the tailplane, which attempts to keep the aircraft travelling in a straight line, becomes more dominant than the turning force generated by the nose gear. This explains why in each panel of Figure 3.4, for a greater value of  $CG$ , the left fold of  $L$  moves to a larger value of  $\delta$  because a greater steering angle is required to generate the necessary turning moment to overcome the aerodynamic holding force. Similarly, the right fold along  $L$  is associated with the effect that a decreasing turning moment from the nose gear (as  $\delta$  is decreased) is being overcome by the aerodynamic forces. Overall, the region bounded by  $L$  grows with thrust because at higher velocities the aerodynamic forces are increased. The region bounded by  $H$  appears and grows with increasing thrust level because the aircraft attempts to make higher velocity turns to the point where they become laterally unstable.

### 3.4.2 Light aircraft case

Figure 3.6 shows surfaces of turning solutions for the case of a light aircraft for three fixed values of the thrust. They are represented in the same way as for the heavy case, except that the range of  $CG$  has been extended to  $CG \in (-20\%, 60\%)$ . The first result is that the turning behaviour for both loading cases is qualitatively the same in the respective panels for low, medium and high thrust; compare with Figure 3.4. Nevertheless, there are some quantitative differences that are of importance from the operational point of view. First of all, notice that the thrust levels identified for the light aircraft case are 4% less throughout compared with the



**Figure 3.6.** Surfaces of turning solutions in  $(\delta, V_x, CG)$ -space for a light aircraft (as specified in Table 3.1) and for three fixed values of the thrust;  $T = 12\%$  in panel (a),  $T = 14\%$  in panel (b), and  $T = 16\%$  in panel (c). Stable solutions are black and unstable solutions are grey; limit point bifurcations occur along the thick black curve  $L$  and Hopf bifurcations occur along the thick grey curve  $H$ ; the black dots in panel (c) are Bogdanov-Takens bifurcation points labelled  $BT$ .

heavy case. More specifically, for a value of thrust of  $T = 12\%$ , as shown in Figure 3.6(a), the initial velocity at  $\delta = 0^\circ$  on the individual solution branches is  $V_x \approx 63\text{m/s}$ . Furthermore, the region bounded by the curve  $L$  for small  $\delta$  does not extend as far into the operational range of  $CG$  as for the heavy aircraft case; compare with Figure 3.4(a). When the thrust is increased

by 2% we again find a region of laterally unstable behaviour, bounded by a closed curve of Hopf bifurcations  $H$ ; see Figure 3.6(b). However, the size of the instability region bounded by  $H$  is dramatically larger when compared to the corresponding heavy aircraft case in Figure 3.4(b). Namely, the minimal point on  $L$  has moved to  $CG \approx 15\%$  and the region bounded by  $H$  extends over the range  $CG \in (1\%, 42\%)$ , below the minimal point on  $L$ . Therefore, in contrast to the heavy case, passing the bifurcation on the left fold along  $L$  always results in the aircraft settling onto laterally unstable behaviour. Furthermore, the region of laterally unstable behaviour in Figure 3.4(b) is accessible from the left without passing a limit point bifurcation. This means that the region of laterally unstable behaviour could be approached more suddenly at lower velocities. When the thrust is increased further to  $T = 16\%$ , as is shown in Figure 3.6(c), the regions bounded by  $L$  and  $H$  increase further and we again find that  $H$  ends at two Bogdanov-Takens bifurcation points on  $L$ . Furthermore, the minimal point on  $L$  moves to a negative value of  $CG \approx -1\%$  and the range of  $H$  extends to  $CG \in (-18\%, 48\%)$ . Note that a negative value of  $CG$  represents a CG position in front of the leading edge of the mean aerodynamic chord.

Overall, we find in the light aircraft case that the size of the region of laterally unstable behaviour increases much more dramatically when compared with the heavy aircraft case. This is a quantitative observation that is of relevance in spite of the fact that the respective panels for the two loading cases are qualitatively the same. Note however that a higher thrust level (of an extra 4% of maximal thrust) is required in the heavy case to achieve similar velocities to the light case. As a result of this the aircraft is much more susceptible to a loss of lateral stability in the light case, as is represented by substantially larger regions of laterally unstable turning solutions.

### 3.4.3 Qualitative changes of the surfaces of solutions with thrust

In Section 3.4.1 and Section 3.4.2 it was demonstrated that the aircraft shows considerable sensitivity to the thrust level: qualitative changes in the overall solution surface occur within a range of 2% of maximum thrust. We now discuss these qualitative changes in more detail. While the nature of the transitions is the same for both loading cases, we consider here the case of a light aircraft as presented in Figure 3.6 because it was seen to be more susceptible to a loss of lateral stability when the thrust is increased.

First of all, the qualitative change between panels (a) and (b) of Figure 3.6 is due to the fact that a closed curve, or isola,  $H$  of Hopf bifurcations appears at a specific thrust value in the interval  $T \in (12\%, 14\%)$ . Indeed, when the thrust is decreased from  $T = 14\%$  then the isola shrinks to a point and disappears. This type of qualitative change of the curve  $H$  is due to a smooth transition through a minimum in the associated two-dimensional surface of Hopf bifurcations in  $(\delta, CG, T)$ -space. This happens at a single value of  $T$  in this three-dimensional parameter space, which is why this is referred to as being of codimension three.

The transition between panels (b) and (c) of Figure 3.6, on the other hand, is more complicated. As Figure 3.7 shows by means of projections of the bifurcation curves  $L$  and  $H$ , it involves the introduction of two Bogdanov-Takens bifurcation points. The mechanism behind this qualitative change is the passage through a codimension-three degenerate Bogdanov-Takens bifurcation, which occurs at an isolated point in  $(\delta, CG, T)$ -space. Figure 3.7 shows all

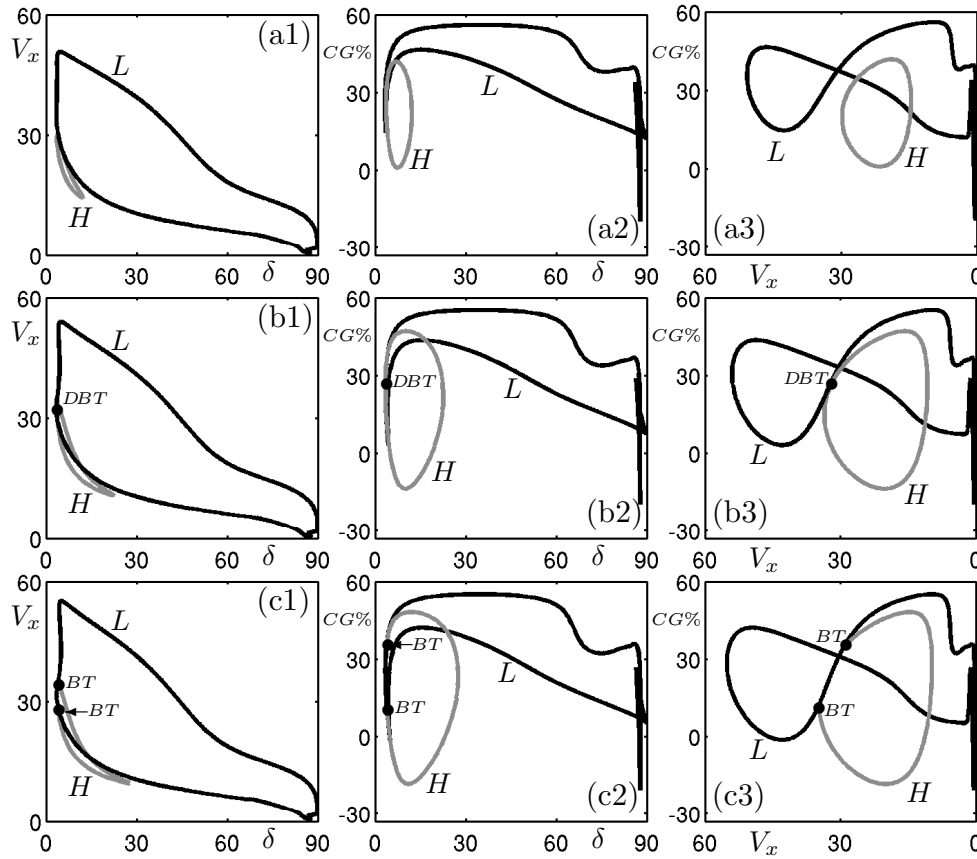


**Figure 3.7.** The bifurcation curves  $L$  and  $H$  for a light aircraft and for thrust levels of  $T = 14\%$  in panels (a),  $T = 15.4\%$  in panels (b), and  $T = 16\%$  in panels (c) are shown in projection onto the  $(\delta, V_x)$ -plane (first column), onto the  $(\delta, CG)$ -plane (second column), and onto the  $(V_x, CG)$ -plane (third column). Note that the  $V_x$ -axis has been reversed in the third column to remain consistent with the surfaces as plotted in Figure 3.6. The black dots in panels (b) represent degenerate Bogdanov-Takens points and in panels (c) two non-degenerate Bogdanov-Takens points. Compare panels (a) and (c) with Figure 3.6(b) and (c), respectively.

three two-dimensional projections of the bifurcation curves from the three-dimensional plots in Figure 3.6 (b) and (c) and for the intermediate transitional case at  $T = 15.4\%$ . The  $(\delta, CG)$ -plane represents the bifurcation diagram in the two parameters, and the same data plotted in the  $(\delta, V_x)$ -plane and  $(V_x, CG)$ -plane reveals the relative positions of the bifurcation curves in terms of the forward velocity  $V_x$ . Due to the way the solution surface is located in  $(\delta, V_x, CG)$ -space, the transition is actually seen most clearly in the third column of Figure 3.7, which shows the projection onto the  $(V_x, CG)$ -plane. Before the degenerate Bogdanov-Takens bifurcation in Figure 3.7(a) the curve  $H$  is indeed closed. At the moment of transition in Figure 3.7(b) the curve  $H$  is still closed, but it now touches the limit point bifurcation curve  $L$  at a single point of tangency. At this point there is a degenerate Bogdanov-Takens bifurcation, labelled  $DBT$ . Mathematically, this point is characterised by a double zero eigenvalue of the linearisation around the respective solution with an additional degeneracy of the higher-order terms of the

normal form [29]. After the transition the degenerate Bogdanov-Takens bifurcation point splits up into two non-degenerate Bogdanov-Takens bifurcation points, which are labelled  $BT$  in Figure 3.7(c). These points are of codimension-two, which means that they are isolated points in the two-dimensional  $(\delta, CG)$ -plane. As a result, the curve  $H$  is no longer closed but now ends at the curve  $L$  at the two  $BT$  points. We do not investigate additional bifurcation curves that are known to exist near these  $BT$  points; however, this could be the subject of future work.

Apart from the nature of transitions between qualitatively different bifurcation diagrams of  $L$  and  $H$  on the solution surface, the projections shown in Figure 3.7 also reveal quantitative features that are not so evident from the surfaces shown in Figure 3.6. For example, panels (a1), (b1), and (c1) of Figure 3.7 show that there is a region to the left of the bifurcation curves, for  $\delta < 3.5^\circ$ , where no bifurcations occur. This stable region is independent of both the  $CG$  position and the thrust level, so that it might be used to define an upper bound for steering angles used during high velocity turns. A similar bound exists in the heavy case but at a lower value of only  $\delta \approx 1.5^\circ$ .

### 3.5 The effect of reducing tyre friction coefficient

In this section we introduce the variation of a new parameter  $\hat{\mu}$  which represents the percentage reduction in friction at the tyre-ground interface. At  $\hat{\mu} = 0\%$  the taxiway surface conditions are considered to be normal/dry and when  $\hat{\mu}$  is increased the lateral force that can be generated by the tyres reduces. A value of  $\hat{\mu} = 50\%$  is considered to represent a wet taxiway and the force that the tyres can generate reduces to 0 at  $\hat{\mu} = 100\%$ . The result of continuation runs computed in  $\delta$  for discrete values of  $\hat{\mu}$  are represented as a surface of solutions. The surface describes the aircraft's dynamics over the entire range of  $\delta$  and  $\hat{\mu}$  as represented by  $V_x$ . The curves of bifurcations are computed continuously under the variation of both  $\delta$  and  $\hat{\mu}$ ; two-dimensional projections of bifurcation curves show certain features more clearly. In the analysis, we consider a light aircraft with  $CG = 14\%$  and the thrust from the engines fixed at  $T = 13\%$ . Note that the thrust level used here is close to the parameter region identified in Chapter 2 for which laterally unstable behaviour is found.

Figure 3.8(a) shows the resulting surface plot of solutions in  $(\delta, V_x, \hat{\mu})$ -space. Changes in stability occur along the curve  $L$  of limit point bifurcations and the curve  $H$  of Hopf bifurcations. The dynamics are best understood by direct comparison with the surface of solutions shown in Figure 2.7(a) in Section 2.3.3. The surfaces of solutions, plotted in terms of  $\hat{\mu}$  and  $\%T_{max}$ , agree qualitatively and crossing the curves  $L$  or  $H$  in either case corresponds to the same outcome in terms of the dynamics. For very small values of  $\hat{\mu} < 5\%$  there is a region of uniformly stable behaviour. For  $\hat{\mu} > 5\%$  there is a region of laterally unstable behaviour accessible by crossing the curve  $H$ . This laterally unstable region can be reached via a limit point bifurcation for  $\hat{\mu} > 15\%$ . For large values of  $\hat{\mu} > 40\%$  the stable region to the left of  $L$  increases and for  $\hat{\mu} > 60\%$  the dynamics become uniformly stable. This large reduction in the friction coefficient results in the aerodynamic forces becoming the dominant effect for the dynamics. Figure 3.8(b) and 3.8(c) show two-dimensional projections of the bifurcation curves onto the  $(\delta, \hat{\mu})$ -plane and the  $(V_x, \hat{\mu})$ -plane, respectively. The  $(\delta, \hat{\mu})$ -plane represents the bifurcation diagram in the two parameters while the same data plotted in the  $(V_x, \hat{\mu})$ -plane reveals the relative positions of the bifurcation curves in terms of the forward velocity  $V_x$ . When

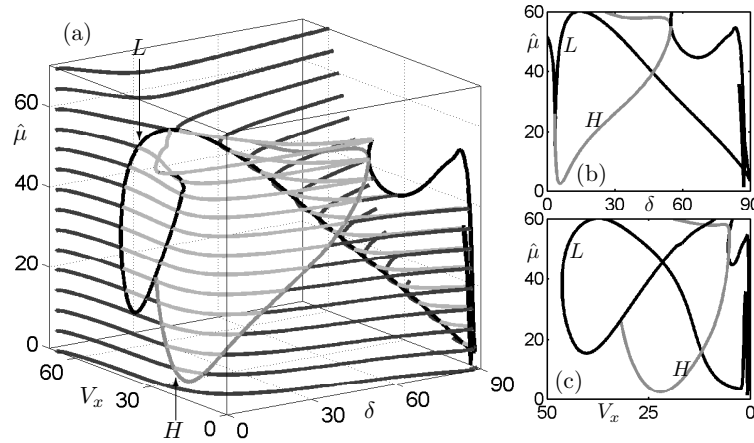


**Figure 3.8.** Panel (a) shows a surface plot of solutions in  $(\delta, V_x, \hat{\mu})$ -space; stable solutions are black and unstable solutions are grey. The curve of limit point bifurcations  $L$  is the thick black curve and the curve of Hopf bifurcations  $H$  is the thick grey curve. Panels (b) and (c) show two-dimensional projections of the bifurcation curves onto the  $(\delta, \hat{\mu})$ -plane and  $(V_x, \hat{\mu})$ -plane, respectively.

$\hat{\mu} = 0$  the solutions are uniformly stable under variation of  $\delta$ . As  $\hat{\mu}$  is increased the solution branches intersect the bifurcation curves  $L$  and  $H$ . By taking parameter values that lie below these two curves the laterally unstable behaviour can be avoided. The curve  $H$  can provide a guide for maintaining stable manoeuvres at higher steering angles. Furthermore, there is a region to the left of  $L$  and  $H$  with  $\delta < 3.5^\circ$  and  $\hat{\mu} < 40\%$  for which no unstable behaviour can occur. Therefore, a value of  $\delta = 3.5^\circ$  can provide an upper bound on the steering angle used in high-velocity turns. The same bound on  $\delta$  was identified in studies that vary the thrust and CG position.

### 3.6 Periodic orbits as canard cycles

The aim in this section is to explain the sharp increase in amplitude of the periodic orbits close to a Hopf bifurcation as reported in Chapter 2. Specifically, in Figure 2.5 from Section 2.3, an apparently discontinuous jump in the amplitude of the periodic oscillations was found close to the two Hopf bifurcations  $H_1$  and  $H_2$ . Due to difficulties in computing families of periodic orbits as a continuous object with the SIMMECHANICS model, time history simulations were used to compute individual periodic orbits at discrete values of  $\delta$ . On the other hand, with the mathematical model it was straightforward to compute the branches of periodic solutions with continuation. This was done in Section 3.3 as part of the model validation process.

In our system (3.1)–(3.6), passing a Hopf bifurcation results in the inner main landing gear tyres saturating and starting to skid; close to the bifurcation the outer gear is able to compensate, and there are small amplitude oscillations about the unstable turning circle solution. Further variation of the steering angle beyond the bifurcation results in the oscillations gradually increasing until the force generated by the outer gear tyres also saturates. The result is a very sharp increase in the amplitude of the oscillations where the aircraft oversteers excessively

before losing control and entering a spin as described in Section 2.4. Although a physical explanation was given for the rapid increase in the amplitude of the oscillations, the phenomena could not be explained from a theoretical point of view. We now use a combination of continuation computations and time history simulations to provide a theoretical explanation for the sharp increase in the size of oscillations. The case considered in this section is that of a light aircraft with  $CG = 35\%$  and  $T = 14\%$ .

A sharp increase in the amplitude of periodic solutions close to a Hopf point is associated with canard cycles in many systems from a range of applications, including chemical reactions, combustion and electronics [4]. In Reference [7] a sharp increase in amplitude of such cycles over an extremely small parameter interval is termed a canard explosion. Systems exhibiting this phenomenon have the property of separable time-scales. An analytical approach is typically used to study the subsystems that describe the dynamics on slow and fast time scales. Due to the complexity of the equations under consideration it is not practical to study the system analytically. However, a numerical approach proves successful in identifying properties of the system that are characteristic of separable time-scales and canard-type oscillations.

Figure 3.9(a) shows a one-parameter bifurcation diagram computed with the continuation package AUTO. The diagram consists of a single branch of steady-state solutions. The continuation parameter is the steering angle  $\delta$ , and the longitudinal velocity of the aircraft  $V_x$  is used as a measure of the solutions. At the right of the figure the branch is stable. As  $\delta$  is decreased the branch becomes unstable in a Hopf bifurcation  $H_2$  giving rise to a stable branch of periodic solutions. Close to the bifurcation the growth of the periodic solutions with decreasing  $\delta$  is typical; that is, it has a square-root type progression. However, decreasing  $\delta$  further,

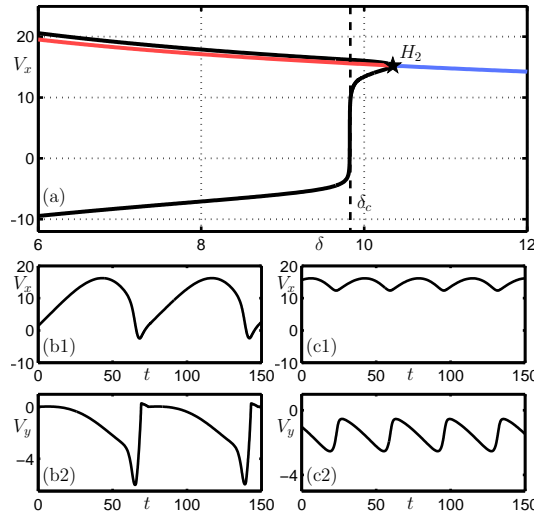


**Figure 3.9.** Panel (a) shows a single branch of steady-state solutions when varying the parameter  $\delta$  and plotted against  $V_x$ ; the stable section is blue and the unstable section is red. The change in stability occurs at a Hopf point  $H_2$  from which a branch of periodic solutions emerges; the maximal and minimal values of  $V_x$  along the branch are black. A sharp increase in the size of the oscillations occurs at  $\delta_c$  which is indicated by a dashed vertical line. Time histories of  $V_x$  and  $V_y$  are plotted at values of  $\delta$  close to  $\delta_c$ . Panels (b1) and (b2) are plotted for  $\delta < \delta_c$ , and panels (c1) and (c2) are plotted for  $\delta > \delta_c$ .

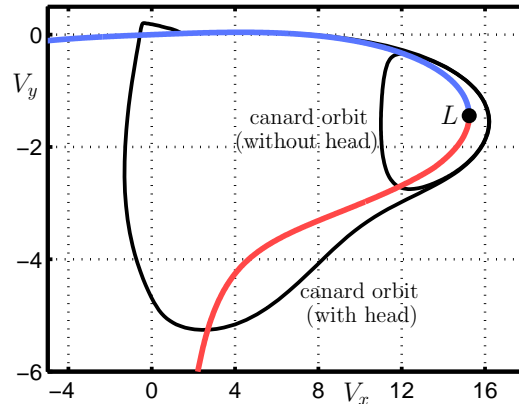


**Figure 3.10.** A branch of steady-state solutions for the frozen system treating  $V_x$  as a parameter is plotted against  $V_y$ ; the stable section is blue and the unstable section is red. The change in stability occurs at a limit point  $L$ . Phase portraits are plotted in black for  $\delta > \delta_c$  (small) and  $\delta < \delta_c$  (large).

the growth rapidly becomes steeper and at  $\delta_c \approx 9.83^\circ$  the lower extent of the branch increases quasi-vertically. As  $\delta$  passes through  $\delta_c$ , the amplitude of the oscillations changes dramatically; the overall amplitude in  $V_x$  increases by a factor of four. Figures 3.9 (c1) and (c2) show time histories of  $V_x$  and the lateral velocity  $V_y$  at  $\delta = 9.89^\circ$ , respectively. This value of  $\delta$  is just before the sharp increase in the size of the oscillations, and the period is approximately 40s. Panels (b1) and (b2) show similar time histories at  $\delta = 9.81^\circ$  after the increase in size of the oscillations, for which the period has grown to approximately 75s. The dramatic increase in the size of the oscillations and the associated increase in the period is characteristic of a canard explosion [7]. Studying the time histories in panels (b1) and (b2) provides further insight. In particular, note that when  $V_x$  is at its minimal value and the gradient is zero the corresponding part of the  $V_y$  curve has a very steep gradient. This suggests that there is a separation of time scales, where  $V_x$  acts as the slow variable and  $V_y$  as a fast variable.

Due to the complexity of the equations of motion under consideration it is not possible to identify the timescale explicitly. However, it is possible to provide numerical evidence that the sharp increase in the size of the oscillations is indeed a canard explosion. In order to do this we constrain the system so that the dynamics of the slow variable is frozen, treating  $V_x$  as a parameter. Figure 3.10 shows the steady states of the frozen system computed for fixed  $\delta = 10.35^\circ$  (at  $H_2$ ) and varying  $V_x$  as a parameter plotted against  $V_y$ . We find that the system exhibits the main feature of a canard orbit: very close to the Hopf bifurcation  $H_2$  in the full system there is a corresponding limit point bifurcation  $L$  in the frozen system [13]. The distance between the bifurcations is of order  $\varepsilon$ , where  $\varepsilon$  is the time-scale ratio of the system. Also plotted in Figure 3.10 are phase portraits of the periodic solutions at  $\delta = 9.89^\circ$  (small closed curve) and  $\delta = 9.81^\circ$  (large closed curve). The curve of steady-state solutions in the frozen system organises the dynamics of the full system. In particular, it is expected that the periodic solutions emerging from  $H_2$  should follow the stable part of the frozen system close to  $L$ , which is indeed the case. Note that the periodic solutions are plotted for a value of  $\delta$  below  $H_2$  so that the curves are slightly separated near  $L$ . We also see that the periodic solutions follow a section of the unstable branch of the frozen system which is a characterising property of canard-type cycles. In particular, at  $\delta = 9.89^\circ$  the periodic solution follows the unstable

branch and then moves back up to the stable branch. At  $\delta = 9.81^\circ$  the periodic solution follows the unstable branch for longer, moves down and away from the unstable branch before jumping up to the stable branch at  $V_x \approx -1\text{m/s}$ . Using terminology from [13], we can identify the smaller oscillation in Figure 3.10 as a canard orbit ‘without head’ and the larger oscillation as a canard orbit ‘with head’.

The results discussed here provide strong numerical evidence that, from a theoretical point of view, the transition from a recoverable loss of lateral stability to an unrecoverable loss of stability is a canard explosion. Furthermore, the canard explosion is directly linked to a physical property of the system: the saturation of the force generated at the outer landing gear during a turn. Initial investigations have shown that the system’s time-scale ratio  $\varepsilon$  decreases with both  $\delta$  and  $T$ . This implies that, for a Hopf bifurcation at a smaller value of  $\delta$  and  $T$ , the transition to the large amplitude oscillations occurs closer to  $H$  and that the transition to laterally unstable behaviour is even more sudden.

### 3.7 Discussion

We presented derivation and implementation details of a fully parameterized mathematical model of an Airbus A320 aircraft. The new mathematical model has been validated against an existing industry-tested SIMMECHANICS model that was used in a previous study. Specifically, a comparison between one-parameter bifurcation diagrams of the two models revealed a consistent and accurate agreement over the full range of steering angle for a particular configuration of the aircraft, both for turning solutions as well as a bifurcating branch of periodic solutions (representing unstable turns).

The mathematical model was developed to improve functionality and computational efficiency when used with continuation software. An extensive bifurcation analysis in several operational parameters demonstrated that the mathematical model indeed allows for much more wide-ranging studies of turning as a function of a number of operational parameters. The results of the computations were presented as surfaces of solutions, where the steering angle and the centre of gravity position of the aircraft served as the main parameters. This provides an effective way of representing the possible dynamics over the complete range of these two parameters in a single figure. Furthermore, it makes it possible to consider sensitivity questions via a study of the influence of other parameters on the solution surface. As we demonstrated for a heavy and a light aircraft, there are qualitative changes of the solution surface when the thrust level is changed. Corresponding solution surfaces of the two cases are related qualitatively via a thrust offset of 4% of maximal thrust. Importantly, from a practical point of view, the region of laterally unstable solutions was found to increase in size more rapidly with increasing thrust for the light aircraft case.

A separate bifurcation study was carried out in terms of an additional parameter, the friction coefficient of the tyres. It was found that a reduction in the level of friction had the same effect as an increase in the thrust level. Specifically, we found a qualitative agreement between the surfaces of solutions computed in terms of either parameter. Additionally, a steering angle of  $3.5^\circ$  was identified as an upper bound when making stable high-velocity turns for the light case. This bound was also identified in computations performed in terms of the CG position

and thrust level. Overall, this result is consistent with respect to the variation of three different parameters.

Finally, the concluding results section of this chapter provided a theoretical explanation for the apparently discontinuous jump in the amplitude of periodic solutions identified in Chapter 2. It was shown that the system of equations shows behaviour characteristic of separated time scales and canard-type oscillations. The sharp increase in the size of the oscillations, a canard explosion, was found to be directly related to the saturation of the outer main landing gear tyres. Examples from the literature of models that exhibit canard-type oscillations generally tend to be quite simplified and abstract. Here, we provided a concrete example for which the associated phenomena can be directly related to the physical behaviour.



# Chapter 4

## Lateral loads during typical taxiway turns

### 4.1 Introduction

The landing gears of commercial aircraft are subject to substantial lateral loads during taxiing. For example, when exiting the runway at relatively high velocity, it is necessary for the tyres to generate sufficiently large lateral forces to complete the manoeuvre. There is a trade-off between increasing the structural strength of a landing gear to accommodate larger loads and the associated weight penalty. Therefore, it is important to identify the maximal lateral load values and the conditions under which they occur. This information can be used to assess the suitability of current regulations, to inform the design of future aircraft and to improve operational practice.

The regulation imposed by the FAA on the lateral loads experienced during turning for the certification of new civil aircraft is specified in Federal Aviation Regulation (FAR) 25.495. Termed the 0.5g lateral acceleration criterion, the regulation has two key parts with regards to the lateral loads experienced at the aircraft's CG position. Firstly, the limit loads during steady turning must not exceed 0.5g laterally. Secondly, each gear must structurally be able to withstand half of its maximum static vertical load applied laterally. In the regulation there is an inherent assumption that the limiting lateral load of 0.5g is evenly distributed between the aircraft's landing gears. The FAA have expressed concerns about the suitability of this regulation for the certification of modern passenger aircraft; in particular, the regulation is perceived to be too conservative for larger aircraft that have more than two main landing gears [16, 22]. With the aim of evaluating the existing regulation, the FAA have instrumented in-service aircraft and carried out a series of extensive studies to determine the actual lateral loads experienced during ground manoeuvres [16, 22, 47, 55].

In this chapter, the specific aim is to investigate lateral loading during ground manoeuvres in order to assess the suitability of the regulation described above. First of all, it is necessary to give further details of the existing investigations carried out by the FAA. Reference [47] provides a statistical analysis of flight and loads data from a specific in-service aircraft recorded over the course of more than 30,000 flight hours. Included in the report is relevant usage data; for example, cumulative occurrences of lateral load factor recorded during different phases of the aircraft's ground operations. The later study [55] summarises and compares such data recorded from a range of different size aircraft. The more recent study [22] focuses specifically

on lateral loads during ground manoeuvres and makes improvements in terms of the presentation of the data. In particular, the data is organised by aircraft model to allow comparison between the lateral loads experienced during different ground phases. Figure 4.1, reproduced from Reference [22], shows cumulative occurrences of lateral load per flight scaled in terms of the operating weight for an Airbus A320. The data is broken up into different phases of the aircraft's ground operation. We focus on the loads experienced during turning; the relevant data in this study is that recorded during the taxi-in, taxi-out, landing roll and runway turn-off phases. The maximal lateral load factor, scaled by aircraft weight, recorded during the taxi-out phase is 0.2g, during the taxi-in phase it is 0.19g, during the landing roll phase it is 0.25g, and during the turn-off phase it is 0.24g. For convenience, these phases are grouped together as follows. The taxi-out and taxi-in phases are grouped together, and denoted the taxi phase, because they consist of similar manoeuvres; the overall maximal lateral load factor for the taxi phase is 0.2g. The landing roll and turn-off phases are grouped together and denoted the runway turn-off phase. We include the landing roll, which immediately precedes the runway turn-off, in order to capture loads recorded as the turn-off manoeuvre is initiated. The overall maximal lateral load factor for the runway turn-off phase is 0.25g. Larger loads occur during runway turn-off due to greater velocities immediately after landing. The data from this study suggests that the regulation limit for the lateral load factor is conservative. The effect of asymmetric loading between the landing gears is not taken into account in Reference [22] and information with regards to the conditions under which specific lateral load values are attained is limited. The most recent study [16] presents limited ground test data recorded from an instrumented large commercial aircraft with more than two main landing gears. The significance of asymmetric loading between the main landing gears is investigated, but no information is provided about the nose landing gear. For specificity, in the remainder of this chapter, we compare our results with usage data from Reference [47] and the scaled loads data for a specific medium-sized passenger aircraft from Reference [22].

A general approach to evaluate an aircraft's performance across an entire operating region for specific turning manoeuvres is presented. We focus on two types of turning manoeuvre: a runway turn-off manoeuvre that corresponds to the runway turn-off phase data, and a taxiway-to-taxiway transition that corresponds to the taxi phase data. We consider that the maximal lateral load factors for the taxi phase and the runway turn-off phase represent a practical upper bound that is not exceeded in the associated turning manoeuvres. Due to the large size of the data sets represented by the FAA studies, we reason that the limit lateral load factors are not surpassed in the day-to-day operation of the aircraft. With the aim of studying the actual landing gear loads at the limits of operation, we define a parameterized turn in terms of the turn approach velocity and the steering input during the turn. Taking into account the runway and taxiway geometry, we are able to relate the parameterized turn directly to the two manoeuvres under consideration. Parameter values at which the limit lateral load cases occur are identified; based on this information operating regions are defined. We find the actual gear loads at the limits of the operating regions and, therefore, at the limit of the aircraft's operation. The maximal gear loads are found for the two types of manoeuvre and two different mass cases (operating weights). We study the effect of asymmetric lateral loading between all the landing gears and the effect of different overall mass on the actual gear loads experienced. We find that the lateral load factor at CG is sufficient for the prediction of the maximal loads at the main landing gears, but not sufficient for the prediction of loads at the nose gear. Furthermore, we find that the loads at the nose gear are significantly underestimated by the lateral load factor

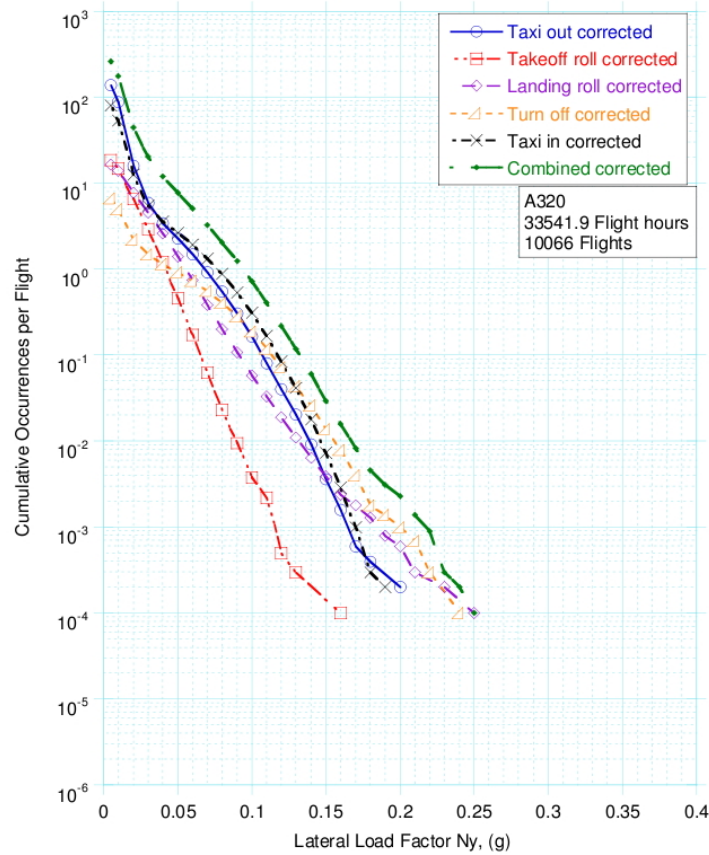


**Figure 4.1.** FAA instrumentation data (reproduction of figure A-27 from Reference [22]) showing cumulative occurrences per flight of lateral load factor, corrected/scaled by operating weight, separated into different ground phases.

at CG. Our results suggest that, for the specific aircraft under consideration, the existing regulation is too conservative for the main landing gears, but this is not necessarily the case for the nose gear. Other regulations, for example the towing regulation FAR 25.509, may account for larger lateral loads on the nose gear; however, the result is still important with respect to fatigue loading. An advantage of the general approach presented is that the limits of operation can be defined in terms of any user specified criteria. As an example, we carry out a similar study with operating regions defined in terms of a criterion that ensures efficiency of the manoeuvres. Overall, the approach presented here gives insights into the conditions under which the maximal loading cases identified in the FAA data occur, and extended information about actual gear loads at the limits of operation. As we demonstrate, the approach is not limited to the study of the extremes of operation. Furthermore, although we focus on the loads experienced at individual landing gears, the approach is applicable for the study of any aircraft states of interest.

The main focus in this chapter is the lateral loads experienced during stable turning. Initial investigations showed that during typical taxiway turns the maximal lateral load values occur during the transient period whilst the aircraft is still converging to its stable turning circle so-

lution. Therefore, the approach taken in this chapter is different from the steady-state analysis presented in earlier chapters; here, we present a transient analysis of turning manoeuvres. In addition to allowing for the accurate prediction of maximal lateral load values, we are able to directly relate the resultant trajectories to specific taxiway turns. Furthermore, we are able to compare the result of the transient analysis with the steady-state analysis presented in earlier chapters. Here, as in earlier chapters, we identify regions of operation for which the aircraft exhibits a laterally unstable behaviour and compare the results between the two types of analysis. This provides further insight into the suitability of the steady-state analysis for predicting the safe operation of the aircraft.

### 4.1.1 Specific loading cases

In this chapter we utilise the fully parameterized mathematical model described in Chapter 3. We define two mass cases that allow for convenient comparison with the loads data presented in Reference [22]. In the FAA study, the recorded lateral loads are scaled in terms of the aircraft's maximum landing weight (MLW) of 64560kg. Here, the loads are scaled in the same way. A comparison of the load values reported in Reference [22] before and after this scaling shows that the maximal lateral load cases correspond to a mass value of approximately  $0.75 \times \text{MLW} = 48420\text{kg}$ , which is close to the minimal operating weight recorded in Reference [47]. Therefore, we consider a heavy operating case at the MLW and a light operating case at  $0.75 \times \text{MLW}$ ; throughout this chapter, the light and heavy operating cases refer to these values and not those defined in earlier chapters. In the remainder of this chapter we refer to the lateral load factor  $N_{CG}$  as the maximal lateral load  $N_y$  recorded at the aircraft CG position during the turn, scaled by the ratio of the operating weight (OR) with the MLW. So, the lateral load factor  $N_{CG} = \max(N_y) \times \frac{\text{OR}}{\text{MLW}}$ . Throughout this chapter we consider a forward CG position at 17% of the aircraft's Mean Aerodynamic Chord [8]. In the results sections of this chapter, the loads experienced at individual landing gears are discussed. For consistency, we scale the loads at the landing gears to allow direct comparison with loads at the CG position. The loads on the individual gears are normalised with respect to maximum vertical load on the gear under static loading. For the Nose Landing Gear (NLG) this corresponds to a heavy aircraft (at MLW) with a forward CG position; the corresponding vertical load under static loading is 92 kN. For the Main Landing Gears (MLGs) we consider a heavy aircraft with an aft CG position; the corresponding vertical load is 300 kN. In the results presented here, we assume that the aircraft always turns to the right and, therefore, in this case we can define the Outer Landing Gear (OLG) as the left-hand gear and the Inner Landing Gear (ILG) as the right-hand gear. We refer to the lateral gear load  $N_{NLG}$ ,  $N_{ILG}$  or  $N_{OLG}$  as the maximal load recorded at the respective landing gear during the turn, divided by the static load values given above. For example, a lateral NLG load of  $N_{NLG} = 0.5$  corresponds to an actual load at the NLG of  $0.5 \times 92 \text{ kN} = 46 \text{ kN}$ .

The results in this chapter are organised as follows. In Section 4.2 the parameterized turn is described. In Section 4.3 we find operational regions for different types of turn in terms of the parameters. In Section 4.4 the maximal lateral loads at the limits of the operational regions are determined. New operating regions are defined in Section 4.5 with respect to the efficiency of turns. In Section 4.6 we compare the continuation analysis and transient analysis. A discussion of the results in this chapter is presented in Section 4.7.

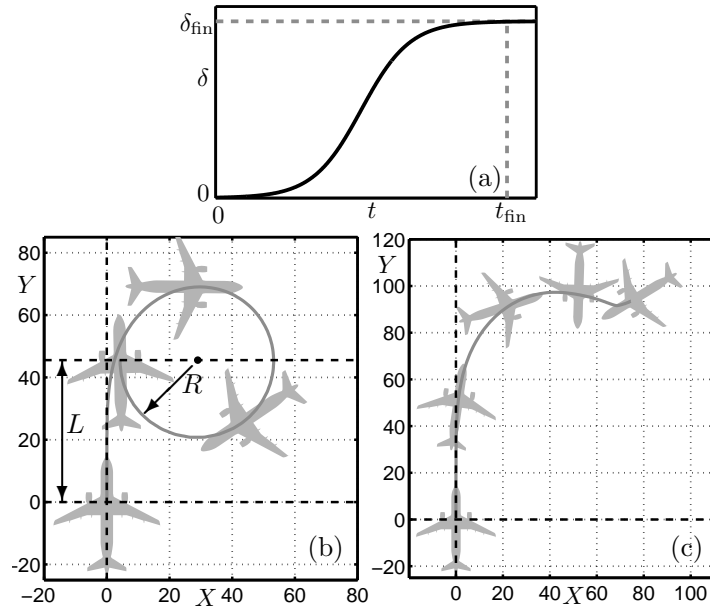


**Figure 4.2.** Panel (a) shows the steering profile, ramping up from  $0^\circ$  to the target steering angle  $\delta_{\text{fin}}$  in time  $t_{\text{fin}}$ . Panels (b) and (c) show traces of the aircraft's CG (grey curve) for the parameterized turn with  $(\delta_{\text{fin}}, V_{\text{init}}) = (29^\circ, 11\text{m/s})$  and  $(\delta_{\text{fin}}, V_{\text{init}}) = (29^\circ, 15\text{m/s})$ , respectively. In panel (a)  $t = 0$  corresponds to the origin in panels (b) and (c). In panel (b) the black dot is the centre of the attracting turning circle with radius  $R$ . Dashed black lines illustrate the measurement of the lag  $L$  during convergence to the turning circle. In panel (c) the aircraft loses lateral stability and at the final point in the trajectory it is stationary.

## 4.2 Generic parameterized turn

In this section a parameterized turn appropriate for the study of lateral loading during taxi manoeuvres is defined. The aim is to characterise a general turning procedure that is representative of pilot practice. Furthermore, for any given taxiway manoeuvre, there are a number of ways to perform that manoeuvre. Dependent on factors such as the velocity when entering a turn and steering characteristics, the lateral loads experienced during the manoeuvre vary significantly. The various factors discussed here are taken into account in the definition of a parameterized turn.

Typically, when the aircraft is approaching a turn on a straight section of taxiway the brakes are applied to achieve a desired velocity before entering the turn. After braking the turn is initiated with the application of steering. The velocity before entering the turn is represented here by the parameter  $V_{\text{init}}$  (with units m/s). In the simulations the initial condition describes the aircraft travelling in a straight line with the thrust set so that it is at equilibrium with fixed velocity  $V_{\text{init}}$ . From the initial condition the turn is initiated with the application of the steering; the steering angle is ramped up from  $0^\circ$  to a target value denoted  $\delta_{\text{fin}}$  (given in degrees) which is taken as the second parameter to characterise the turn. The idealised steering profile used here is shown in Figure 4.2(a); it is represented by the function

$$\delta_N(t) = \frac{\delta_{\text{fin}}}{2} \left[ 1 + \tanh \left( \frac{\delta_{\text{rate}}}{\delta_{\text{fin}}} (2t - t_{\text{fin}}) \right) \right],$$

where  $\delta_N(t)$  is the steering angle applied at the nose gear at time  $t$ ; furthermore,  $\delta_{\text{rate}}$  is the fixed maximum steering rate and  $t_{\text{fin}} = \frac{3\delta_{\text{fin}}}{\delta_{\text{rate}}}$  is the required time to ramp up the steering such that  $\delta_N(t_{\text{fin}}) = \delta_{\text{fin}}$ . The realistic value of  $\delta_{\text{rate}} = 12\text{deg/s}$  is used and the maximum rate is achieved at  $t = \frac{t_{\text{fin}}}{2}$ .

In the remainder of this section we study the properties of the parameterized turn for different values of the parameter pair  $(\delta_{\text{fin}}, V_{\text{init}})$  of target steering angle and initial velocity. We initially study the resulting trajectories independently of the taxiway geometry, and in Section 4.3 we relate the trajectories directly to taxiway geometry. Each simulation gives a trajectory describing the motion of the aircraft over the  $(X, Y)$ -ground plane and associated time history data for the system states; the coordinates  $X$  and  $Y$  are given in metres (m). It is straightforward to extract detailed information from the model, such as the forces experienced at the ground-type interactions.

In Chapter 2 we identified two possible types of behaviour; when the aircraft makes a turn it can either converge to a stable turning circle solution or, if the manoeuvre is too aggressive, there is a loss of lateral stability. Figure 4.2(b) and (c) are two example trajectories; plotted is a trace of the aircraft's CG position (grey curve) over the  $(X, Y)$  ground-plane with markers plotted to scale at equally spaced time intervals that indicate the aircraft's orientation along the trajectory. Figure 4.2(b) shows a trajectory computed for  $(\delta_{\text{fin}}, V_{\text{init}}) = (29^\circ, 11\text{m/s})$ , for which the aircraft converges to a stable turning circle after a transient period. Illustrated are two quantities that describe the geometry of a stable trajectory. The radius of the turning circle to which the aircraft converges is denoted  $R$  (with units m). The longitudinal distance travelled from the initiation of the steering ramp at  $t = 0$  to the point where the centre of the turning circle is passed is referred to as the approach lag; it is denoted  $L$  (with units m). For illustrative purposes, the parameter values of  $\delta_{\text{fin}}$  and  $V_{\text{init}}$  for the trajectory shown in Figure 4.2(b) were chosen to exaggerate  $L$ . In general, when  $\delta_{\text{fin}}$  is increased the radius  $R$  decreases as the aircraft follows tighter turns; when either  $\delta_{\text{fin}}$  or  $V_{\text{init}}$  is increased the lag  $L$  increases as there is a longer delay before the aircraft makes the turn. Figure 4.2(c) shows a manoeuvre computed for  $(\delta_{\text{fin}}, V_{\text{init}}) = (29^\circ, 15\text{m/s})$ ; with this greater initial velocity the aircraft loses lateral stability. This laterally unstable behaviour has been studied at length in Chapter 2; here we identify the boundary between the two types of behaviour but the main focus is on stable turning.

### 4.2.1 Trajectory geometry

The implementation of a relatively low-order model in Matlab allows for the computation of large numbers of model simulations across a two-dimensional parameter space at low computational cost. A  $200 \times 200$  grid of values for the parameters  $\delta_{\text{fin}}$  and  $V_{\text{init}}$  is taken over the ranges  $\delta_{\text{fin}} \in (2^\circ, 25^\circ)$  and  $V_{\text{init}} \in (5, 25)\text{m/s}$ . The velocity range is chosen to cover values representing relatively low-speed turns up to values in excess of the limits of operation. The maximal  $V_{\text{init}}$  values correspond to a thrust level of approximately 6% of maximum available thrust for the light mass case, and 7% for the heavy mass case. An aircraft trajectory as described in the previous section is computed for each of the  $200 \times 200$  initial conditions in the  $(\delta_{\text{fin}}, V_{\text{init}})$ -plane. Various data are recorded and represented by greyscale maps over an appropriate range.

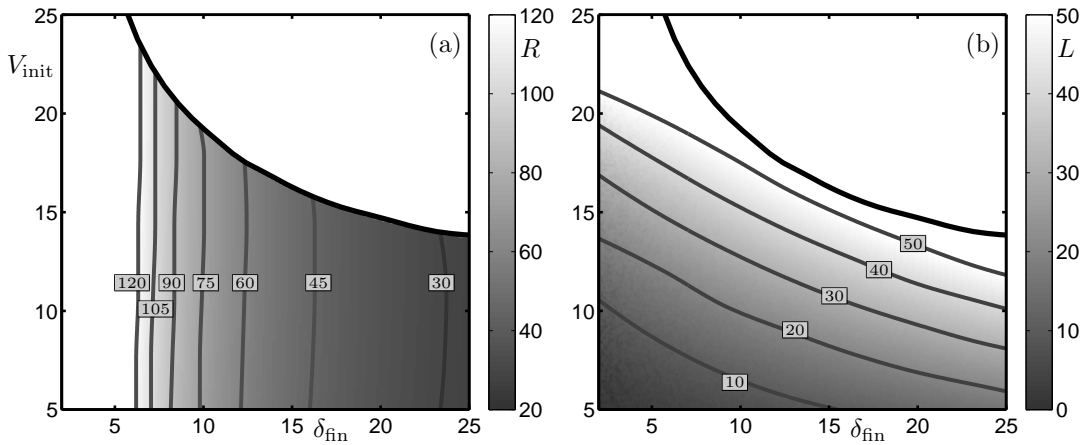


**Figure 4.3.** Greyscale maps showing values of turn radius  $R$  in panel (a) and approach lag  $L$  in panel (b) over the shown range of  $V_{\text{init}}$  and  $\delta_{\text{fin}}$  values; contours are plotted in grey. The thick black curve is the limit of stable turning; white points above it correspond to laterally unstable turns.

Figure 4.3 shows the geometrical measures  $R$  and  $L$  over the grid of  $(\delta_{\text{fin}}, V_{\text{init}})$ -values in panels (a) and (b), respectively. For each value of  $\delta_{\text{fin}}$ , simulations are performed at discrete values of  $V_{\text{init}}$  increasing from  $V_{\text{init}} = 5\text{m/s}$  to  $V_{\text{init}} = 25\text{m/s}$  and points at which there is a transition from stable solutions to laterally unstable solutions are detected. Specifically, if the lateral velocity of the aircraft exceeds  $5\text{m/s}$  then this indicates that lateral stability has been lost. This choice of lateral velocity is consistent with the results in Chapter 2 as a value for which the aircraft has been subject to a loss of lateral stability. The transition occurs along the black curve in each of the panels in Figure 4.3; white points that lie above this curve correspond to laterally unstable turns. Figure 4.3(a) shows that the turn radius  $R$  decreases with an increase in  $\delta_{\text{fin}}$ . Note that it is independent of the initial condition determined by  $V_{\text{init}}$ , which follows from the fact that  $R$  is a measure of the stable turning circle solution to which the trajectories converge. Furthermore, the small changes in thrust used to set  $V_{\text{init}}$  do not affect  $R$ . However,  $V_{\text{init}}$  has a significant effect on the transient behaviour before convergence to a stable turning circle. This is reflected in Figure 4.3(b), which shows that the distance or lag  $L$  travelled by the aircraft before convergence to a stable turning circle increases with  $V_{\text{init}}$ . Recall that  $L$  increases with  $V_{\text{init}}$  because, with a greater initial velocity, the aircraft will travel further before executing the turn. There is also an increase in  $L$  with  $\delta_{\text{fin}}$  because the steering rate is limited; it takes longer for the steering ramp to reach the target steering angle with increased  $\delta_{\text{fin}}$ .

### 4.3 Operating region for typical taxiway turns

In this section we identify operating regions for different types of turning manoeuvre. The aim is to define the regions such that they represent a range of possible ways in which the different manoeuvres are performed. The first step is to relate the parameterized turn described in Section 4.2 to specific turning manoeuvres. Typical taxiway geometries are chosen that are representative for the turning manoeuvre under consideration. In Section 4.3.1 we identify

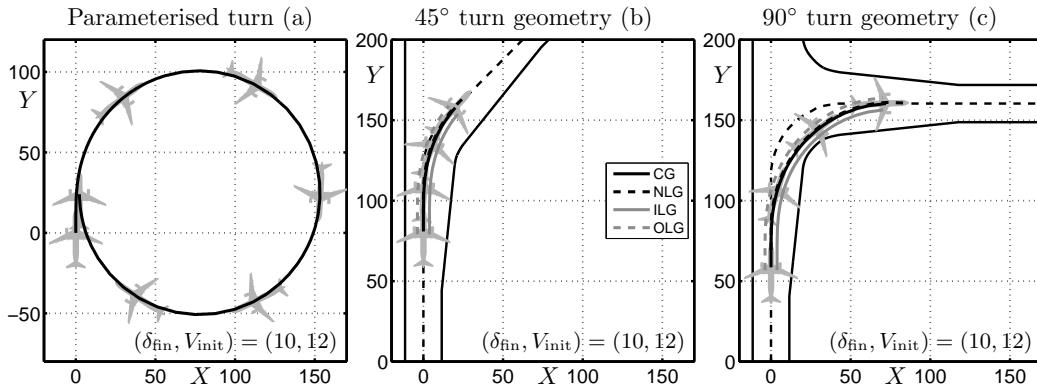


**Figure 4.4.** Panel (a) shows the aircraft trajectory for the parameterized turn at  $(\delta_{fin}, V_{init}) = (10^\circ, 12\text{m/s})$  plotted over the  $(X, Y)$ -ground plane; the aircraft has turned through  $360^\circ$  at the end of the trajectory. Panels (b) and (c) show the taxiway geometry for  $45^\circ$  and  $90^\circ$  turns with the taxiway limits plotted as solid black curves and the turn centre-lines plotted as dashed black curves. In each case the respective section of the parameterized turn is plotted; the trajectories end when the aircraft has turned through  $45^\circ$  and  $90^\circ$  in panels (b) and (c), respectively.

bounds that restrict our study to parameter values for which the aircraft follows a trajectory suitable for the specific taxiway geometry. These bounds ensure that the operating region only consists of parameter values for which the aircraft remains safely within the taxiway geometry and does not excessively overshoot the turn. The second step is to ensure that the parameter values in the operating region do not exceed other criteria for practical turns. In Section 4.1 we concluded that the maximal lateral load factors at CG reported in the FAA studies in Reference [22] are a practical upper bound for the operation of the aircraft. The criterion chosen in Section 4.3.2 is that the lateral load factor during the turn does not exceed the values in the FAA studies for the different types of manoeuvre.

### 4.3.1 Relating parameterized turn trajectories to specific manoeuvres

We describe a general method to relate the parameterized turn output trajectories directly to manoeuvres performed whilst exiting the runway and moving between taxiways. Each trajectory output is effectively fitted to the taxiway geometry upon which the manoeuvre is performed. The initial point in the trajectory is aligned to the entrance vector of the turn and the point on the trajectory at which the aircraft has rotated sufficiently to complete the turn is aligned with the exit vector of the turn. This works on the reasonable assumption that the steering is applied by the pilot at the appropriate distance from the turn entrance. Furthermore, it is assumed here that, if the end point of the aircraft's trajectory is approximately tangential to the exit vector of the turn, then it is possible to straighten out the aircraft to exit the turn. In this way, we are able to relate the data from a single computation at a specific value of  $\delta_{fin}$  and  $V_{init}$  to any turn geometry.

We focus on two types of turning manoeuvre: the runway turn-off manoeuvre and a taxiway-to-taxiway transition. For simplicity we consider the single taxiway geometry of a  $45^\circ$  turn at

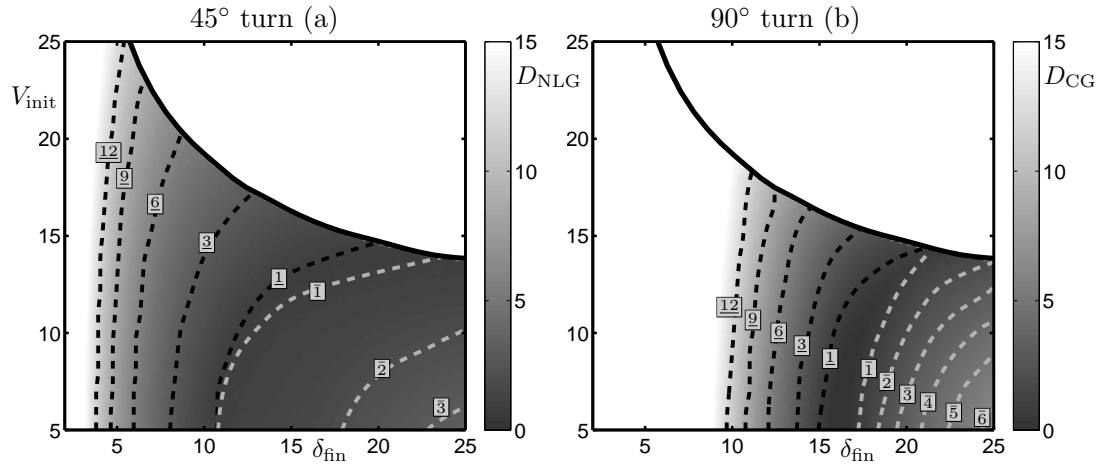


**Figure 4.5.** Greyscale maps showing  $D_{NLG}$  for the  $45^\circ$  turn (a) and  $D_{CG}$  for the  $90^\circ$  turn (b). Contours of  $D_{NLG}$  and  $D_{CG}$  plotted as dashed black curves represent an undershoot of the turn centre-line and are labelled with an underlined value; similarly, contours to the right plotted as dashed grey curves represent an overshoot of the turn centre-line and are labelled with a bar over the value.

a group V category airport [15] to be representative of a shallow runway turn-off manoeuvre. We choose the group V category as the standard airport geometry for which manoeuvrability studies are performed. Secondly, we consider a  $90^\circ$  turn at a group V category airport to be representative of the taxiway-to-taxiway transition. To allow for direct comparison the turn radius is 45m for both geometries. We now demonstrate the method described above by relating a single output trajectory to two different turning manoeuvres. Figure 4.4(a) shows the output trajectory of the parameterized turn for  $(\delta_{fin}, V_{init}) = (10^\circ, 12\text{m/s})$  plotted over the  $(X, Y)$ -ground plane; the aircraft has turned through  $360^\circ$  at the end of the trajectory. Panels (b) and (c) show the geometry for a  $45^\circ$  and a  $90^\circ$  turn, respectively. The taxiway limits are plotted as solid black curves and the turn centre-lines, straight sections of which correspond to the entrance and exit vectors of the turn, are plotted as dashed black curves. In each case a section of the parameterized turn is plotted over the taxiway geometry; the trajectories end when the aircraft has turned through  $45^\circ$  or  $90^\circ$ , as appropriate. Traces of the aircraft's CG position and the path of each landing gear are shown. For the same values of  $(\delta_{fin}, V_{init}) = (10^\circ, 12\text{m/s})$ , the parameterized turn corresponds to following the turn centre-line closely for the  $45^\circ$  turn and the ILG almost exiting the taxiway for the  $90^\circ$  turn.

The pilot can ensure that the ILG remains a safe distance from the edge of the taxiway by following the turn centre-line with either the NLG or the approximate aircraft CG position. The former approach of following the turn centre-line (painted on the taxiway) with the NLG is used for shallow turns such as the  $45^\circ$  turn that we consider here. In particular, when turning at speed this method allows the pilot to control the turn easily as the NLG is approximately at the same position as the cockpit. Therefore, to study the  $45^\circ$  turn we define  $D_{NLG}$  (in m) as the maximum deviation of the NLG from the turn centre-line; for the trajectory shown in Figure 4.4(b) the NLG slightly undershoots the turn and  $D_{NLG} \approx 2.5\text{m}$ . For a  $90^\circ$  turn the pilot aims to follow the turn centre-line with the approximate position of the aircraft's CG; this ensures that the ILG does not come close to the edge of the taxiway even for a tight

turn. Therefore, to study the  $90^\circ$  turn we define  $D_{CG}$  (in m) as the maximum deviation of the CG position from the turn centre-line; for the trajectory shown in Figure 4.4(c) the aircraft significantly undershoots the turn and  $D_{CG} \approx 12.5\text{m}$ . The aircraft should operate such that all landing gears are at least 4.5m from the edge of the taxiway as specified by the design of the taxiway geometry [15]; here we relax this to 3m to capture turns that marginally exceed the safety limit. In the trajectory shown in Figure 4.4(c) the ILG comes within 3m of the edge of the taxiway. We use the two properties  $D_{NLG}$  and  $D_{CG}$  to determine bounds that identify suitable trajectories in the  $(\delta_{fin}, V_{init})$ -plane. Specifically, a left-hand bound on  $\delta_{fin}$  and  $V_{init}$  ensures that the ILG does not come too close to the edge of the taxiway. A right-hand bound on  $\delta_{fin}$  and  $V_{init}$  ensures that the aircraft does not overshoot the turn centre-line (with the NLG in the  $45^\circ$  turn or the CG in the  $90^\circ$  turn). An excessive overshoot of the centre-line is prohibited as this corresponds to the aircraft following a turn of unnecessarily small radius. Although the quantities  $D_{NLG}$  and  $D_{CG}$  are closely related, it is convenient to consider them separately for the two different turns.

Figure 4.5(a) and (b) show greyscale maps of  $D_{NLG}$  for the  $45^\circ$  turn and  $D_{CG}$  for the  $90^\circ$  turn, respectively. Contours of  $D_{NLG}$  and  $D_{CG}$  plotted as dashed black curves represent an undershoot of the turn centre-line and are labelled with an underlined value. Similarly, contours to the right plotted as dashed grey curves represent an overshoot of the turn centre-line and are labelled with a bar over the value. In Figure 4.5(a) there is a dark central region bounded by the curves  $D_{NLG} = \underline{1}\text{m}$  and  $D_{NLG} = \bar{1}\text{m}$  that represents the trajectories for which the NLG closely follows the turn centre-line (within  $\pm 1\text{m}$ ). Similarly, in Figure 4.5(b) the region bounded by the curves  $D_{CG} = \underline{1}\text{m}$  and  $D_{CG} = \bar{1}\text{m}$  represents the trajectories for which the CG position closely follows the turn centre-line (within  $\pm 1\text{m}$ ). The shading gets lighter to the left of the central region representing a greater undershoot and lighter to the right of the central region indicating a greater overshoot. Note that away from the central region the contours are closer together for the  $90^\circ$  turn because the aircraft must follow the turn centre-line for longer. We now define the operational limits for the two turn cases in terms of  $\delta_{fin}$  and  $V_{init}$  by identifying specific contours in Figure 4.5. For the  $45^\circ$  turn the contour  $D_{NLG} = \underline{12}\text{m}$  provides the left-hand bound, which ensures that the ILG remains at least 3m from the edge of the taxiway. The contour  $D_{NLG} = \bar{1}\text{m}$  provides the right-hand bound, which ensures that the aircraft does not excessively overshoot the turn centre-line. Similarly, we define the bounds for the  $90^\circ$  turn as  $D_{CG} = \underline{12}\text{m}$  and  $D_{CG} = \bar{1}\text{m}$ . Again, these bounds ensure that the ILG remains at least 3m from the edge of the taxiway and the aircraft does not excessively overshoot the turn centre-line. From a practical point of view the undershoot criteria are more important. The bounds identified here are used to define an operational region in terms of  $\delta_{fin}$  and  $V_{init}$  in Section 4.3.2.

### 4.3.2 Maximal lateral loading conditions and operating regions

We now identify values of the parameters  $\delta_{fin}$  and  $V_{init}$  that coincide with trajectories for which the aircraft experiences the limiting lateral load factors reported in Reference [22]. Recall from Section 4.1 that the maximal lateral load factor recorded for the aircraft under consideration is 0.25g during the runway turn off phase and 0.2g during the taxi phase. Therefore, the aim here is to determine values of the parameters  $\delta_{fin}$  and  $V_{init}$  for which lateral load factor generated is 0.25g for a  $45^\circ$  turn and 0.2g for a  $90^\circ$  turn. This information describes an upper bound on the operation of the aircraft during taxiing for the two types of turn.

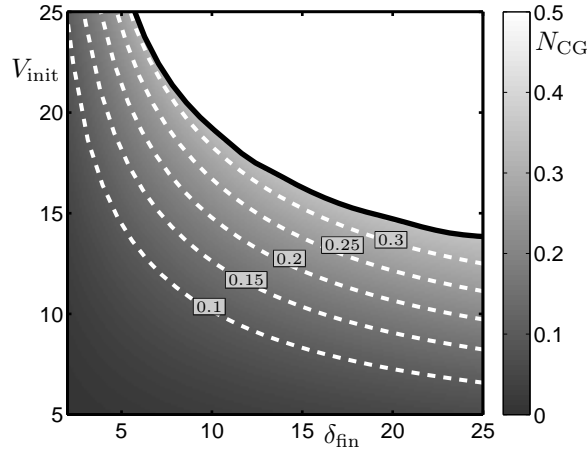


**Figure 4.6.** Greyscale map of the maximal lateral load factor  $N_{CG}$  for the output trajectory initialised from each  $(\delta_{fin}, V_{init})$ -pair; dashed white curves are contours of  $N_{CG}$ .

Figure 4.6 shows a greyscale map of the lateral load factor  $N_{CG}$  for the trajectory represented by each  $(\delta_{fin}, V_{init})$ -pair; dashed white curves show contours of  $N_{CG}$ . The figure shows that for turns performed at high velocity, the lateral load factor increases rapidly with increased steering angle. Conversely, at lower velocities  $N_{CG}$  increases slowly with increased steering angle. The lateral stability boundary appears to coincide with a limit lateral load factor of approximately 0.35g. Note that for all the aircraft considered in Refs. [55, 22, 16] the lateral load factor does not exceed 0.35g. With increasing  $N_{CG}$  the contours bound a larger region; this property that  $N_{CG}$  increases as the lateral stability boundary is approached is important. In general, for any aircraft, an increase in the lateral load factor with increased  $V_{init}$  or  $\delta_{fin}$  is expected: when following a steady turning circle then  $N_{CG} \propto \frac{V^2}{R}$  (or approximately,  $N_{CG} \propto V^2 \times \delta$ ), where  $V$  is the aircraft's velocity and  $R$  is the radius of the turning circle corresponding to the steering angle  $\delta$ .

From the maximal lateral load values in the FAA studies we can infer that for the runway turn-off manoeuvre the aircraft's operation corresponds to values of  $\delta_{fin}$  and  $V_{init}$  below the 0.25g contour. Similarly, for taxiway-to-taxiway transitions the aircraft's operation corresponds to values of  $\delta_{fin}$  and  $V_{init}$  below the 0.2g contour. We use this information in conjunction with the bounds defined in terms of  $D_{NLG}$  and  $D_{CG}$  to define operating regions for the two types of turn.

Figure 4.7(a) and (b) show the resulting operating regions for the 45° turn and the 90° turn, respectively. The left-hand limits of the operating regions shows that for increasing degree of turn, a larger  $\delta_{fin}$  is required to keep the ILG a suitable distance from the edge of the taxiway; compare  $D_{NLG} = \underline{12}$  in panel (a) with  $D_{CG} = \underline{12}$  in panel (b). Again, the right-hand limit occurs at higher values of  $\delta_{fin}$  with increased degree of turn. A larger steering angle is required for the NLG or CG position to follow the turn centre-line and, for the 90° turn, the aircraft must follow the centre-line for longer; compare  $D_{NLG} = \bar{1}$  in panel (a) with  $D_{CG} = \bar{1}$  in panel (b). For the 45° turn, the bound on  $N_{CG}$  is at larger values of  $\delta_{fin}$  and  $V_{init}$  and closer to the lateral stability boundary; compare  $N_{CG} = 0.25$  in panel (a) with  $N_{CG} = 0.2$  in panel (b). Due to the larger velocities associated with the runway turn-off manoeuvre (45° turn), the corresponding

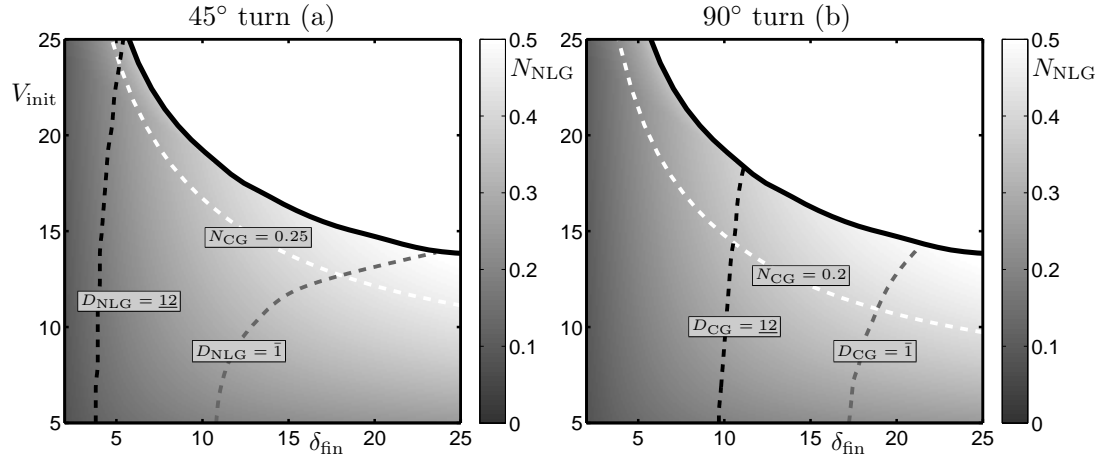


**Figure 4.7.** Greyscale maps show the lateral NLG load  $N_{NLG}$  for the trajectory represented by each  $(\delta_{fin}, V_{init})$ -pair. The operating regions are represented by the values of  $\delta_{fin}$  and  $V_{init}$  that lie inside bounds on  $D_{NLG}$ ,  $D_{CG}$  and  $N_{CG}$  as shown.

lateral load factor is larger than during taxiway-to-taxiway transitions ( $90^\circ$  turn). The operating regions are plotted over a greyscale map of the lateral NLG load  $N_{NLG}$ . It is convenient to show this information because the maximal landing gear loads across each operating region are studied in Section 4.4. We choose  $N_{NLG}$  because the lateral NLG loads come closest to exceeding the FAR. Note that the values of  $N_{NLG}$  are independent of the degree of the turn because the maximal loads on the NLG occur whilst the steering is being ramped up to  $\delta_{fin}$ ; this is before the aircraft has turned through  $45^\circ$  (the same holds for the ILG and OLG within the operating regions). The operating region for the  $45^\circ$  turn encompasses values of  $\delta_{fin}$  and  $V_{init}$  corresponding to values of  $N_{NLG}$  that are close to the regulation's limit of  $N_{NLG} = 0.5$ . An important feature of the data shown in Figure 4.7 is that for both operating regions  $N_{NLG}$  is uniformly increasing as  $\delta_{fin}$  and  $V_{init}$  approach the  $N_{CG}$  boundary. This property also holds for lateral ILG and OLG loads. Therefore, to find the maximal lateral gear loads in a given operating region it is sufficient to study the loads solely along the  $N_{CG}$  boundary.

#### 4.4 Maximal lateral gear loads in operating regions

Since the maximal lateral gear loads in each operating region are attained at the  $N_{CG}$  boundary, we parametrise the  $N_{CG}$  curve to get a representation of the maximal lateral gear loads in the operating regions depending on  $\delta_{fin}$ . Effectively the problem of finding the limiting loads has been reduced to computing these values along a one-dimensional curve. Given that the criteria for defining a region of standard operations can be applied to any aircraft configuration, the limiting loads are computed for light and heavy aircraft cases. For both mass cases and the two types of taxiway turn, the lateral gear load values are found along the corresponding  $N_{CG}$  boundary at 50 discrete values of  $\delta_{fin}$ . In this way, the lateral gears load values are extracted along the operating limit curves in Figure 4.7.

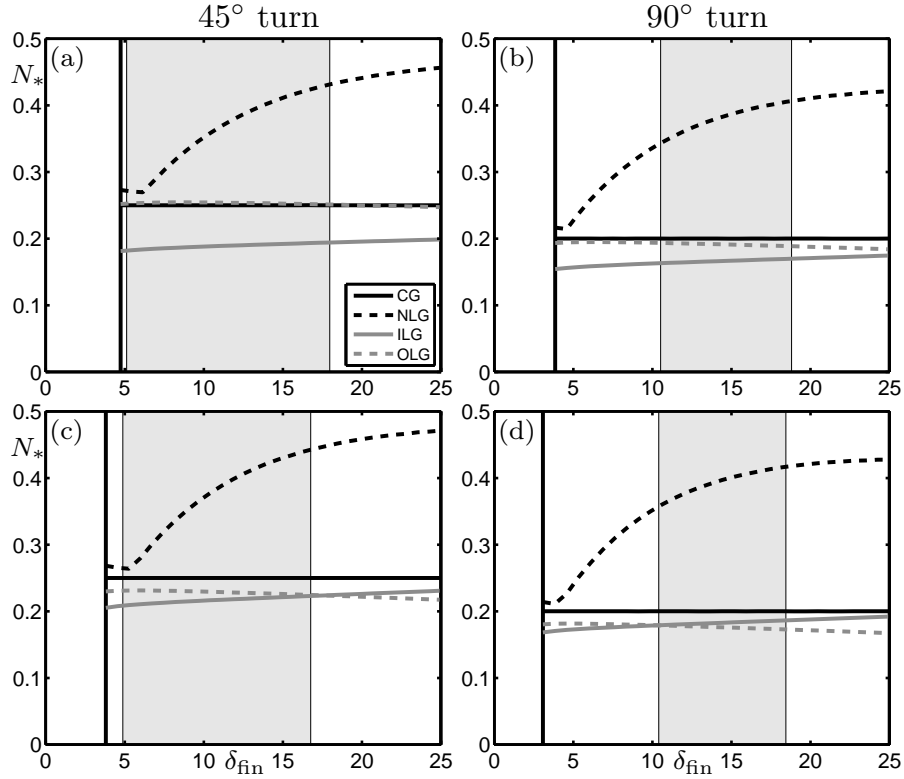


**Figure 4.8.** The lateral loads  $N_*$  (at CG, NLG, ILG and OLG) computed along the  $N_{CG}$  boundary curves and parameterized in terms of  $\delta_{fin}$ . Panels (a) and (b) show data for the light aircraft case and panels (c) and (d) for the heavy aircraft case; turn degree is indicated at the top of the figure. In each panel the region shaded in grey represents the values of  $\delta_{fin}$  corresponding to the appropriate operating region as shown in Figure 4.7. A vertical black line indicates the lower extent of the parameterized  $N_{CG}$  curve.

Figure 4.8 shows plots of the lateral gear loads  $N_*$  recorded along the  $N_{CG}$  limit parameterized in terms of  $\delta_{fin}$ . The top two panels (a) and (b) represent the light aircraft case for which the operating regions are shown in Figure 4.7; the bottom panels represent the heavy aircraft case. The first column corresponds to the 45° turn and the second column to the 90° turn. In each panel the (fixed) value of  $N_{CG}$  is plotted as a reference. In each panel of Figure 4.8 vertical black lines indicate the  $\delta_{fin}$  value corresponding to the lower extent of the  $N_{CG}$  curve; the section shaded grey represents the values of  $\delta_{fin}$  corresponding to the appropriate operating region. The limits of the grey region correspond to intersections between  $N_{CG}$  and the appropriate  $D_{NLG}$  and  $D_{CG}$  curves.

First, we focus on the distribution of lateral loads between the ILG and the OLG. The lateral ILG and OLG loads are closely related to the lateral load factor  $N_{CG}$ :  $N_{ILG}$  and  $N_{OLG}$  vary linearly with  $\delta_{fin}$  in all panels of Figure 4.8. Panels (a) and (b) show that, in the light case, for both types of turn,  $N_{OLG}$  is larger than  $N_{ILG}$ . Within the operating region for the 45° turn  $N_{OLG}$  is at most 40% larger than  $N_{ILG}$ ; for the 90° turn the difference is at most 20% larger. This difference can be accounted for by the fact that during a turn the aircraft's weight

shifts to the outside gear and the OLG takes a larger vertical load; in general the lateral load generated by a tyre increases with vertical load. In the heavy aircraft case, for both types of turn, there is a value of  $\delta_{\text{fin}}$  above which  $N_{\text{ILG}}$  is larger than  $N_{\text{OLG}}$ ; see panels (c) and (d). Due to the aircraft geometry the ILG generates a larger slip angle whilst turning. For stable turns the lateral forces generated by the tyres increase with slip angle and in the heavy case there is some value of  $\delta_{\text{fin}}$  for which this effect dominates over the larger vertical load at the OLG. For a heavy aircraft in the operating region for the  $45^\circ$  turn  $N_{\text{OLG}} > N_{\text{ILG}}$  with the values becoming equal at the maximal value of  $\delta_{\text{fin}}$ ; see panel (c). Conversely, in the operating region for the  $90^\circ$  turn,  $N_{\text{ILG}} > N_{\text{OLG}}$  with the values being equal at the minimal value of  $\delta_{\text{fin}}$ ; see panel (d). Across all four cases shown in Figure 4.8, the lateral load factor is a good predictor of the lateral ILG and OLG loads. Furthermore,  $N_{\text{ILG}}$  and  $N_{\text{OLG}}$  are less than or equal to the lateral load factor at CG (with a slight exception for the OLG in Figure 4.8(a)).

Across all four cases shown in Figure 4.8 the lateral NLG loads  $N_{\text{NLG}}$  are greater than  $N_{\text{OLG}}$ ,  $N_{\text{ILG}}$  and  $N_{\text{CG}}$ . The loads at the NLG increase with  $\delta_{\text{fin}}$  and the maximal values occur at the upper limit of  $\delta_{\text{fin}}$ . In the operating regions for the  $45^\circ$  turn  $N_{\text{NLG}}$  is approximately equal to  $N_{\text{CG}}$  for small values of  $\delta_{\text{fin}}$ ; see panels (a) and (c). However, as  $\delta_{\text{fin}}$  increases there is a rapid deviation and the lateral NLG load is vastly underestimated by the lateral load factor at CG. Furthermore, at the upper limit of  $\delta_{\text{fin}}$  the loads at the NLG come close to  $N_{\text{NLG}} = 0.5$ , which is approaching the limit imposed by the FAA. For all values of  $\delta_{\text{fin}}$  in the operating regions for the  $90^\circ$  turn  $N_{\text{NLG}}$  is vastly underestimated by  $N_{\text{CG}}$ ; see panels (b) and (d). Overall, for the fixed values of  $N_{\text{CG}}$  considered here, the corresponding values of  $N_{\text{NLG}}$  can vary by up to 100%. We conclude that studying the lateral load factor at CG alone is insufficient for the prediction of the loads at the landing gears. Note that the large change in mass between the light and heavy cases corresponds to only a marginally increased lateral NLG load. The largest loads at the OLG occur for the light mass case.

## 4.5 Operating region for efficient turns

In Sections 4.3 and 4.4 the upper limit of operation was defined in terms of the maximal lateral load factors shown in Figure 4.1. In this way, the limits of the operating regions represent the extremes of the aircraft's operation. However, the approach presented in this chapter is very flexible and other limits can be defined in a similar way with any relevant criteria that provide a bound within which it is desirable for the aircraft to operate. As an example, we now define operating regions in terms of a target for the efficiency of turns. Specifically, a turn can be considered efficient if during the turn a large proportion of the approach velocity is conserved.

The velocity lost during a turn,  $V_{\text{loss}}$ , is expressed as a percentage by the equation

$$V_{\text{loss}} = 100 \times \frac{V_{\text{init}} - V_{\text{fin}}}{V_{\text{init}}},$$

where  $V_{\text{fin}}$  is the velocity of the aircraft when it reaches the exit vector of the turn. For smaller values of  $V_{\text{loss}}$  less velocity is lost and the turn is more efficient. Figure 4.9 shows greyscale maps of  $V_{\text{loss}}$  for the two types of turn; contours of  $V_{\text{loss}}$  are plotted as white curves. The plots show that more velocity is lost with a higher-degree turn. Specifically, in panel (a) we see that for the  $45^\circ$  turn the maximal value of  $V_{\text{loss}}$  just exceeds 10% in the stable region; the largest

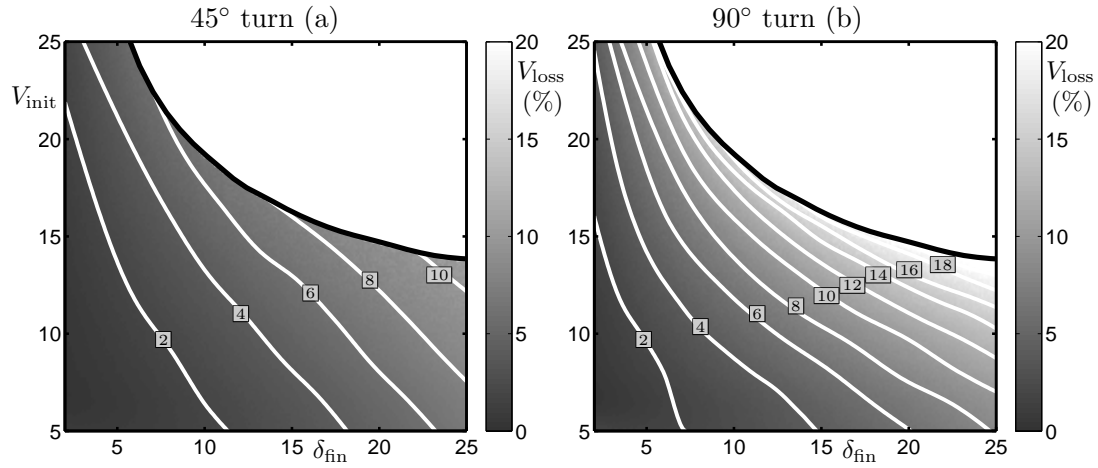


**Figure 4.9.** Greyscale maps showing the percentage of velocity lost  $V_{\text{loss}}$  for the two types of turn for the trajectory represented by each  $(\delta_{\text{fln}}, V_{\text{init}})$ -pair. White curves are contours of  $V_{\text{loss}}$ .

value occurs close to the lateral stability boundary at high  $\delta_{\text{fln}}$ . For the  $90^\circ$  turn, see panel (b), the maximal value of  $V_{\text{loss}}$  just exceeds 18% with the maximal values occurring close to the lateral stability boundary. The relative spacing between the contours for the two types of turn shows that there is a larger penalty in terms of efficiency when increasing  $\delta_{\text{fln}}$  and  $V_{\text{init}}$  for the  $90^\circ$  turn. Therefore, depending on the type of turn, different  $V_{\text{loss}}$  limits are chosen as the criteria for suitably efficient manoeuvres.

We now specify contours of  $V_{\text{loss}}$  to represent upper limits for new operating regions that, as in Section 4.3.2, take into account appropriate limits for  $D_{\text{NLG}}$  and  $D_{\text{CG}}$ . An upper limit of  $V_{\text{loss}} = 4\%$  is taken for the  $45^\circ$  turn and  $V_{\text{loss}} = 8\%$  for the  $90^\circ$  turn. These limits are chosen such that in these new operating regions the lateral load factor does not exceed the maximal values identified in the FAA studies for the light aircraft case. Accordingly,  $N_{\text{CG}} < 0.25g$  along  $V_{\text{loss}} = 4\%$  for the  $45^\circ$  turn, and  $N_{\text{CG}} < 0.2g$  along  $V_{\text{loss}} = 8\%$  for the  $90^\circ$  turn. The same  $V_{\text{loss}}$  limits are chosen for the heavy aircraft case to allow for direct comparison between the mass cases. Figure 4.10 shows the resulting operating regions, again plotted over a greyscale map of  $N_{\text{NLG}}$ . The new operating regions represent a subset of those defined in Section 4.3.2 due to the way in which the  $V_{\text{loss}}$  bounds are chosen.

The lateral load factor and lateral gear loads increase as the  $V_{\text{loss}}$  limit is approached and, therefore, in order to identify the maximal loads in the region we extract the loads along the  $V_{\text{loss}}$  curves. Plots of the lateral load factor and lateral gear loads are shown for the two types of turn and two mass cases in Figure 4.11. For the  $45^\circ$  turn, the lateral load factor  $N_{\text{CG}}$  peaks close to the lower extent of the operating region and steadily drops off as  $\delta_{\text{fln}}$  increases; see panels (a) and (c). For the light case  $N_{\text{OLG}} > N_{\text{ILG}}$  with the loads becoming equal at the upper extent of the operating region; see panel (a). For the heavy case there is a transition from the greater load being the OLG to the ILG with  $N_{\text{ILG}} = N_{\text{OLG}}$  at  $\delta_{\text{fln}} \approx 10^\circ$ ; see panel (c). For the  $90^\circ$  turn, the lateral load factor decreases with increased  $\delta_{\text{fln}}$  in the operating region; see panels (b) and (d). For the light aircraft case  $N_{\text{OLG}} > N_{\text{ILG}}$  with the loads becoming equal at the upper extent of the operating region; see panel (b). For the heavy case  $N_{\text{ILG}} > N_{\text{OLG}}$  and the loads are equal at the lower extent of the operating region; see panel (d). For both turn types

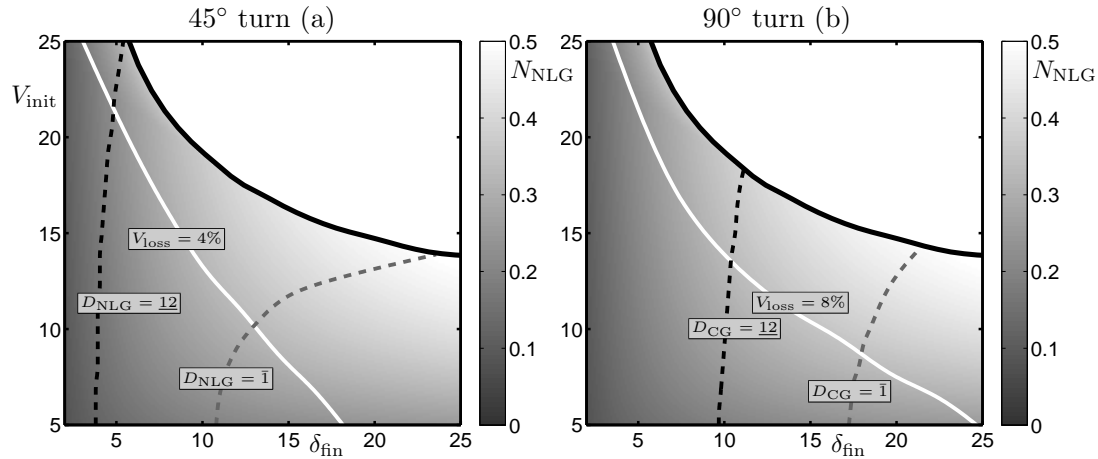


**Figure 4.10.** Greyscale maps showing the lateral NLG load  $N_{NLG}$  for the trajectory represented by each  $(\delta_{fin}, V_{init})$ -pair. The operating regions are the values of  $\delta_{fin}$  and  $V_{init}$  that lie inside bounds on  $D_{NLG}$ ,  $D_{CG}$  and  $V_{loss}$  as shown.

with the light case,  $N_{CG}$  matches  $N_{OLG}$  very closely and is a good predictor of the loads at the main landing gears; see panels (a) and (b). For the heavy case the main lateral gear loads are more evenly distributed; see panels (c) and (d). Again, in all cases  $N_{CG}$  is a good predictor for the loads at the main landing gears. However, the loads at the NLG are vastly underestimated by  $N_{CG}$ . The main qualitative difference between the profile of  $N_{NLG}$  when compared with Figure 4.8 is that with increasing  $\delta_{fin}$  there is a peak value after which the load drops off; for the  $45^\circ$  turn this occurs at  $\delta_{fin} \approx 12^\circ$  and for the  $90^\circ$  turn at  $\delta_{fin} \approx 16^\circ$ , independently of the mass case. The data shows that the inadequacy of  $N_{CG}$  in predicting  $N_{NLG}$  is not limited to the extremes of the aircraft's operation.

## 4.6 Comparison of transient analysis and continuation analysis

We now discuss the relation between the results generated from two different types of computation: the transient analysis as presented in this chapter and the continuation analysis, as presented in Chapters 2 and 3. In the transient analysis trajectories are computed from an initial condition with the aircraft travelling in a straight line at fixed velocity, the steering angle is ramped up to a desired value, and the resulting trajectory studied. We focused on the data recorded in the transient period during which the aircraft is converging to a turning circle solution. A condition on the lateral velocity was used to determine whether the resulting trajectories converged to a stable turning solution or if there is a loss of lateral stability. In the continuation analysis we computed the turning circle solutions directly; the solutions were tracked under variation of parameters and their stability monitored; changes in stability occur at bifurcations. We aim to assess whether the stability boundaries as represented by curves of Hopf bifurcations in the continuation analysis are suitable for the identification of safe operating regions for the aircraft when performing a turn as considered in this chapter.

Figure 4.12 is a reproduction of Figure 4.6; recall that the greyscale map and associated

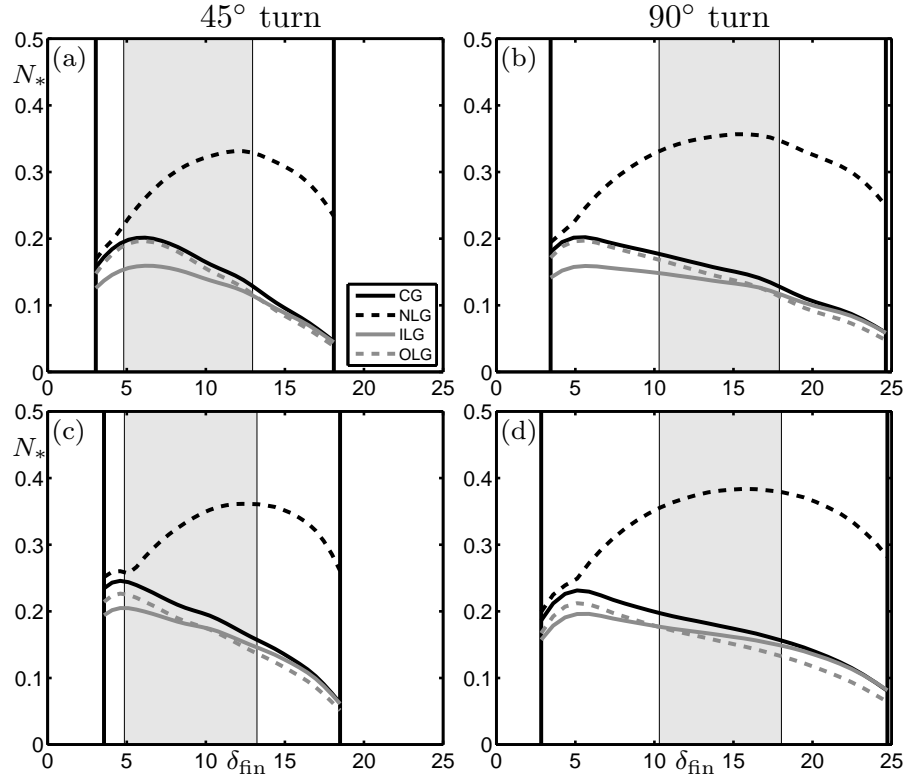


**Figure 4.11.** The lateral loads  $N_*$  (at CG, NLG, ILG and OLG) computed along the  $V_{\text{loss}}$  boundary curves parameterized in terms of  $\delta_{\text{fin}}$ . Panels (a) and (b) show data for the light aircraft case and panels (c) and (d) for the heavy aircraft case; turn degree is indicated at the top of the figure. In each panel the grey shaded region represents the values of  $\delta_{\text{fin}}$  corresponding to the appropriate operating region as shown in Figure 4.10; vertical black lines indicate the upper and lower extent of  $\delta_{\text{fin}}$  for the parameterized  $V_{\text{loss}}$  curve.

contours show the lateral load factor at CG for the trajectory represented by each  $(\delta_{\text{fin}}, V_{\text{init}})$ -pair. The solid black curve  $S$  represents the lateral stability boundary and points above the boundary are white. The curve of Hopf bifurcations  $H$  plotted in the  $(\delta, V_x)$ -projection is superimposed and corresponds approximately to  $N_{\text{CG}} = 0.23$ . For both the transient data and the continuation data, the steering angle  $\delta$  and the thrust  $T$  vary but all other model parameters are the same. The way in which  $\delta$  and  $T$  are varied is different in the two types of analysis. In the transient analysis the thrust is fixed at a value corresponding to the initial velocity  $V_{\text{init}}$  and the thrust varies in the range  $T \in (4.5\%, 6\%)$ . In the continuation analysis the curve  $H$  is computed directly under the variation of  $\delta$  and  $T$ ; the thrust varies in the range  $T \in (14\%, 17\%)$ . These thrust values correspond to straight-line velocities in excess of 25m/s; however, for  $\delta > 5^\circ$ , the corresponding velocity of the steady-state solutions is less than 25m/s. The trajectory for each  $(\delta_{\text{fin}}, V_{\text{init}})$ -pair effectively represents a traverse through the  $(\delta, V_x)$  parameter-state space. If the curve  $H$  is crossed, it is possible to exhibit the behaviour that exists at higher  $T$  values.

We now summarise the qualitative behaviour in terms of the curves  $H$  and  $S$ . For values of

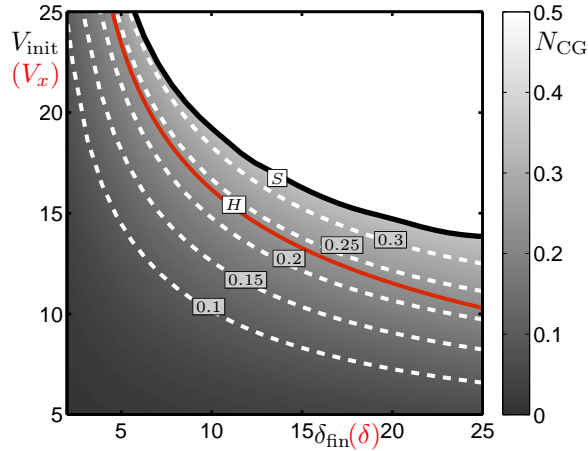


**Figure 4.12.** Reproduction of Figure 4.6 shows a greyscale map of the maximal lateral load factor  $N_{CG}$  for the output trajectory initialised from each  $(\delta_{f\text{ln}}, V_{\text{init}})$ -pair; the lateral stability boundary  $S$  is a thick black curve and dashed white curves are contours of  $N_{CG}$ . Overlaid is the curve of Hopf bifurcations  $H$  plotted in the  $(\delta, V_x)$ -projection. For both sets of data the mass case and CG position are the same; the curve  $H$  is computed under the variation of  $T$  and  $\delta$ .

$(\delta_{f\text{ln}}, V_{\text{init}})$  that lie below  $H$ , the aircraft converges to a stable turn and the forces generated by the main landing gear tyres do not saturate. For values of  $(\delta_{f\text{ln}}, V_{\text{init}})$  that lie in between  $H$  and  $S$ , the aircraft can exhibit the small-amplitude oscillatory behaviour close to the bifurcation  $H_2$  as described in Section 3.6. The associated trajectories converge to a stable turn, but the force generated by the outer main landing gear tyres can saturate and the tyres start to skid during the transient behaviour. For values of  $(\delta_{f\text{ln}}, V_{\text{init}})$  above  $S$ , the forces generated by the tyres at both main landing gears saturate, a skid starts and lateral stability is lost. Effectively, the lateral stability boundary in the transient analysis corresponds to the canard explosion as described in Section 3.6. From a practical point of view, the curve  $H$  provides a suitable limit that ensures the safe operation of the aircraft; specifically, it ensures that the forces generated at all the landing gears do not saturate so that the tyres do not skid.

## 4.7 Discussion

We presented a general approach to evaluate an aircraft's performance across an entire operating region for specific turning manoeuvres. A turn that represents pilot practice during taxiway manoeuvres was parameterized in terms of approach velocity and steering input. The output trajectories of the parameterized turn were then related directly to turning manoeuvres. Representative runway and taxiway geometries were chosen for two types of turning manoeuvre: a runway turn-off of  $45^\circ$  and a taxiway-to-taxiway transition of  $90^\circ$ . Operating regions were defined to represent a range of possible ways in which the different manoeuvres are performed where the limits of the regions represent the extremes of the aircraft's operation. Specifically, we considered the extremes of operation as given by the maximal lateral load factors (at the aircraft's CG position) reported in studies of in-service aircraft carried out by the FAA. Such

operating regions were defined for the two types of manoeuvre and for two mass cases. In this way we assessed the performance, in terms of the actual lateral loads experienced, of individual landing gear across the operating regions. In particular, we focused on the maximal lateral loads at the limits of the operating regions.

The results show that the lateral load factor at CG is a consistent predictor of the loads experienced at the main landing gears. We investigated asymmetric lateral loading between the main gears and found that whether greater loads occur at the inner or outer gear depends on the turn type and the aircraft mass. More significantly, the lateral loads at the nose landing gear cannot be predicted by the lateral load factor at CG; for the same lateral load at CG the load at the nose gear can vary by up to 100%. Another finding is that, for the same lateral load factor at CG, the actual lateral gear loads are largely unaffected by changes to the aircraft weight. We conclude that an investigation into lateral loading during taxiing operations should not be confined to studying the lateral load factor at CG. Furthermore, should future studies be carried out with instrumentation of the individual landing gears: it is of paramount importance that the nose gear be included. In conjunction with existing studies, our results suggest that, for the particular aircraft under consideration, the limit imposed in the FAR is too conservative for the main landing gears.

To illustrate the generality of the approach described above, it was adapted to study lateral gear loads in operating regions based on a criterion for the proportion of the aircraft's approach velocity that is conserved during a turn. The main observation is still that the lateral load factor at CG can predict the loads at the main gears, but not the loads at the nose gear. The robustness in the qualitative behaviour shows that the overall result is not limited to the extremes of the aircraft's operation. The criterion under consideration could easily be adapted to satisfy a specific safety margin for the landing gear loads with respect to regulation limits. Such a criterion could then be implemented through pilot practice or in an automatic control system. Our approach is suitable for the study of any reasonable criteria on the aircraft's operation; for example, speed limits depending on taxiway conditions, limiting vertical or lateral load on a specific gear, the maximal slip angles generated at the tyres, or a bound on the energy lost during manoeuvres. It can also be applied to study performance with respect to changes in design. A particular example would be to efficiently assess the performance of different landing gear configurations for heavy aircraft with more than two main gears.

In the final section of this chapter we discussed the relationship between the curve of Hopf bifurcations from the steady-state analysis and the lateral stability boundary found in the transient analysis. It was shown that the curve of Hopf bifurcations would be suitable for the definition of a safe operating region: operating below this curve would ensure that the forces on the tyres do not saturate and the tyres do not start to skid. Furthermore, we found that the lateral stability boundary in the transient analysis corresponds with the canard explosion discussed in Section 3.6. The region below the lateral stability boundary appears to be safe from the transient analysis alone. However, comparison with the steady-state analysis has shown that close to the lateral stability boundary the inner main landing gear tyres can saturate and start to skid. Overall, the curve of Hopf bifurcations provides an efficient way of predicting a region of safe operation for the aircraft.



# Chapter 5

## Conclusion and outlook

In this chapter we summarise the results presented in the thesis and discuss possible directions for future work.

### 5.1 Summary

The objective of this work was to use mathematical and computer modelling to study the dynamics of an aircraft moving on the ground. Through the application of advanced methods and the development of new techniques, we aimed to better understand the important factors that govern the dynamics. In particular, we aimed to develop an efficient method to identify safe operating conditions in order to inform operational practice and the design of automated control systems. Nonlinear effects are known to play a significant role in aircraft ground dynamics; therefore, it was essential that this be reflected in our modelling approach. The first part of our analysis was the identification and development of suitable models that incorporate an appropriate level of complexity and that include nonlinear effects where relevant. Numerical continuation and bifurcation analysis were identified as suitable tools for the study of such nonlinear systems: an approach that has not previously been applied to the study of aircraft ground dynamics. Overall the approach taken proved successful in gaining new insights into many aspects of aircraft ground operations.

In Chapter 2 we used an established, industry-tested model that, with minor modification, allowed us to perform a bifurcation analysis of turning circle solutions in terms of control parameters. The model was implemented in a multi-body systems package and includes nonlinear effects in the component models for the tyre forces, oleos and aerodynamics. The bifurcation analysis identified — in dependence on relevant control parameters — the boundaries between regions of safe operation, for which the aircraft follows a stable turning circle, and regions of unsafe operation, for which the aircraft exhibits a laterally unstable behaviour. For the specific configuration considered, the analysis provided a complete description of the possible dynamics and, more importantly, described the exact parameter regions that ensure safe operation. It was found that crossing a curve of Hopf bifurcations is associated with the transition to laterally unstable behaviour. Due to a robustness in the behaviour over ranges of parameters, we were able to provide a complete description of the aircraft's dynamics as represented by a single surface of solutions. Furthermore, we presented a comprehensive exposition of the qualitatively

different types of periodic motion in the unsafe region; a novel diagrammatic representation was used to describe the order in which the forces at each landing gear saturate during the loss of lateral stability.

In Chapter 3 we developed the full equations of motion for an aircraft turning on the ground. In conjunction with component models that describe the forces acting on the airframe, a fully mathematical description of the existing multibody model was given. The new mathematical model was fully validated against the existing model and shows a high level of agreement between the respective steady-state solutions and periodic motions describing laterally unstable behaviour. This computationally efficient mathematical model facilitated an extended bifurcation analysis over the relevant range of a total of four parameters describing the aircraft's control and operational configuration. Two-parameter bifurcation diagrams were represented as surfaces of solutions. Under the variation of additional parameters we were able to identify qualitative changes in such surfaces of solutions. In this way, we were able to present extensive parameter studies in a compact manner. A separate case study in terms of a tyre friction parameter revealed a direct analogy between reducing the friction and increasing the engine thrust. The improved versatility of the mathematical model facilitated a detailed analysis of the transition from stable turning to laterally unstable behaviour associated with a curve of Hopf bifurcations. The system was shown to have a separation of time-scales and, by freezing the dynamics of the system's slow variable, we were able to provide strong numerical evidence that the loss of lateral stability is mathematically a canard explosion.

In Chapter 4 the aim was to assess the suitability of the regulation imposed by the FAA with regards to lateral loading during taxiing. We compared our simulation data with statistical studies of the usage of in-service aircraft carried out by the FAA. In these studies, only the lateral loads experienced at the aircraft's CG position were reported; we aimed to determine whether this information is sufficient to predict the loads at individual gears. Since the maximal lateral loads occur in the transient period, during which the aircraft is converging to a stable turning circle, it was necessary to use an approach that takes into account this transient dynamics. We developed a parametrised turn defined by the velocity approaching the turn and the steering input. We defined operating regions in terms of these parameters representing a range of possible ways in which manoeuvres can be performed. The definition took into account the taxiway geometry and the limits of operation specified by the maximal lateral loads reported the FAA studies. For two different turn geometries and two different mass cases we found the maximal lateral loads experienced by individual landing gears at the limits of the aircraft's operation. We found that the loads at the aircraft's CG position could not accurately predict the loads at individual landing gears. Furthermore, we found this result to be robust with respect to the mass case and the criteria used to define the operational region. Finally, we discussed the relationship between the transient analysis and the continuation analysis; in particular, we established that the curve of Hopf bifurcations is a suitable limit of safe operation.

## 5.2 Future work

The primary goal for commercial aircraft taxiing between terminal and runway is to do so quickly and safely. Minor pre-take-off and post-landing incidents that occur quite frequently during taxiing are typically attributed to pilot error or adverse weather conditions. Such incidents may lead to extensive delays and high maintenance costs. In order to address these

concerns the ultimate goal is the design of adaptive control systems that can perform manoeuvres efficiently and safely whilst taking into account operating conditions.

We found that the dynamical behaviour described by the models presented is organised by an intricate solution structure. The bifurcation results describe regions of safe operation for the aircraft in terms of several relevant parameters. An understanding of how the regions of safe operation change with respect to operational parameters can inform the design of controllers that adapt to, for example, the aircraft loading and taxiway conditions. The identification of system states or measurable outputs that, if monitored, can predict if the aircraft is in danger of losing lateral stability requires further investigation. Control systems that monitor such states could be designed to take evasive action to ensure the safe operation of the aircraft. Following the design of an automated control system, its effectiveness can in turn be evaluated with bifurcation analysis.

The equations of motion described in the mathematical model provide a concrete example of a system with physical relevance that exhibits a separation of time scales and canard-type periodic orbits. The next step in the analysis would be to identify the dependence of the system's time-scale ratio on physical parameters. This information is of practical significance because it can be used to predict how soon after passing a Hopf bifurcation a canard explosion, which results in a loss of lateral stability, will be encountered. The development of a further-reduced set of governing equations that capture all the important dynamical behaviour would facilitate further progress in this area. Furthermore, it might allow for an analytical approach. Preliminary work has shown that equations describing only the planar motion, in two translational DOF and one rotational DOF, can still capture all of the qualitative dynamics. Another extension of the bifurcation analysis would be to investigate the possible existence of homoclinic connections and chaotic dynamics that are known to exist near a Bogdanov-Takens bifurcations [29].

To investigate the lateral loads experienced during turning we carried out an analysis taking into account transient effects. This was done because, over certain parameter ranges, steady-state behaviour of the system alone does not provide sufficient information to study specific turning manoeuvres with respect to taxiway geometry. Further work is required in order to understand better the relation between the steady-state analysis and the transient analysis. We propose that it would be possible to compute trajectory segments that include transient behaviour under the variation of parameters. With the definition of suitable boundary value conditions on the initial point of the trajectory and a second point after convergence to a steady-state, it would be possible to use continuation to compute and then follow an entire aircraft trajectory. This sort of computation would provide complete trajectory information that could be related directly to taxiway geometries; furthermore, this approach might permit studies of how different parameters, such as the steering rate and braking input, affect the transient dynamics.



## References

- [1] E. L. Allgower and K. Georg, *Introduction to numerical continuation methods*, Society for Industrial Mathematics, December 2003.
- [2] P. Basu-Mandal, A. Chatterjee, and J. M. Papadopoulos, *Hands-free circular motions of a benchmark bicycle*, Proceedings of the Royal Society A: Mathematical, Physical and Engineering Science **463** (2007), no. 2084, 1983–2003.
- [3] R. G. Bedford and M. H. Lowenberg, *Bifurcation analysis of rotorcraft dynamics with an underslung load*, AIAA Atmospheric Flight Mechanics Conference (2004), no. AIAA-2004-4947.
- [4] E. Benoît, J.-L. Callot, F. Diener, and M. Diener, *Chasse au canard*, Collect. Math. **32** (1981), 37–119.
- [5] J. M. Biannic, A. Marcos, M. Jeanneau, and C. Roos, *Nonlinear simplified LFT modelling of an aircraft on ground*, Proceedings of the IEEE Computer Aided Control Applications Conference **1** (2006).
- [6] M. Blundell and D. Harty, *The multibody systems approach to vehicle dynamics*, SAE International, September 2004.
- [7] M. Brøns, *Bifurcations and instabilities in the Greitzer model for compressor system surge*, Engineering in Industry **2** (1988), no. 1, 51–63.
- [8] E. F. Bruhn, *Analysis and design of flight vehicle structures*, Jacobs Publishing Inc., June 1973.
- [9] G. A. Charles, M. H. Lowenberg, D. P. Stoten, X. Wang, and M. di Bernardo, *Aircraft flight dynamics analysis and controller design using bifurcation tailoring*, AIAA Guidance Navigation and Control Conference (2002), no. AIAA-2002-4751.
- [10] E. B. Coetzee, *Nonlinear aircraft ground dynamics*, Master’s thesis, University of Bristol, 2006.
- [11] N. S. Currey, *Aircraft landing gear design: Principles and practices*, American Institute of Aeronautics and Astronautics, 1988.
- [12] E. J. Doedel, A. R. Champneys, T. F. Fairgrieve, Y. A. Kuznetsov, B. Sandstede, and X. Wang, *Auto 97 : Continuation and bifurcation software for ordinary differential equations*, <http://indy.cs.concordia.ca/auto/>, May 2001.

- [13] W. Eckhaus, *Relaxation oscillations including a standard chase on French ducks*, Asymptotic Analysis II (F. Verhulst, ed.), Lecture Notes in Math., vol. **985**, Springer-Verlag, New York, 1983, pp. 449–494.
- [14] B. Etkin, *Dynamics of atmospheric flight*, Wiley, 1972.
- [15] FAA, *Airport design*, Advisory Circular **150** (1989), 33–40.
- [16] E. Finn, R. Gleich, K. Green, R. Saccarelli, and M. Szot, *Investigation of limit design lateral ground maneuver load conditions*, Tech. Report DOT/FAA/AR-07/38, Federal Aviation Administration, June 2007.
- [17] G. Franke, W. Suhr, and F. Riess, *An advanced model of bicycle dynamics*, European Journal of Physics **11** (1990), no. 2, 116.
- [18] T. D. Gillespie, *Fundamentals of vehicle dynamics (r114)*, SAE International, March 1992.
- [19] J. Guckenheimer and P. Holmes, *Nonlinear oscillations, dynamical systems and bifurcations of vector fields, applied mathematical sciences vol. 42*, Springer, 1983.
- [20] M. Jeanneau, *Description of aircraft ground dynamics*, Garteur FM AG17 RP0412731, GARTEUR, 2004.
- [21] \_\_\_\_\_, *Nonlinear analysis and synthesis techniques for aircraft control*, ch. 1. The Airbus on-ground transport aircraft benchmark, pp. 3–24, Springer, 2007.
- [22] T. Jones, J.W. Rustenburg, D.A. Skinn, and D.O. Tipps, *Study of side load factor during aircraft ground operations*, Tech. Report DOT/FAA/AR-05/7, Federal Aviation Administration, March 2005.
- [23] P. D. Khapane, *Simulation of asymmetric landing and typical ground maneuvers for large transport aircraft*, Aerospace Science and Technology **7** (2003), no. 8, 611–619.
- [24] D. H. Klyde, R. E. Magdaleno, and J. G. Reinsberg, *The effect of tire pressure on aircraft ground handling*, Journal of Guidance, Control, and Dynamics **26** (2003), no. 4, 558–564.
- [25] D. H. Klyde, T. T. Myers, R. E. Magdaleno, and J. G. Reinsberg, *Development and evaluation of aircraft ground handling maneuvers and metrics*, AIAA Atmospheric Flight Mechanics Conference Proceedings (2001), no. AIAA-2001-4011.
- [26] D.H. Klyde, T.T. Myers, R.E. Magdaleno, and J.G. Reinsberg, *Identification of the dominant ground handling characteristics of a navy jet trainer*, Journal of Guidance, Control, and Dynamics **25** (2002), no. 3, 546–552.
- [27] D.H. Klyde, E. Sanders, J.G. Reinsberg, and A. Kokolios, *Flight test evaluation of a stability augmentation steering system for aircraft ground handling*, Journal of Guidance, Control, and Dynamics **27** (2004), no. 1, 41–51.
- [28] B. Krauskopf, H. M. Osinga, and J. Galán-Vioque, *Numerical continuation methods for dynamical systems*, Springer, 2007.

- [29] Y. A. Kuznetsov, *Elements of applied bifurcation theory*, Springer-Verlag, September 1998.
- [30] Z. Liu and G. Payre, *Global bifurcation analysis of a nonlinear road vehicle system*, *Journal of Computational and Nonlinear Dynamics* **2** (2007), no. 4, 308–315.
- [31] Z. Liu, G. Payre, and P. Bourassa, *Nonlinear oscillations and chaotic motions in a road vehicle system with driver steering control*, *Nonlinear Dynamics* **9** (1996), no. 3, 281–304.
- [32] M. Lowenberg, D. Rezgui, and P. Bunniss, *Experimental evaluation of numerical continuation and bifurcation methods applied to autogyro rotor blade aeromechanical stability*, *Proceedings of ASME IDETC 2009* (2009), no. DETC2009-87634.
- [33] M. H. Lowenberg, *Bifurcation analysis of multiple-attractor flight dynamics*, *Philosophical Transactions: Mathematical, Physical and Engineering Sciences* **356** (1998), no. 1745, 2297–2319.
- [34] Mathworks, *Model and simulate mechanical systems with SimMechanics*, <http://www.mathworks.com/products/simmechanics/>, 2004.
- [35] J. P. Meijaard, J. M. Papadopoulos, A. Ruina, and A. L. Schwab, *Linearized dynamics equations for the balance and steer of a bicycle: a benchmark and review*, *Proceedings of the Royal Society A: Mathematical, Physical and Engineering Science* **463** (2007), no. 2084, 1955–1982.
- [36] J. P. Meijaard and A. A. Popov, *Numerical continuation of solutions and bifurcation analysis in multibody systems applied to motorcycle dynamics*, *Nonlinear Dynamics* **43** (2006), no. 1, 97–116.
- [37] D. J. Mitchell, *Calculation of ground performance in take-off and landing*, Data Sheet 85029, ESDU, 1985.
- [38] V. Nguyen, G. Schultz, and B. Balachandran, *Lateral load transfer effects on bifurcation behavior of four-wheel vehicle system*, *ASME Journal of Computational and Nonlinear Dynamics* **4** (2009), no. 4, 041007.
- [39] V. Nguyen and G. A. Schultz, *Vehicle handling, stability, and bifurcation analysis for nonlinear vehicle models*, Master's thesis, Department of Mechanical Engineering, University of Maryland, 2005.
- [40] H. B. Pacejka, *Tyre and vehicle dynamics*, Elsevier, 2006.
- [41] W. F. Phillips, *Mechanics of flight*, Wiley, January 2004.
- [42] J. Rankin, E. Coetsee, B. Krauskopf, and M. Lowenberg, *Bifurcation and stability analysis of aircraft turning on the ground*, *AIAA Journal of Guidance, Control, and Dynamics* **32** (2009), no. 2, 499–510.
- [43] \_\_\_\_\_, *Nonlinear modeling and analysis of aircraft ground dynamics*, MATHMOD 2009 - 6th Vienna International Conference on Mathematical Modelling **261** (2009), 2600–2603.

- [44] J. Rankin, B. Krauskopf, M. Lowenberg, and E. Coetzee, *Operational parameter study of aircraft dynamics on the ground*, ASME Journal of Computational and Nonlinear Dynamics **5** (2010), no. 021007.
- [45] J. W. Rustenburg, D. A. Skinn, and D. O. Tipps, *Statistical loads data for a Boeing 737-400 aircraft in commercial operations*, Tech. Report DOT/FAA/AR-98/28, Federal Aviation Administration, August 1998.
- [46] ———, *Statistical loads data for Boeing 767-200ER aircraft in commercial operations*, Tech. Report DOT/FAA/AR-00/10, Federal Aviation Administration, March 2000.
- [47] ———, *Statistical loads data for the Airbus A320 aircraft in commercial operations*, Tech. Report DOT/FAA/AR-02/35, Federal Aviation Administration, April 2002.
- [48] A. Shabana, *Dynamics of multibody systems*, 2nd ed., Cambridge University Press, October 2003.
- [49] G. Stépán, *Delay, oscillations and shimmying wheels*, Proceedings of Symposium CHAOS97, Kluwer Ac. Publ., Dordrecht **1** (1998), 373–386.
- [50] S. H. Strogatz, *Nonlinear dynamics and chaos*, Springer, 2000.
- [51] D. Takács and G. Stépán, *Experiments on quasiperiodic wheel shimmy*, ASME Journal of Computational and Nonlinear Dynamics **4** (2009), no. 3, 031007.1–031007.7.
- [52] J. M. T. Thompson and F. B. J. Macmillen (Eds.), *Nonlinear flight dynamics of high-performance aircraft*, Philosophical Transactions of the Royal Society A **356** (1998), no. 1745, 2165–2333.
- [53] P. Thota, B. Krauskopf, and M. Lowenberg, *Interaction of torsion and lateral bending in aircraft nose landing gear shimmy*, Nonlinear Dynamics **57** (2009), no. 3, 455–467.
- [54] ———, *Bifurcation analysis of nose-landing-gear shimmy with lateral and longitudinal bending*, Journal of Aircraft **47** (2010), no. 1, 87–95.
- [55] D. O. Tipps, J. Rustenburg, D. Skinn, and T. DeFiore, *Side load factor statistics from commercial aircraft ground operations*, Tech. Report UDR-TR 2002-00119, Federal Aviation Administration, January 2003.
- [56] D. A. Venn, *The application of bifurcation analysis to road vehicle dynamics*, Ph.D. thesis, Department of Aerospace Engineering, University of Bristol, 2006.
- [57] J.Y. Wong, *Theory of ground vehicles*, 3rd ed., Wiley-Interscience, March 2001.
- [58] Q. Zhu and M. Ishitobi, *Chaos and bifurcations in a nonlinear vehicle model*, Journal of Sound and Vibration **275** (2004), no. 3-5, 1136–1146.